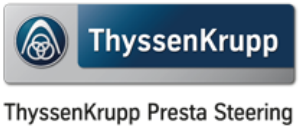

ThyssenKrupp Presta Steering

Graz University of Technology

Master Thesis

Model-based Controller Concepts for Steering by Torque Vectoring

conducted at the
Institute of Automotive Engineering
Graz University of Technology

in corporation with
ThyssenKrupp Presta AG
Eschen, Liechtenstein

by
Mathias Vierhauser

Supervisors, TU Graz:
Dipl.-Ing. Dr.techn. Cornelia Lex
Dipl.-Ing. Andreas Hackl BSc

Supervisors, ThyssenKrupp Presta AG:
Dr.-Ing. Carlo Miano
Dipl.-Ing. Leonard Lapis

Assessors/Examiners:
Dipl.-Ing. Dr.techn. Jürgen Fabian

Graz, September 2017
Restricted access until October 16, 2019

Statutory Declaration

I declare that I have authored this thesis independently, that I have not used other than the declared sources/resources, and that I have explicitly marked all material which has been quoted either literally or by content from the used sources.

date (signature)

Eidesstattliche Erklärung

Ich erkläre an Eides statt, dass ich die vorliegende Arbeit selbstständig verfasst, andere als die angegebenen Quellen/Hilfsmittel nicht benutzt, und die den benutzten Quellen wörtlich und inhaltlich entnommene Stellen als solche kenntlich gemacht habe.

Graz, am (Unterschrift)

Abstract

This thesis deals with the control of *Steering by Torque Vectoring*, a redundant steering concept for a *Steer by Wire* vehicle. Different driving torques on the front wheels are used to generate desired steering angles in order to steer the vehicle. Along with a 27 degree of freedom simulation model, different controller concepts are developed and tested on a real car. The prototype vehicle is represented by a BMW X5, which was refitted into an electrical powered car with a Steer by Wire system and individually propelled front wheels.

In the first part of this thesis, a linear representation of the system is derived and validated with the simulation model and measurement data. With this representation, two different model-based controller concepts are developed and implemented on the hardware of the prototype vehicle. On special test tracks, these controller concepts are tested, occurring problems are identified and investigated. Finally, the breakdown of the steer by wire system is investigated by disabling the steering actuator and switching to the Torque Vectoring redundancy.

Kurzfassung

Die vorliegende Masterarbeit befasst sich mit der Regelung von *Steering by Torque Vectoring*, ein redundantes Lenkungskonzept für ein Steer by Wire Fahrzeug. Durch verschiedene Antriebsmomente an den Vorderrädern können gewünschte Lenkwinkel eingestellt werden. Dieser Effekt kann zum Lenken des Fahrzeugs genutzt werden. Zusammen mit einem 27 Freiheitsgrade umfassenden Simulationsmodelles werden verschiedene Regelkonzepte entworfen und am echten Fahrzeug getestet. Der verwendete Prototyp ist ein umgebauter BMW X5, dessen Vorderräder individuell elektrisch angetrieben werden können. Das bestehende Lenksystem wurde durch ein Steer by Wire System ersetzt.

Im ersten Teil der Masterarbeit wird ein lineares Modell des Systems abgeleitet, welches anhand des Simulationsmodelles und Messdaten validiert wird. Anhand dieser linearen Abbildung werden zwei modellbasierte Regelungskonzepte entworfen und auf der Hardware des Protoyps implementiert. Auf speziellen Teststrecken werden diese Regelungskonzepte getestet, auftretende Probleme erkannt und untersucht. Zum Schluss wird der Ausfall des Steer by Wire Systems durch Abschalten des Lenkaktuators simuliert und dabei der Übergang auf Steering by Torque Vectoring untersucht.

Contents

1 Introduction

1.1 ThyssenKrupp Presta AG

ThyssenKrupp Presta AG (TKP) is one of the market-leading manufacturer for steering systems. With about 7000 employees in 16 countries, TKP is part of the ThyssenKrupp group. By having a wide product range from simple cold forging parts to steering columns, complete steering systems and just recently also electric drives, TKP supplies nearly all global automotive manufacturers. The main research and development department is located in Eschen, Liechtenstein, which is also the head quarter of the company. However, the expenditures for R&D activities accounts a high rate of the company's total spending, which stands for a high level of diversification and innovation. One of the latest topic of research is the so called *Steer by Wire* (SbW) System [1].

1.2 Steer by Wire

For a long time, steering systems in automotive vehicles were just mechanical connections between the steering wheel and the driven wheels. Over the years, comfort and safety got more important and the automotive industry has been making continuous effort in developing more advanced steering systems. So called power assisted steering systems (PAS) had been introduced and are available in many different forms and implementations. With these systems, the driver is supported in the steering motion, but as there is still a mechanical connection, the fixed steering ratio limits their possibilities [2]. The next major development was active front power assisted steering (AFS), where the steering axle is decoupled from the steering wheel (e.g. with a planetary gear and a electric motor), but still has a mechanical connection. This gives the possibility of a variable steering ratio. AFS offers complete freedom on the response side, but the feedback tuning possibilities are still limited. To get rid of all limitations, the solution is a full Steer by Wire system (SbW) [3].

In a SbW system, both the road wheels and the steering wheel torque are controlled by their own actuator. Both the response of the car and the feedback to the driver are controlled by software and are completely independent of each other. This offers maximum functional freedom in both response and feedback, which is only limited by the actuator performance and dynamics. The main issue with SbW systems is safety, as no mechanical link is available between the road wheels and the steering wheel [3]. Figure 1.1 illustrates the main difference between a conventional PAS and a SbW system. Because of the high safety requirements, two concepts are distinguished:

- *Fail-safe system with mechanical back-up:* If an error is detected, a clutch can be closed and a mechanical linkage is established (implemented in the Nissan Infinity Q50, which is the first SbW production vehicle).
- *Fail tolerant system with self controlled redundancies:* This layout requires double actuators, double electrical circuit, double sensors, etc.

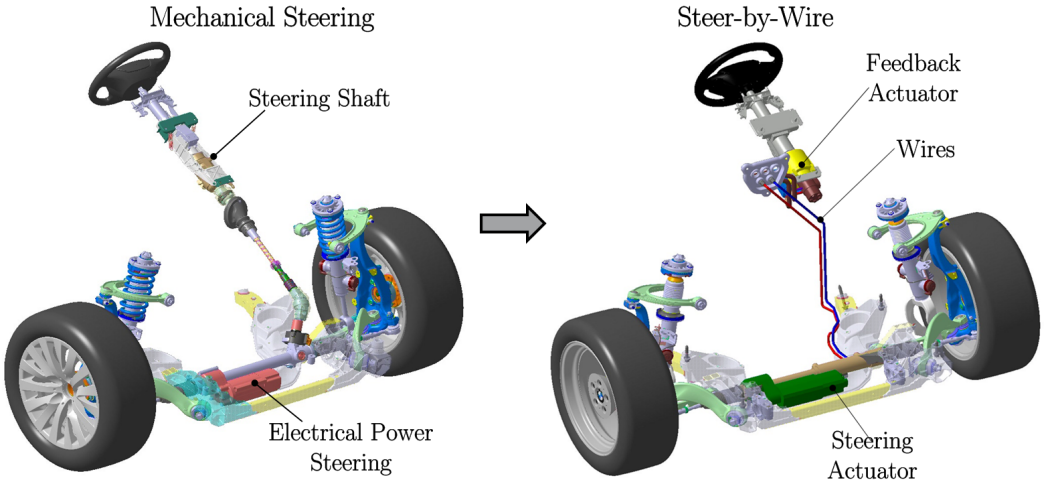

Figure 1.1: Comparison of a conventional PAS to a SbW system [4]. In SbW, the steering column and shaft is replaced by a fully electrical connection with actuators on both sides. The steering actuator controls the driven wheels to the desired steering angle, whereas the feedback actuator delivers a haptic response of the driving state to the driver [2].

The fail-safe system is less expensive and less complicated, but also has the disadvantage that a steering column is still necessary. This implicates that this solution does not have the extra flexibility and modularity of a fail tolerant system without a steering column. Also crash performance is a big advantage in a system without a steering column [3]. For fail tolerant systems there are many different approaches. Besides the full redundancy of the actuator, there is also the possibility to use single wheel steering (as shown in [5]), or, if the wheels can be propelled independently, the use of the so called *torque steering effect* [6].

1.3 Steering by Torque Vectoring

In general, torque vectoring (TV) means individual torque distribution on at least one pair of wheels. In today's cars, TV is mostly used to stabilize and improve the lateral dynamics, which means that it can be seen as an extension to the regular steering system. Since cars with combustion engines require special torque vectoring differentials, which are very complex and expensive, this feature is reserved for luxury and sports cars. For vehicles with independent electric drives, TV becomes much more applicable. Especially in combination with a SbW system, TV on the front axle allows to steer the vehicle with a non working or even without any steering actuator. This effect is called *Steering by Torque Vectoring* (SbTV) and is explained in Figure 1.2.

The success of SbTV is mostly determined by the suspension design. As mentioned in Figure 1.2, lateral forces and self aligning torques of the tires act against the longitudinal forces. If this influence is significant, the electric drives have to generate high drive torques to compensate this effect, which leads to the main limitations of SbTV. On the one hand, high drive torques require powerful motors, which would increase the costs of the system tremendously. On the other hand, high torques require enough traction on the wheels to build up the necessary longitudinal forces. Especially at bad road conditions (e.g. snow, ice, or gravel), this demand often cannot be fulfilled. To achieve a good performance, this effect has to be minimized. Figure 1.3 describes some important characteristic steering kinematic values and their influence on this problem. According to [6], a high *normal*

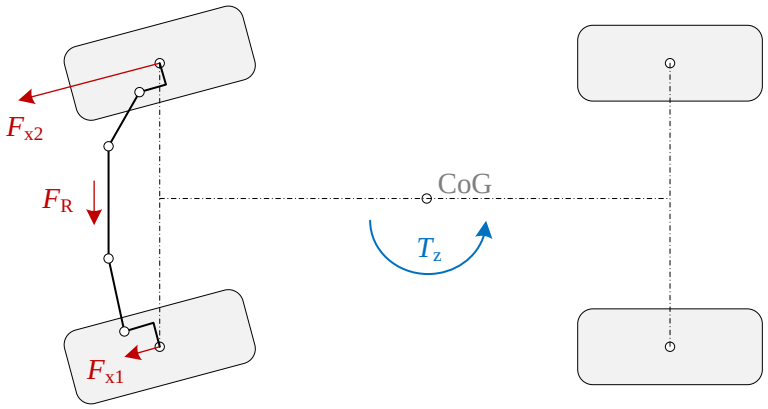

Figure 1.2: Principle of Steering by Torque Vectoring. By applying different driving torques on the front wheels, two major effects take place. First, the difference of the resulting longitudinal forces F_{x1} and F_{x2} causes a yaw-torque T_z around the z-axis. Second, under a suspension dependent transmission, a longitudinal force generates a torque around the steering axis that forces the tire to steer. With the steering, the tire builds up lateral force and self alignment torque that act against the steering movement. At a certain steering angle, the forces and torques of the tire are at an equilibrium and the steering movement stops. If the front wheels are connected with a steering rack, also the other tire influences this behavior. Then, this equilibrium can be described with the force on the steering rack F_R.

steering axis offset at wheel center and a small *castor offset at ground* is desirable. At present suspensions, these values are designed to provide the driver a desired feedback, but since SbW has complete freedom on the response side, these characteristics can be chosen more widely.

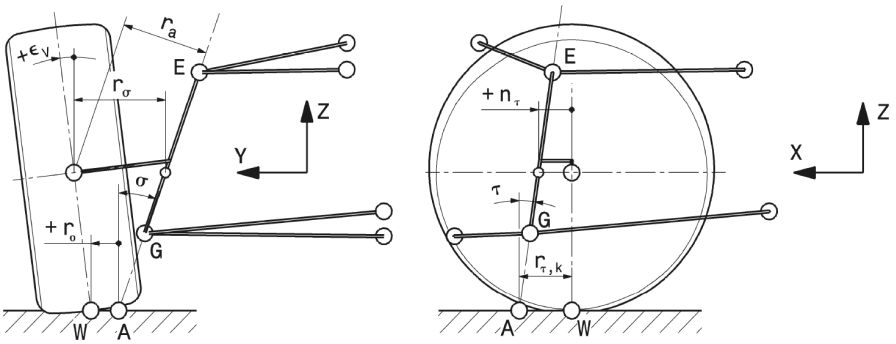

Figure 1.3: Characteristic steering kinematic values according to Matschinsky [2]. For SbTV, two values are essential. The *normal steering axis offset at wheel center* r_a as the lever arm for the longitudinal forces and the *castor offset at ground* $r_{\tau,k}$ as the lever arm for the lateral forces. Investigations showed that a low ratio of $r_{\tau,k}/r_a$ is representative for a good performance of SbTV [6].

Besides the possibility of providing redundancy for a fail tolerant SbW system, SbTV brings additional advantages. In a supportive role, TV can reduce the demands on the steering actuator, which could reduce the costs of the SbW hardware. Furthermore, TV still can be used for stabilization of the lateral dynamics. One can see that there is a high potential to justify the added complexity in the propulsion system. TKP conducted several research projects in the past and also this thesis deals with the topic of SbTV.

1.4 Motivation

The history of SbTV at TKP started with the master thesis of Marc Zurbuchen [7] in 2013. He derived a suitable vehicle model based on a Formula Student car and did first theoretical investigations with different controller concepts. Sebastian Stracke continued these concepts in his thesis [6] in 2014, improved the simulation model by a more advanced tire and steering rack model and developed a LQR controller strategy with gain scheduling for controlling the position of the steering rack. Due to technical problems at the test vehicle, also this investigations remained theoretically. In the meantime, TKP and Suncar from ETH Zürich refitted a BMW X5 into a fully electrical powered vehicle to provide a proper research prototype for SbTV [8]. In 2016, Cornel Pfister and Jan Reis [9] developed and validated a complex SIMPAC simulation model based on the BMW X5. They tried different controller designs based on the LQR concepts from Stracke, but didn't get satisfying results on the real car. In the beginning of 2017, intern engineers at TKP designed a PID controller with a vehicle speed dependent gain scheduling. They achieved a good performance in controlling the position of the steering rack. Nevertheless, also with this solution, the potential of the system is not fully used. Therefore, further research was commissioned.

Based on a vehicle model from Georg Rill [10], Klaus Esser [11] and Gerald Reiter [12] validated an advanced simulation model for the BMW X5. With this model as a foundation for realistic simulations, the performance of SbTV should reach a new level of performance.

1.5 Goal of the Thesis

The goal of this thesis is to develop a strategy to control the position of the steering rack of the prototype vehicle BMW X5 under the principle of SbTV. With help of the simulation model [12], the performance of the resulting system should exceed previous solutions clearly. The new concepts should identify the limits of SbTV and find possible improvements to exceed these limits. Furthermore, the error handling of the SbW system has to be investigated. In the case of a breakdown of the steering actuator, SbTV as the redundant system has to provide a safe and stable transition from the error case to a normal operating mode of the redundancy.

2 System Overview

In this chapter, the basis for this thesis is presented. Starting with an overview of the test vehicle and the used hardware, also the development tools and software are introduced. Subsequently, the simulation model will be explained in more detail following by the existing controller concepts for SbTV, which determine the benchmark for this thesis.

2.1 Test Vehicle "BMW X5 iSUV"

To provide a proper research platform, TKP and Suncar from ETH Zürich developed a prototype vehicle based on a BMW X5 e70 from 2007 [8]. The car was refitted to an electrical powered vehicle featuring two independent drives on the front wheels to allow SbTV. Figure 2.1 shows the car from outside and Figure 2.2 gives some insights to the reconstruction of the car. Furthermore, the steering system of the car has been replaced by a fail safe SbW system with a mechanical clutch. In case of an error, this clutch can be closed.

Figure 2.1: Test Vehicle BMW X5 iSUV [4].

The electrical drives are synchronous motors of type HSM1-10.18.13 from the manufacturer *Brusa*. With a supply voltage of 400 VDC, they can deliver a constant torque of 305 Nm up to a constant power of 93 kW each. To allow higher torques on the wheel side, every motor has a gearbox with a ratio of 1:5.5 installed. The battery has a nominal capacity of 85 kWh and comes from a decommissioned Tesla vehicle. The weight of the battery pack is very high, which raises the overall weight of the car from 2185 kg of the original X5 to 2659 kg.

Since the car is designed to be a research vehicle, several additional sensors to the stock version are installed. The essential ones for SbTV are described in Table 2.1.

(a) Engine compartment of the refitted BMW with all the power electronic devices.

(b) Interior of the car with one of the installed battery packs.

Figure 2.2: The combustion engine with all associated parts had been removed and replaced by two independent synchronous motors, gearboxes and appropriate inverters. Instead of the back seats, one part of the battery is installed. The second part of the battery is mounted at the underbody.

Table 2.1: Essential Sensors for SbTV on the BMW X5.

Physical value	Comment
rack position u_r	The sensor is placed at the input shaft of the steering rack and has a very high precision. The signal can be seen as virtually noiseless.
rack velocity $\dot{u}_\mathrm{r}$	This value is measured with an internal motor sensor of the SbW power pack The signal can also be used for SbTV, when the steering actuator is switched off.
steering wheel angle δ_w	To generate a reference, the position of the steering wheel needs to be known and is measured in the feedback actuator of the SbW system.
yaw rate $\dot{\psi}$	This signal comes from a *Racelogic VBOX IMU04* sensor.
wheel speeds ω_3 and ω_4	With an average of the rear wheel speeds, the velocity of the car can be estimated.

Autobox - ControlDesk

The main processing unit is a Autobox from dSpace, which is a rugged embedded system, specially designed for prototype vehicles [13]. It consists of a robust casing with a real-time processor and different I/O cards. Supplied by a separate battery, also the safety functions, like the mechanical clutch of the SbW system is controlled by this processor. ControlDesk, which is the software of Autobox, is the interface between hardware and software, providing a powerful experimental tool for the entire development process of automotive electronic control devices. As it is directly compatible with Matlab/Simulink, this system fulfills all requirements for a promising development environment.

2.2 Simulation model (VTC model)

Usually, making tests on the real prototype car is associated with high costs, as one has to rent a special test track, organize a transport for the vehicle and in some cases, also professional test drivers are needed. With realistic simulation models, one can benefit a lot in terms of costs and development time for new systems. Therefore, TKP arranged a cooperation with the Graz University of Technology to derive and validate a proper simulation model for the BMW X5.

The regarding model (VTC model) is based on a multi-body approach from Georg Rill [10] and was extended and validated by two students. Klaus Esser on the one hand did the validation of the tire model [11] and Gerald Reiter on the other hand extended the model with special suspension- and steering rack models [12]. Also the validation of the remaining parts were done by Gerald Reiter. The model was realized in MATLAB R2013b without any requirement on special toolboxes. Figure 2.3 gives an overview of the structure.

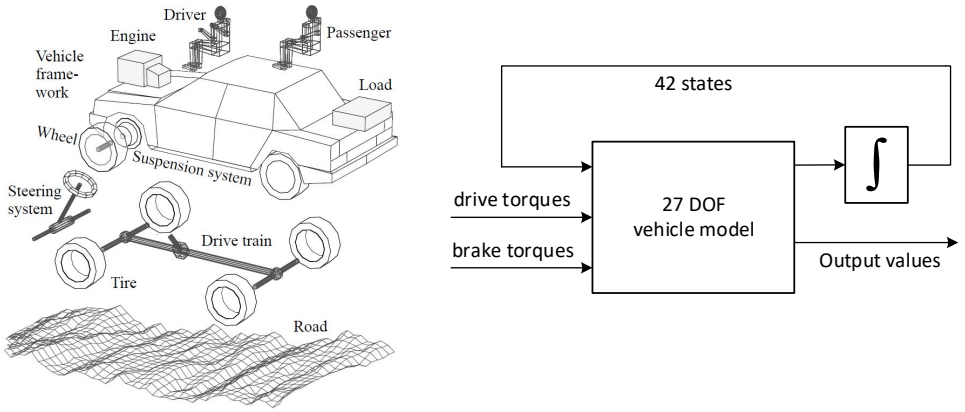

(a) A general multi-body structure for a vehicle simulation model by Georg Rill [10].

(b) Input-Output scheme for the VTC model. The system consists of more states than DOF due to several 2nd order differential equations.

Figure 2.3: A quick overview of the simulation model for the BMW X5. The whole system is separated in several single bodies (tires, suspension, chassis, ...) which are modeled separately. For a connection between the single bodies, the principle of *Jourdain* and *D'Alembert* is applied. The result is a model with 27 degrees of freedom (DoF), which are described in Table 2.2 in more detail. Drive- and brake torques on all wheels are the input quantities of the model.

Table 2.2: The DoF's of the model in more detail. Because of the high complexity, this model is just capable of off-line simulations.

Degrees of freedom (DoF)	
3	position of the vehicle (longitudinal, lateral, vertical)
3	orientation of the chassis (roll, pitch, yaw)
4	rotation angles of the wheels
4	suspension deflections
3×4	tire states for the TMeasy tire model [10]
1	steering rack position

2.3 Existing controller concept

In February 2017, internal engineers from TKP tuned a PID-controller for the control of the rack position u_r. Dependent on the vehicle speed, the car changes it's behavior clearly, which means that the controller had to be tuned for several velocities. To avoid discontinuities in the switching process, gain scheduling of the parameters with lookup-tables was realized. Figure 2.4 shows the structure of the implemented controller and Figure 2.5 shows the speed dependent parameters of the heuristically tuned controller.

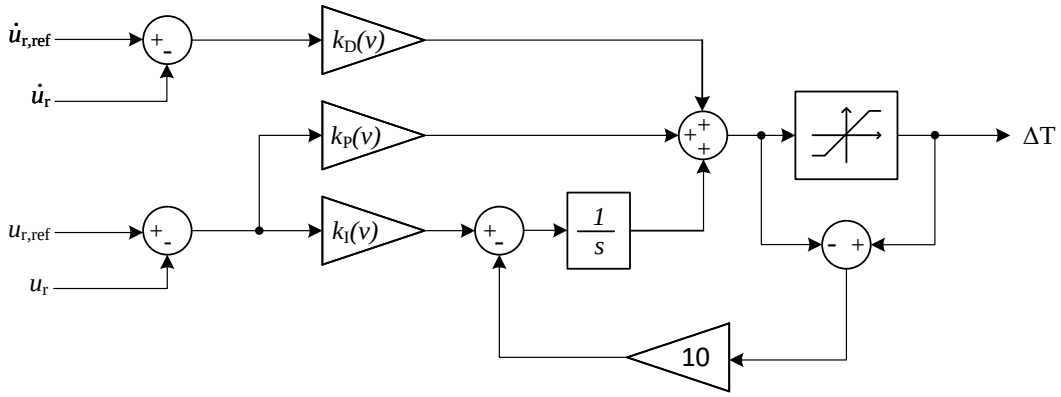

Figure 2.4: Structure of existing PID-controller [4]. Since the rack velocity $\dot{u}_\mathrm{r}$ can be measured, there is no need for additional dynamics in the derivative part. Hence the controller has 4 input parameters. The only dynamics comes from the integral part. The feedback of the saturated control signal to the integrator works as a anti-windup principle.

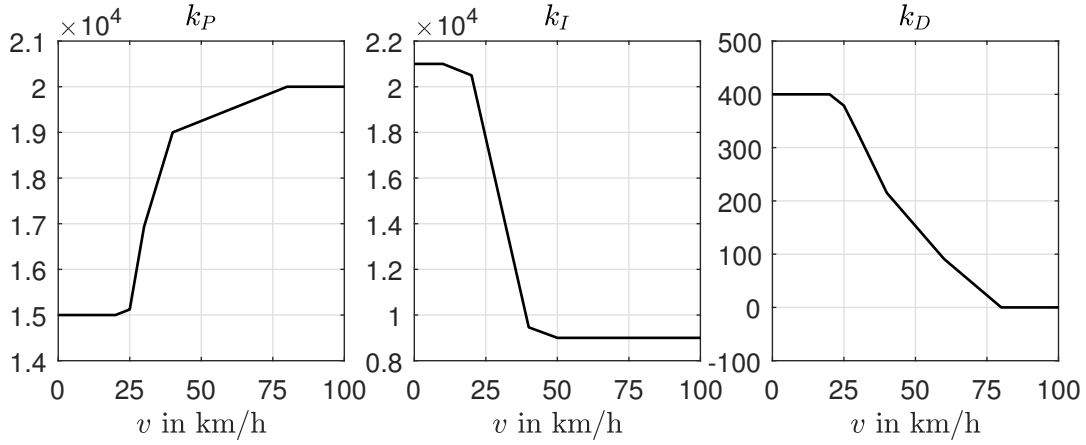

Figure 2.5: Vehicle speed dependent gain scheduling of the existing PID-controller. Data taken from [4]. The controller was tuned heuristically for several vehicle speeds. The scheduling of the parameters was implemented via Lookup-Tables.

One drawback of this controller design is, that the tuning was done empirically. This means, that it had no systematic background and took a lot of time to tune. Also, to avoid stability issues with the resonances of the system, the parameter gains had to be kept low, which resulted in a slow time response and big phase delays. These problems can be seen e.g. in a step steer maneuver, as shown in Figure 2.6.

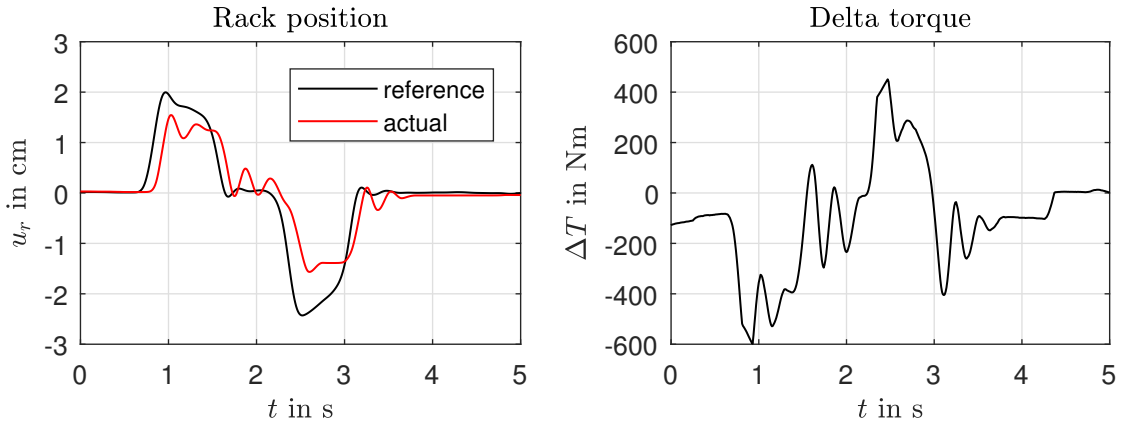

Figure 2.6: Step steer maneuver at $v = 30\,\text{kmh}$ with the existing PID controller. One can see clearly the delay until the steering rack starts moving. Furthermore, the steering rack starts to oscillate a little, since the controller was tuned very close to the limits of stability.

When doing a step experiment for a higher vehicle speed, these oscillations can get even worse. Figure 2.7 shows the same maneuver as Figure 2.6 with a higher speed of $v = 40\,\text{kmh}$.

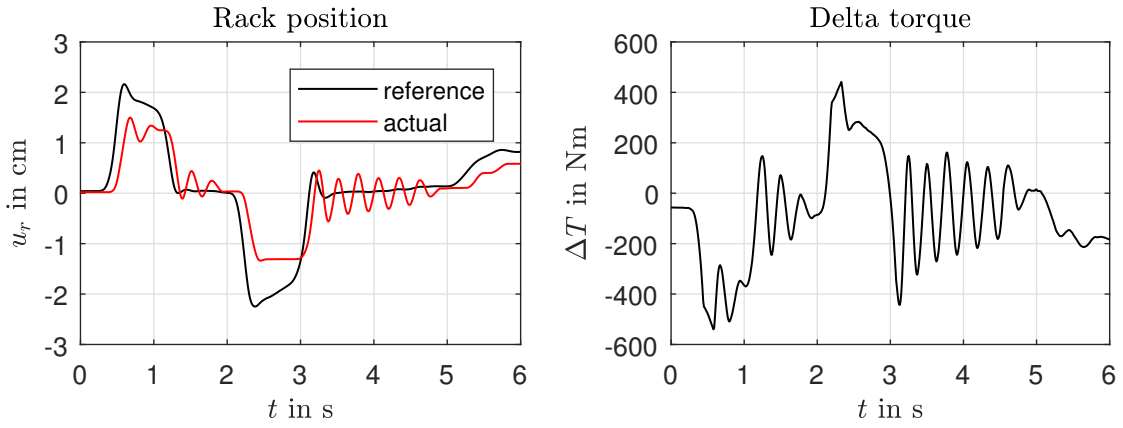

Figure 2.7: Step steer maneuver at $v = 40\,\text{kmh}$ with the existing PID controller. The system gets very close to the limits of stability. The resulting oscillation is producing a uncomfortable feeling for the driver.

It's in the interest of TKP to identify and investigate the source of this resonance problem. With a more complex controller design, these problems should be avoided and the performance of the overall system should be increased.

Therefore, the next logical step is to derive a proper mathematical model, that describes all the important characteristics of the system and build up controller concepts based on these representations. An optimal basis for common model-based controller theory is a linear model in state space form, which will be derived in the next chapter.

3 Linear vehicle modeling

With it's 27 DoF, the VTC model described in Section 2.2 is far too complex to allow a model-based controller design. Therefore, the mathematical relations have to be simplified in a way, that common controller theory can be applied. The modeling approach in this thesis will be a linear 2-track model for the lateral dynamics, separated from the longitudinal dynamics. To describe the movement of the vehicle, ISO 70000 standard is used (see Figure 3.1).

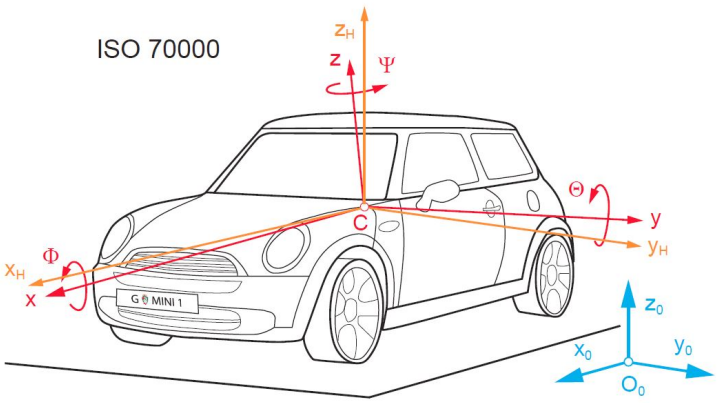

Figure 3.1: Vehicle coordinate system according to ISO 70000 [14]. The origin is located at the center of gravity (CoG).

The behavior of a real vehicle is strongly nonlinear. Therefore, a linear model of the vehicle does not represent the exact realistic behavior and bring significant errors with it. But it has to be clear, that the goal of this reduced model is not an optimal representation of the real car. It is more important, that the tendency, like characteristic frequencies and dynamics, matches reality properly.

For the validation of this reduced model, the VTC model can be used. This saves a lot of time, because otherwise, one has to make big efforts in measurements and experiments on the real car for a proper validation. Nevertheless, the steering rack model of the VTC model is not very accurate. Therefore, adjustments with measurement data as an addition will be necessary. Furthermore, the propulsion system of the BMW X5 with the electric motors and corresponding inverters are not modeled yet and will be taken into account in this approach.

In the end of this chapter, the derived model is compared to the VTC model as well as against measurement data from the real car. The resulting system is present in a state space realization, which is an optimal basis for linear controller theory.

3.1 Basic two-track model

3.1.1 Tire Forces

As the tire is the only element of a car, which interacts with it's surrounding, tire modeling is a very important part to get realistic simulations. There is a big variation of tire models on the market, beginning from simple mathematical to high level physical approaches. For example, the used TMeasy model in the VTC model consists of 54 parameters and has a 3rd order dynamic model included [10].

To get a linear tire model, a lot of assumptions have to be made. In Figure 3.2, one can see, that without a camber angle, all the coordinate systems of the wheel are at same position in the xy plane and everything is horizontally aligned. Also the static radius r_s is assumed to be constant for different wheel loads.

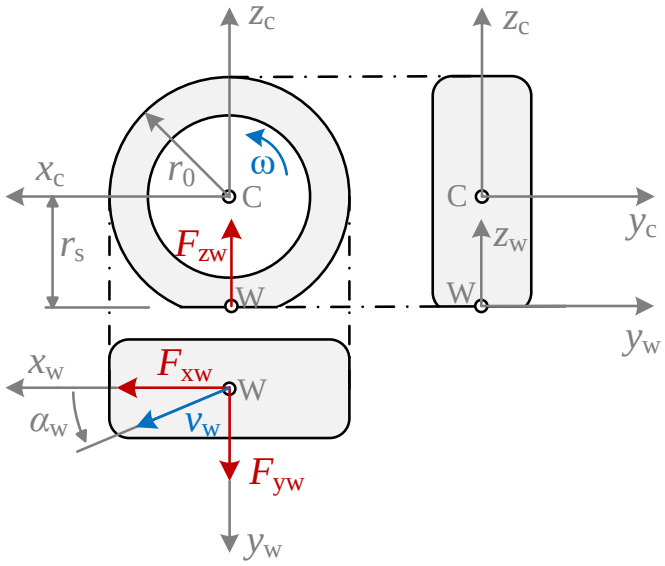

Figure 3.2: Illustration of a single wheel, based on ISO 8855 [14]. By neglecting tire masses and camber angle, the wheel contact point coordinate system W is on the same position as the wheel center coordinate system C with the static radius as a vertical offset. This means that all the forces, that act in the contact point W, act at the same value and direction in the wheel center C.

On real tires, forces are generated only in combination with slips. According to Rill [10], the longitudinal slip

$$s_x = \frac{-\left(v_{xw} - r_D\,\omega\right)}{r_D\,|\omega|} \tag{3.1}$$

is responsible for a longitudinal force F_{xw} and the slip angle

$$\alpha_w = \tan\frac{v_{yw}}{r_D\,|\omega|} \tag{3.2}$$

generates a lateral force F_{yw}. r_D denotes the dynamic rolling radius of the tire. It becomes more complex, if the longitudinal and lateral forces act in combination, as the tire has limits in force transmission. The well known friction ellipse describes these limits.

As a simplification, the longitudinal and lateral forces are separated from each other. Additionally, it is assumed that all the drive torque is fully transferred into a longitudinal force, which means that the slip quantity is not needed. Only a wheel load dependent roll friction (based on [10]) acts against the movement. Therefore, the longitudinal force can be written as

$$F_{\mathrm{xw}} = \frac{T_{\mathrm{dw}}}{r_{\mathrm{s}}} - F_{\mathrm{zw}}\, f_{\mathrm{rw}}\, \frac{r_0}{r_{\mathrm{s}}} \tag{3.3}$$

where T_{dw} is the drive torque, r_{s} the static tire radius, F_{zw} the wheel load, r_0 the unloaded tire radius and f_{rw} the coefficient of roll friction. The lateral tire force is a nonlinear dependency of the slip angle α_{w} and wheel load F_{zw}. As depicted in Figure 3.3, the lateral tire force consists of a linear range until slip angles of $|\alpha_{\mathrm{w}}| < 3°$ and a saturation range for higher values. Therefore, we can suppose a linear characteristic if the assumption of small slip angles holds.

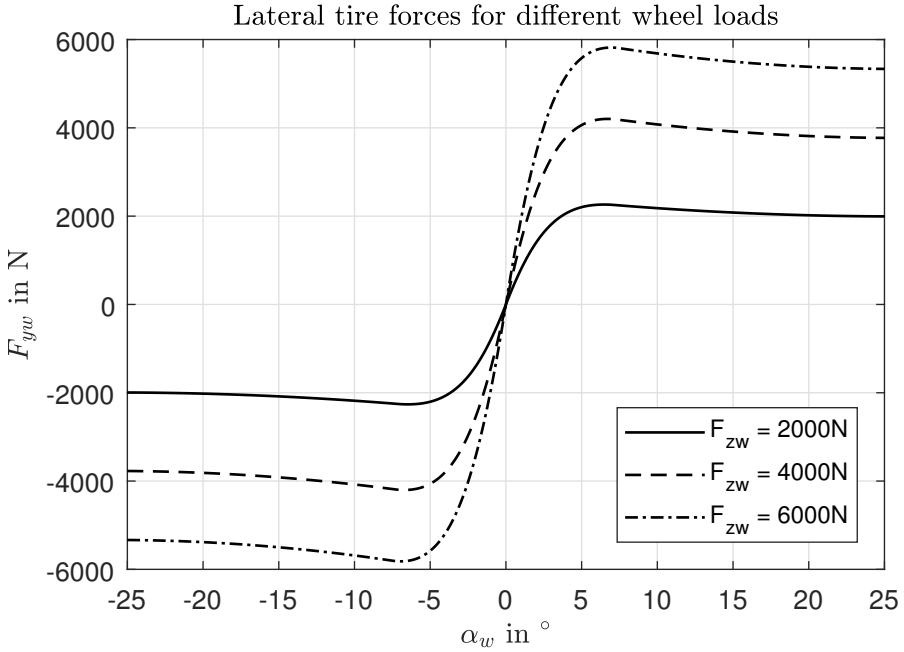

Figure 3.3: Lateral force dependent on slip angle α_{w} for different loads F_{zw} of the tire used on the BMW X5 from the validated TMeasy tire model. One can see a degressive behavior of the tire. With rising wheel loads, the lateral force capability gets smaller in a relative sense.

For this use case, the degressive influence of F_{zw} on the lateral force does not have any practical significance and is not further investigated. Therefore a linear approximation around a nominal load F_{zn} is sufficient. The resulting lateral force can be calculated by

$$F_{\mathrm{yw}} = -c_{\mathrm{a}}\, \alpha_{\mathrm{w}} \frac{F_{\mathrm{zw}}}{F_{\mathrm{zn}}} \tag{3.4}$$

with c_{a} as the cornering stiffness at the nominal load F_{zn}. Changes in the wheel loads F_{zw} come from load transfer due to lateral accelerations of the vehicle and is discussed later in Section 3.1.4.

3.1.2 Model equations around the center of gravity

As a next step, the model equations for vehicle movement around the center of gravity will be derived. The resulting model is a two track model without vertical movement, roll and pitch motion and is based on the work of W. Hirschberg [14] and G. Rill [10]. All given vectors are related to the vehicle fixed coordinate system located in the CoG as shown in Figure 3.4. First, the acceleration vector of the vehicle has to be derived. It

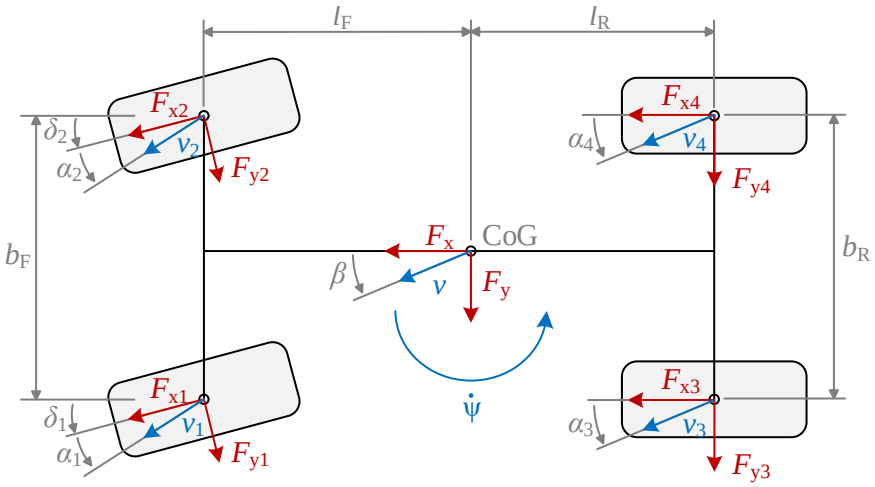

Figure 3.4: Vector orientation of the two track model, based on [14]. The described movement is limited to the xy-plane and yaw-movement around the CoG. All angles and vectors are depicted in positive sense and do not represent a realistic driving state.

consists of two parts, one from the translatory movement of the vehicle and one from the rotatory momentum around the z-axis, which is also known as centrifugal acceleration. By calculation of

$$\boldsymbol{a} = \dot{\boldsymbol{v}} + \boldsymbol{\omega} \times \boldsymbol{v} = \begin{bmatrix} \dot{v}_\mathrm{x} \\ \dot{v}_\mathrm{y} \\ 0 \end{bmatrix} + \begin{bmatrix} 0 \\ 0 \\ \dot{\psi} \end{bmatrix} \times \begin{bmatrix} v_\mathrm{x} \\ v_\mathrm{y} \\ 0 \end{bmatrix}, \tag{3.5}$$

the accelerations in x and y direction are given by

$$a_\mathrm{x} = \dot{v}_\mathrm{x} - \dot{\psi}\, v_\mathrm{y} \tag{3.6}$$

$$a_\mathrm{y} = \dot{v}_\mathrm{y} + \dot{\psi}\, v_\mathrm{x}. \tag{3.7}$$

According to Newton's 2nd law, the equations of motion for translatory movements can now be stated as

$$m\left(\dot{v}_\mathrm{x} - \dot{\psi}\, v_\mathrm{y}\right) = F_{\mathrm{x}1}\cos\delta_1 - F_{\mathrm{y}1}\sin\delta_1 + F_{\mathrm{x}2}\cos\delta_2 - F_{\mathrm{y}2}\sin\delta_2 + F_{\mathrm{x}3} + F_{\mathrm{x}4} \tag{3.8}$$

$$m\left(\dot{v}_\mathrm{y} + \dot{\psi}\, v_\mathrm{x}\right) = F_{\mathrm{x}1}\sin\delta_1 + F_{\mathrm{y}1}\cos\delta_1 + F_{\mathrm{x}2}\sin\delta_2 + F_{\mathrm{y}2}\cos\delta_2 + F_{\mathrm{y}3} + F_{\mathrm{y}4} \tag{3.9}$$

with m as the overall vehicle mass, δ_1, δ_2 as the steering angles and $F_{\mathrm{x}w}, F_{\mathrm{y}w}$ as the tire forces on all wheels. The yaw movement can be described via the equilibrium of torques around the z-axis. With Θ as the overall inertia of the chassis, $l_\mathrm{f}, l_\mathrm{r}$ as the distances from the CoG to front and rear axle and $b_\mathrm{f}, b_\mathrm{r}$ as the track width's of both axles, the third

equation of motion is given by

$$\begin{aligned}\Theta\,\ddot{\psi} = {} & l_\mathrm{f}\,(F_\mathrm{x1}\sin\delta_1 + F_\mathrm{y1}\cos\delta_1) - b_\mathrm{f}/2\,(F_\mathrm{x1}\cos\delta_1 - F_\mathrm{y1}\sin\delta_1)\\ & + l_\mathrm{f}\,(F_\mathrm{x2}\sin\delta_2 + F_\mathrm{y2}\cos\delta_2) + b_\mathrm{f}/2\,(F_\mathrm{x2}\cos\delta_2 - F_\mathrm{y2}\sin\delta_2)\\ & - l_\mathrm{r}\,F_\mathrm{y3} - b_\mathrm{r}/2\,F_\mathrm{x3}\\ & - l_\mathrm{r}\,F_\mathrm{y4} + b_\mathrm{r}/2\,F_\mathrm{x4}.\end{aligned} \tag{3.10}$$

In a regular vehicle, the steering angles rarely exceed $|\delta_i| > 20°$. Therefore, the trigonometric functions can be approximated by

$$\begin{aligned} sin\,\delta_1 &\approx \delta_1 \qquad & sin\,\delta_2 &\approx \delta_2\\ cos\,\delta_1 &\approx 1 \qquad & cos\,\delta_2 &\approx 1.\end{aligned} \tag{3.11}$$

The rear wheels are not driven, and as this model does not consider brakes, the longitudinal forces F_3 and F_4 are generating only rolling resistance and are assumed to be at same size. This means that

$$F_\mathrm{x4} - F_\mathrm{x3} = 0. \tag{3.12}$$

Applying these assumptions, the equations of motion simplify to:

$$m\left(\dot{v}_\mathrm{x} - \dot{\psi}\,v_\mathrm{y}\right) = F_\mathrm{x1} + F_\mathrm{x2} + F_\mathrm{x3} + F_\mathrm{x4} - F_\mathrm{y1}\,\delta_1 - F_\mathrm{y2}\,\delta_2 \tag{3.13}$$

$$m\left(\dot{v}_\mathrm{y} + \dot{\psi}\,v_\mathrm{x}\right) = F_\mathrm{y1} + F_\mathrm{y2} + F_\mathrm{y3} + F_\mathrm{y4} + F_\mathrm{x1}\,\delta_1 + F_\mathrm{x2}\,\delta_2 \tag{3.14}$$

$$\begin{aligned}\theta\,\ddot{\psi} = {} & l_\mathrm{f}\,(F_\mathrm{y1} + F_\mathrm{y2} + F_\mathrm{x1}\,\delta_1 + F_\mathrm{x2}\,\delta_2)\\ & - b_\mathrm{f}/2\,(F_\mathrm{x1} - F_\mathrm{x2} - F_\mathrm{y1}\,\delta_1 + F_\mathrm{y2}\,\delta_2)\\ & - l_\mathrm{r}\,(F_\mathrm{y3} + F_\mathrm{y4})\,.\end{aligned} \tag{3.15}$$

As a next step, the side slip angle β is introduced. It describes the position of x-axis relative to the movement of the vehicle. For small side slip angles, lateral and longitudinal velocities plus their derivatives can be approximated by

$$\begin{aligned} v_\mathrm{x} &= v\cos\beta \approx v\\ v_\mathrm{y} &= v\sin\beta \approx v\,\beta\\ \dot{v}_\mathrm{x} &= \dot{v}\cos\beta - v\sin\beta\,\dot{\beta} \approx \dot{v} - v\,\beta\,\dot{\beta}\\ \dot{v}_\mathrm{y} &= \dot{v}\sin\beta + v\cos\beta\,\dot{\beta} \approx \dot{v}\,\beta + v\,\dot{\beta}\end{aligned} \tag{3.16}$$

It is assumed, that the vehicle velocity v is changing slowly, which means that $\dot{v} \approx 0$. Then, the final equations of motion for the lateral dynamics can be stated as

$$m\,v\left(\dot{\beta} + \dot{\psi}\right) = F_\mathrm{y1} + F_\mathrm{y2} + F_\mathrm{y3} + F_\mathrm{y4} + F_\mathrm{x1}\,\delta_1 + F_\mathrm{x2}\,\delta_2 \tag{3.17}$$

$$\begin{aligned}\theta\,\ddot{\psi} = {} & l_\mathrm{f}\,(F_\mathrm{y1} + F_\mathrm{y2} + F_\mathrm{x1}\,\delta_1 + F_\mathrm{x2}\,\delta_2)\\ & - b_\mathrm{f}/2\,(F_\mathrm{x1} - F_\mathrm{x2} - F_\mathrm{y1}\,\delta_1 + F_\mathrm{y2}\,\delta_2)\\ & - l_\mathrm{r}\,(F_\mathrm{y3} + F_\mathrm{y4})\,.\end{aligned} \tag{3.18}$$

3.1.3 Tire velocities and slip angles

In order to calculate the slip angles of the tires, the vehicle velocities at each wheel center have to be determined first. With the actual vehicle speed, yaw rate and distance from CoG to wheel center, the velocity at the wheel center of the front left tire, depicted in the vehicle fixed coordinate system (Figure 3.4), can be calculated as

$$\boldsymbol{v}_{1,\mathrm{v}} = \boldsymbol{v} + \boldsymbol{\omega} \times \boldsymbol{r}_{\mathrm{vc1,v}} = \begin{bmatrix} v \\ v\,\beta \\ 0 \end{bmatrix} + \begin{bmatrix} 0 \\ 0 \\ \dot{\psi} \end{bmatrix} \times \begin{bmatrix} l_\mathrm{f} \\ \frac{b_\mathrm{f}}{2} \\ 0 \end{bmatrix} = \begin{bmatrix} v - \dot{\psi}\,\frac{b_\mathrm{f}}{2} \\ v\,\beta + \dot{\psi}\,l_\mathrm{f} \\ 0 \end{bmatrix}. \tag{3.19}$$

By taking the steering angle δ_1 into account, this velocity can be transformed into a wheel fixed coordinate system, which components are given by

$$v_{\mathrm{x1}} = \left(v - \dot{\psi}\,\frac{b_\mathrm{f}}{2}\right)\,\cos\delta_1 + \left(v\,\beta + \dot{\psi}\,l_\mathrm{f}\right)\sin\delta_1 \tag{3.20}$$

$$v_{\mathrm{y1}} = \left(v\,\beta + \dot{\psi}\,l_\mathrm{f}\right)\cos\delta_1 - \left(v - \dot{\psi}\,\frac{b_\mathrm{f}}{2}\right)\,\sin\delta_1. \tag{3.21}$$

Applying the approximation of the trigonometric functions from equation (3.11), these relations can be simplified to

$$v_{\mathrm{x1}} = v - \dot{\psi}\,\frac{b_\mathrm{f}}{2} + \left(v\,\beta + \dot{\psi}\,l_\mathrm{f}\right)\,\delta_1 \tag{3.22}$$

$$v_{\mathrm{y1}} = v\,\beta + \dot{\psi}\,l_\mathrm{f} - \left(v - \dot{\psi}\,\frac{b_\mathrm{f}}{2}\right)\,\delta_1. \tag{3.23}$$

As stated in Section 3.1.1, the longitudinal slip is set to $s_\mathrm{x} = 0$. With this assumption and with an approximation of $\tan\varphi \approx \varphi$ for small values of φ, the slip angle definition from equation (3.2) simplifies to

$$\alpha_\mathrm{w} \approx \frac{v_\mathrm{yw}}{v_\mathrm{xw}}. \tag{3.24}$$

Then, the slip angle of the front left tire can be calculated as

$$\alpha_1 \approx \frac{v_{\mathrm{y1}}}{v_{\mathrm{x1}}} = \frac{v\,(\beta - \delta_1) + \dot{\psi}\left(l_\mathrm{f} + \delta_1\,\frac{b_\mathrm{f}}{2}\right)}{v\,(1 + \delta_1\,\beta) - \dot{\psi}\left(\frac{b_\mathrm{f}}{2} - \delta_1\,l_\mathrm{f}\right)}. \tag{3.25}$$

Investigating this result, it can be noticed that for velocities $v > 5\,\mathrm{kmh}$

$$\begin{aligned} 1 &\gg |\delta_1\,\beta| \\ v &\gg \left|\dot{\psi}\left(\frac{b_\mathrm{f}}{2} - \delta_1\,l_\mathrm{f}\right)\right| \\ l_\mathrm{f} &\gg \left|\delta_1\frac{b_\mathrm{f}}{2}\right|, \end{aligned} \tag{3.26}$$

which can be applied to equation (3.25). Then, the slip angle can be approximated by the linear relation

$$\alpha_1 \approx \beta - \delta_1 + \dot{\psi}\frac{l_\mathrm{f}}{v}. \tag{3.27}$$

Similar to the front left wheel, the slip angles for the remaining wheels can be derived as

$$\alpha_2 \approx \beta - \delta_2 + \dot{\psi}\frac{l_\mathrm{f}}{v} \tag{3.28}$$

$$\alpha_3 \approx \beta - \dot{\psi}\frac{l_\mathrm{r}}{v} \tag{3.29}$$

$$\alpha_4 \approx \beta - \dot{\psi}\frac{l_\mathrm{r}}{v}. \tag{3.30}$$

For a better straight-line stability and corner entry handling, the wheels of the BMW X5 are orientated with a toe-in angle. As seen in Figure 3.5, toe is an angle formed by the center line of the wheel and the x axis of the vehicle fixed coordinate system, looking at the vehicle from above. If the lines meet in front of the car, this is known as toe-in [10].

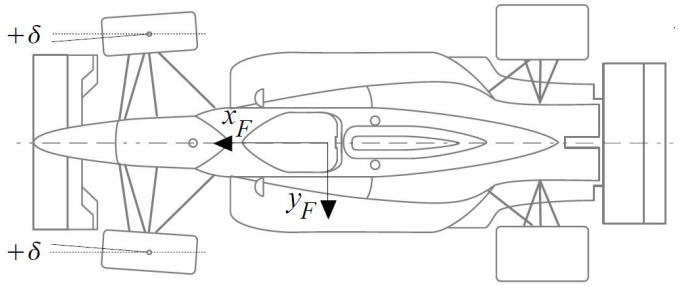

Figure 3.5: Toe-in angle on the front wheels [10]. This angle improves the straight-line stability and corner entry handling but increases the tire wear.

This angle also improves the stability of the model and can be easily considered in the slip angles of the tires. By using d_tf as a constant for the toe on the front wheels and d_tr for the rear wheels, the slip angles change to

$$\alpha_1 = \beta - \delta_1 + \dot{\psi}\frac{l_\mathrm{f}}{v} + d_\mathrm{tf} \tag{3.31}$$

$$\alpha_2 = \beta - \delta_2 + \dot{\psi}\frac{l_\mathrm{f}}{v} - d_\mathrm{tf} \tag{3.32}$$

$$\alpha_3 = \beta - \dot{\psi}\frac{l_\mathrm{r}}{v} + d_\mathrm{tr} \tag{3.33}$$

$$\alpha_4 = \beta - \dot{\psi}\frac{l_\mathrm{r}}{v} - d_\mathrm{tr}. \tag{3.34}$$

3.1.4 Lateral load transfer

Due to the lateral acceleration in cornering situations, the loads of the single wheels changes. This effect is called lateral load transfer. There is a similar effect for longitudinal acceleration, but as we consider only lateral dynamics, the longitudinal load transfer will be neglected.

The load transfer is mainly determined by the suspension design and the height of the CoG. To avoid additional degree's of freedom coming from suspension deflections, only the steady state behavior is considered. Mitterrutzner derived a simplified dynamic tire

load model in his thesis [15]. This model was adapted as followed:

$$F_{z1} = \frac{m\,g}{2} W_B - a_y \frac{m\,h_{CoG}}{b_f} R_B \tag{3.35}$$

$$F_{z2} = \frac{m\,g}{2} W_B + a_y \frac{m\,h_{CoG}}{b_f} R_B \tag{3.36}$$

$$F_{z3} = \frac{m\,g}{2} (1 - W_B) - a_y \frac{m\,h_{CoG}}{b_r} (1 - R_B) \tag{3.37}$$

$$F_{z4} = \frac{m\,g}{2} (1 - W_B) + a_y \frac{m\,h_{CoG}}{b_r} (1 - R_B) \tag{3.38}$$

With no lateral acceleration, the weight of the car is equally distributed to the wheels according to it's weight balance W_B, which is determined by

$$W_B = \frac{l_r}{l_f + l_r}. \tag{3.39}$$

Proportional to a lateral acceleration a_y, load is shifted towards the outer wheel in case of a cornering situation. The roll balance R_B as a constant parameter determines the load distribution on the front axle relative to the rear axle and is given by the overall suspension design. Other dependencies come from the height of the center of gravity h_{CoG} and the track widths b_f and b_r. In steady state, a_y can be approximated by

$$a_y \approx v \left(\dot{\beta} + \dot{\psi} \right) \approx v\,\dot{\psi}. \tag{3.40}$$

Inserted in the equations above, the final load transfer model is given by

$$F_{z1} = \frac{m\,g}{2} W_B - \dot{\psi}\,\frac{m\,v\,h_{CoG}}{b_f} R_B \tag{3.41}$$

$$F_{z2} = \frac{m\,g}{2} W_B + \dot{\psi}\,\frac{m\,v\,h_{CoG}}{b_f} R_B \tag{3.42}$$

$$F_{z3} = \frac{m\,g}{2} (1 - W_B) - \dot{\psi}\,\frac{m\,v\,h_{CoG}}{b_r} (1 - R_B) \tag{3.43}$$

$$F_{z4} = \frac{m\,g}{2} (1 - W_B) + \dot{\psi}\,\frac{m\,v\,h_{CoG}}{b_r} (1 - R_B)\,. \tag{3.44}$$

3.1.5 Steering rack model

For SbTV, the rack position u_r is an additional degree of freedom and has to be modeled as well. Dependent on the suspension and steering geometry, the tire forces and torques generate a force on the steering rack. The resulting force on the rack minus a friction force F_r is responsible for a movement of the rack. Figure 3.6 shows a illustration of the steering rack to understand the described relations.

To describe the movement of the rack, a compensation mass for the whole system needs to be determined. With this mass, all the subsystems, that are moving together with the rack are considered. Pfister and Reis in [9] did some investigations about this problem and calculated this compensation mass as

$$m_r = m_z + \theta_{EM} \left(\frac{2\,\pi\,i_{belt}}{i_{BLD}} \right)^2 + \theta_{BLD} \left(\frac{2\,\pi}{i_{BLD}} \right)^2 + 2\,\theta_{wheel} \left(\frac{1}{l_{sh}} \right)^2 \tag{3.45}$$

where m_z is the mass of the steering rack by itself, $\theta_{EM}, \theta_{BLD}, \theta_{wheel}$ the inertias of steering

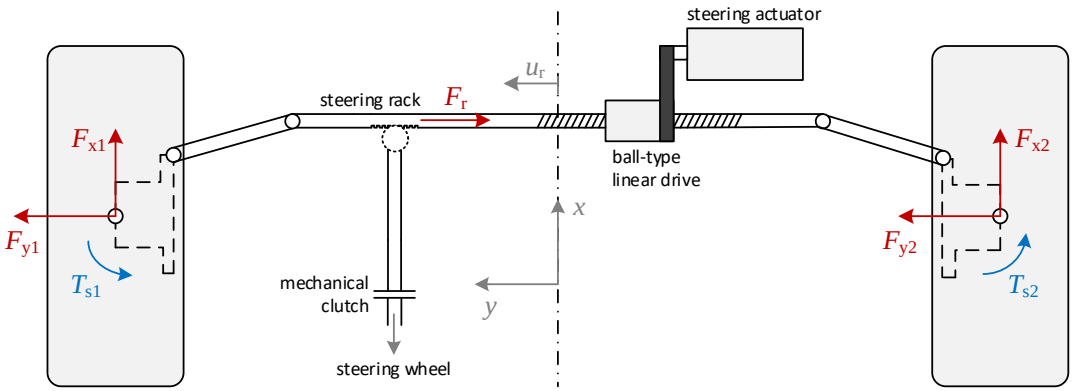

Figure 3.6: Schematic drawing of the steering rack. The tire forces generate a torque around the pivot, where the wheel carrier is connected to the tie rod. The sum of these torques and the self aligning torque of the wheel generate a force directly on the steering rack. As there are a lot of components installed from the SbW system (the steering column, steering actuator and the ball-type linear drive (BLD)), there is a lot of friction in the system.

actuator, BLD and wheel. i_{belt} is the transmission between the actuator and the BLD. i_{BLD} is the transmission between the BLD and the steering rack. l_{sh} is the lever length for the steering arm. With an equilibrium of forces on the steering rack, the movement of u_{r} can be described as

$$m_{\text{r}}\,\ddot{u}_{\text{r}} = F_{\text{l}} - F_{\text{r}}(\dot{u}_{\text{r}}) \tag{3.46}$$

with F_{l} as the sum of forces coming from the tires and $F_{\text{r}}(\dot{u}_{\text{r}})$ as the friction force. The friction inside the steering rack is quite complex, as it has asymmetric and dynamic behavior. Rohrmoser [16] developed a rack friction estimation based on the Lund-Grenoble friction model for a different SbW vehicle. Because of the complexity, the validation of the model is very time consuming and therefore inappropriate for the demands of this thesis. A more basic approach is the one, that Reiter used in his thesis [12], a Coulomb friction model of form

$$F_{\text{r}}(\dot{u}_{\text{r}}) = f_{\text{r}}\,\text{sign}(\dot{u}_{\text{r}}) + f_{\text{d}}\,\dot{u}_{\text{r}}. \tag{3.47}$$

Since the sign-function is unsuitable for simulation, it is replaced by a tanh-function which results as

$$F_{\text{r}}(\dot{u}_{\text{r}}) = f_{\text{r}}\tanh(\dot{u}_{\text{r}}\,k_{\text{fr}}) + f_{\text{d}}\,\dot{u}_{\text{r}}. \tag{3.48}$$

where f_{r} denotes the static friction, k_{fr} the slope of the tanh-function and f_{d} the damping coefficient of the system.

Usually, the transition of the tire forces to the rack force F_{l} is nonlinear, dependent on the suspension deflection and the steering angle. For this demands, this nonlinearities are neglected and replaced by linear relations. According to Reiter [12], longitudinal and vertical forces are counteracting, whereas the lateral forces and self alignment torques are acting in the same direction. With linear constants, the rack force then can be determined by

$$F_{\text{l}} = k_{\text{x}}\,(F_{\text{x1}} - F_{\text{x2}}) + k_{\text{y}}\,(F_{\text{y1}} + F_{\text{y2}}) + k_{\text{z}}\,(F_{\text{z1}} - F_{\text{z2}}) + r_{\text{M}}\,(M_{\text{s1}} + M_{\text{s2}})\,. \tag{3.49}$$

Supposing, that the lever arm n is constant, the self aligning torques can be described as a function of the lateral forces by

$$M_{s1} = -n\,F_{y1} \tag{3.50}$$
$$M_{s2} = -n\,F_{y2}. \tag{3.51}$$

Then the equation of motion for the rack position u_r results as

$$\begin{aligned} m_r\,\ddot{u}_r = {} & k_x\,(F_{x1} - F_{x2}) + (k_y - n\,r_M)\,(F_{y1} + F_{y2}) + k_z\,(F_{z1} - F_{z2}) \\ & - f_r\,\tanh \dot{u}_r/k_{fr} - f_d\,\dot{u}_r. \end{aligned} \tag{3.52}$$

In today's cars, the steering angle of the inner wheel in a cornering situation is higher than the steering angle of the outer wheel. The most common steering geometry is the Ackermann Steering geometry [2]. For the demands of this model, however, the steering geometry is assumed to be linear with the same steering angles left and right. Then, the steering angle can be described proportional to the rack position as

$$\delta_1 = \delta_2 = k_d\,u_r. \tag{3.53}$$

The steering transmission k_d can be determined by an average point of the real steering geometry. For steering angles up to $|\delta_i| < 10°$, this assumption holds pretty good.

3.1.6 Drive train

At the moment, the model has 2 input parameters, the drive torques on the front wheels T_{d1} and T_{d2}. Since the average torque of T_{d1} and T_{d2} has no influence regarding SbTV, the torques can be transformed to

$$T_{d1} = T + \Delta T \tag{3.54}$$
$$T_{d2} = T - \Delta T \tag{3.55}$$

with the longitudinal torque T and the delta torque ΔT. According to the assumption that $\dot{v} = 0$, T can be approximated in steady state as a function of the drag- and the rolling resistance:

$$T \approx \frac{1.25}{4}\,r_s\,c_d\,A_f\,v^2 + 2\,r_0\,f_{rw}\,F_{zn} \tag{3.56}$$

The system is therefore reduced to 1 input parameter, the delta Torque ΔT. In the real system, this torque cannot be generated instantly. The inverters with their related motors are control systems by itself that need time to build up the required torques. The easiest way to model this behavior is a 1st order dynamics of form

$$\tau \Delta\dot{T} = -\Delta T + \Delta T_{req} \tag{3.57}$$

where τ is a time constant and ΔT_{req} the requested delta torque as input parameter.

3.2 Validation

The derived model in the previous section needs to be validated. For most of the necessary parameters, the VTC model in SbW mode can be used. For the other parameters, that aren't accessible in a direct way need to be validated through special simulations or with measurement data from the real car.

3.2.1 General vehicle parameters

The geometric parameters, the vehicle mass and the overall inertia was validated by Reiter in [12] and can be used directly. The track width of the front axle is about 7 cm wider than the width of the rear axle, which comes from installed spacers on the front wheel carriers. This increases the normalized steering offset as mentioned in Figure 1.3 and improves the performance of SbTV.

For the lateral load transfer model from section 3.1.4 two additional parameters are needed. The weight balance can be calculated as shown in equation (3.39) to

$$W_{\mathrm{B}} = \frac{l_{\mathrm{r}}}{l_{\mathrm{f}} + l_{\mathrm{r}}} = \frac{1.349\,\mathrm{m}}{1.349\,\mathrm{m} + 1.580\,\mathrm{m}} = 0.459, \tag{3.58}$$

which means, that about 46 % of the vehicle mass is laying on the front axle. The roll balance R_{B} represents the suspension dependent load distribution between the front and rear axle. This parameter is not directly available and needs to be validated by experiments. Therefore, a so called *ramp-steer-maneuver* has been simulated, where the rack position follows a ramp signal at a constant vehicle speed. With the wheel loads of all 4 tires, the roll balance then can be calculated by

$$R_{\mathrm{B}} = \frac{\frac{F_{\mathrm{z2}} - F_{\mathrm{z1}}}{2}}{\frac{F_{\mathrm{z2}} - F_{\mathrm{z1}}}{2} + \frac{F_{\mathrm{z4}} - F_{\mathrm{z3}}}{2}} = \frac{F_{\mathrm{z2}} - F_{\mathrm{z1}}}{F_{\mathrm{z2}} - F_{\mathrm{z1}} + F_{\mathrm{z4}} - F_{\mathrm{z3}}} \tag{3.59}$$

for different lateral accelerations a_{y} and is shown in Figure 3.7.

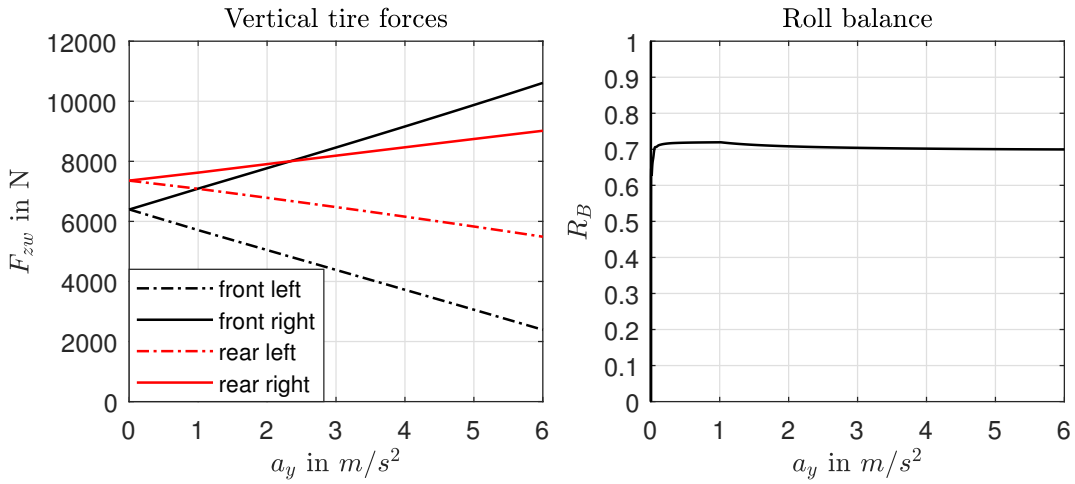

Figure 3.7: Ramp steer maneuver at $v = 30\,\mathrm{km/h}$ to determine the roll balance. One can see, that the load transfer on the front axle is much higher, than on the rear axle. This represents a high roll stiffness on the front, which is necessary to guarantee a understeering behavior of the car. With the resulting wheel loads, the roll balance then can be calculated and is shown in the left plot.

The roll balance is nearly constant for a wide range of a_y until the first wheel tips up. But as tipping up is hardly possible with SbTV (since there is always traction necessary to generate the delta torque), the roll balance can be considered as constant. An average value out of Figure 3.9 can be determined as

$$R_B = 0.711. \tag{3.60}$$

All the general vehicle parameters are summarized in Table 3.1.

Table 3.1: General vehicle parameters. All parameters, except W_B and R_B, have been taken from [12].

Param.	Value	Description
l_f	1.580 m	Distance from CoG to front axle
l_r	1.349 m	Distance from CoG to rear axle
b_f	1.714 m	Track width of front axle
b_r	1.650 m	Track width of rear axle
m	2804.3 kg	Overall vehicle mass incl. 2 drivers
θ	6525 kg m^2	Inertia of the vehicle around z-axis
W_B	0.459	Weight balance
R_B	0.711	Roll balance
h_{CoG}	0.585 m	Height of the center of gravity

3.2.2 Rack parameters

To analyze the steering geometry and the toe angles, another ramp steer with a very low vehicle speed has been simulated. The low velocity is needed to avoid deflections in the suspensions (bump steer effect) and other dynamic effects which could influence this isolated experiment. In Figure 3.8, the results of this simulation are shown.

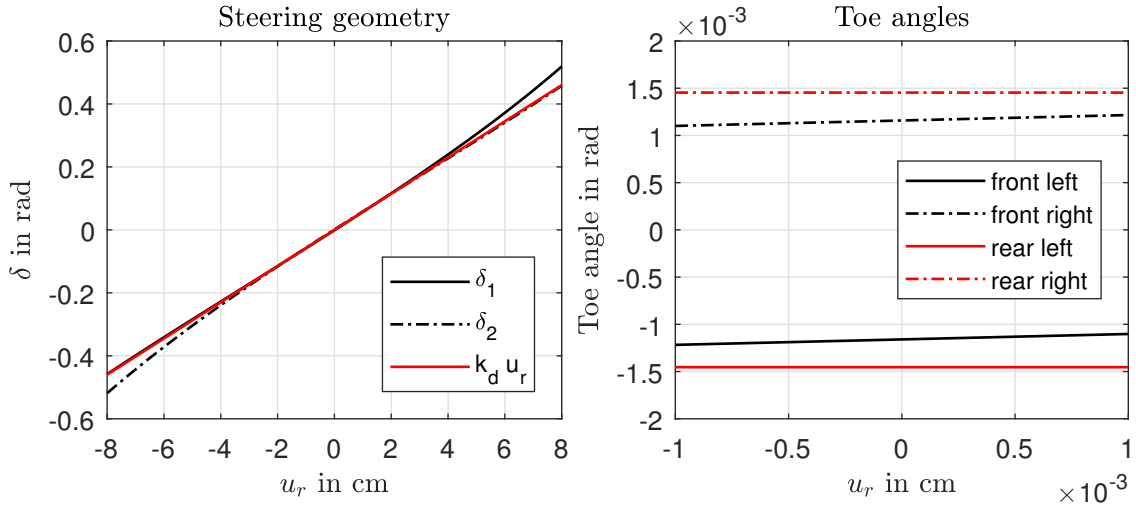

Figure 3.8: Ramp steer with very low vehicle speed to analyze the steering geometry of the car. In the left plot, one can see the Ackermann steering geometry, where the inner wheel have a higher steering angle than the outer wheel. For this model, a linear approximation (as depicted with the red graph) is sufficient. With a zoom around the origin, the toe angles on the front and rear axle can be determined.

For rack positions smaller than $u_\mathrm{r} < |4\,\mathrm{cm}|$, the linear approximation

$$\delta_1 = \delta_2 = k_\mathrm{d}\, u_\mathrm{r} = 5.75\, u_\mathrm{r} \tag{3.61}$$

is sufficient. For higher steering angles, this approximation produces some slight errors. The toe angles are constant for the whole range uf u_r and are modeled by

$$d_\mathrm{tf} = 0.0012\,\mathrm{rad} \tag{3.62}$$
$$d_\mathrm{tr} = 0.0014\,\mathrm{rad}. \tag{3.63}$$

In order to validate the gains of the tire forces and self aligning torque to rack force, the suspension model from Reiter [12] can be used. With this model, the gains can be analyzed for different rack positions and suspension deflections. Figure 3.9 show these gains for both of the front tires with zero suspension deflection.

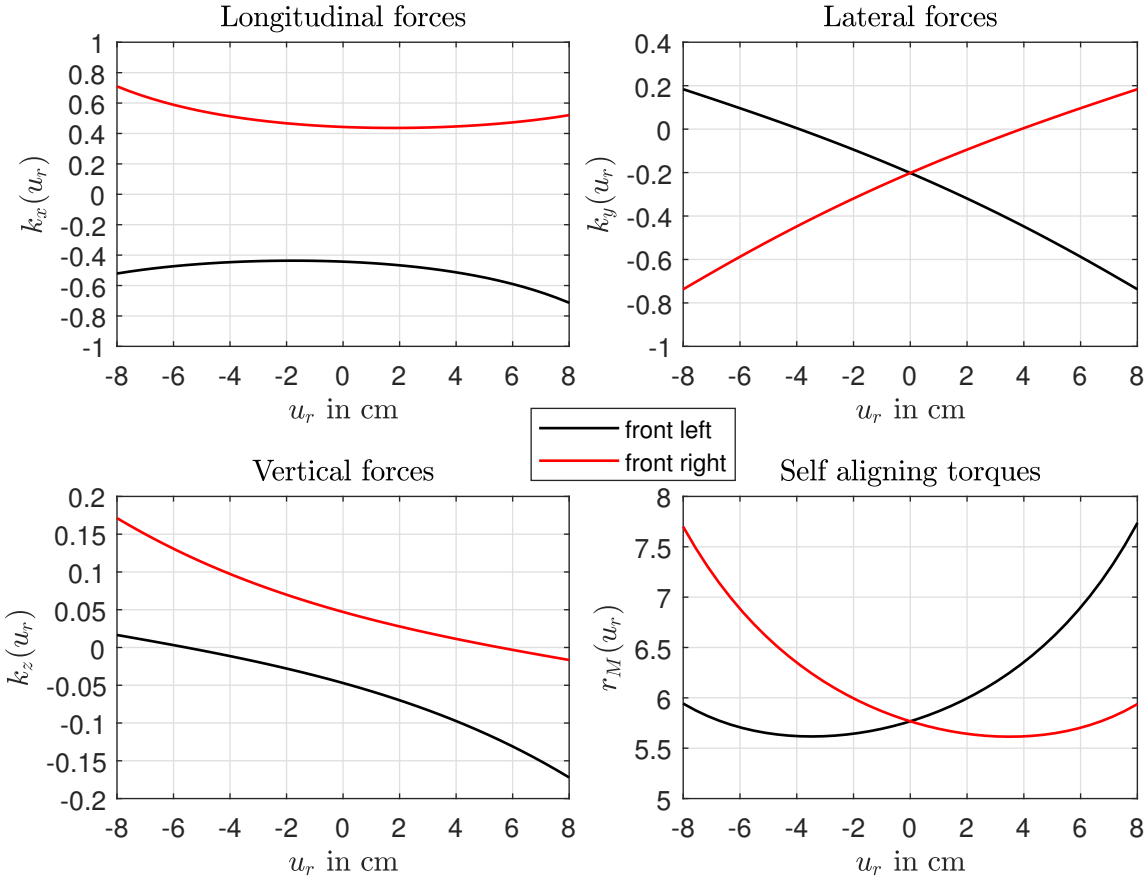

Figure 3.9: Gains of the transition from tire forces and self aligning torque to rack force with zero suspension deflection [12]. One can see that the rack forces influences these gains in a non linear way. In the origin, the value for k_x and k_z have the same value but opposite sign. This means that the longitudinal and vertical forces are counteracting.

According to equation (3.52), constant gains are necessary to get a linear relation. Therefore, the gains had been taken out of the data from Figure 3.9 at $u_\mathrm{r} = 0$:

$$\begin{aligned} k_\mathrm{x} &= -0.440 & k_\mathrm{y} &= -0.200 \\ k_\mathrm{z} &= -0.045 & r_\mathrm{M} &= 5.775\,m^{-1} \end{aligned} \tag{3.64}$$

With equation (3.45) and the parameters from Table 3.2, Pfister and Reis[9] calculated a rack compensation mass of $m_\mathrm{r} = 1057\,\mathrm{kg}$, that describes the characteristic frequency of the rack.

Table 3.2: Parameters for calucation of rack compensation mass from [9].

Param.	Value	Description
m_z	$2.3\,\mathrm{kg}$	Mass of steering rack
θ_EM	$0.0003\,\mathrm{kg\,m^2}$	Inertia of steering actuator
θ_BLD	$0.0006628\,\mathrm{kg\,m^2}$	Inertia of ball-type linear drive
θ_wheel	$0.8457\,\mathrm{kg\,m^2}$	Inertia of a single wheel
i_belt	2.41	Transmission between steering actuator and BLD
i_BLD	$0.01\,\mathrm{m/U}$	Transmission between BLD and steering rack
l_sh	$0.18\,\mathrm{m}$	Lever length for the steering arm

According to measurements (see Figure 3.10), this frequency lies at $f_\mathrm{rack} = 3.2\,\mathrm{Hz}$. To match the real frequency of the BMW X5, this virtual mass has to be higher than the calculation from [9]. With

$$m_\mathrm{r} = 1900\,\mathrm{kg}, \tag{3.65}$$

the model reproduces exactly a resonance frequency of 3.2 Hz.

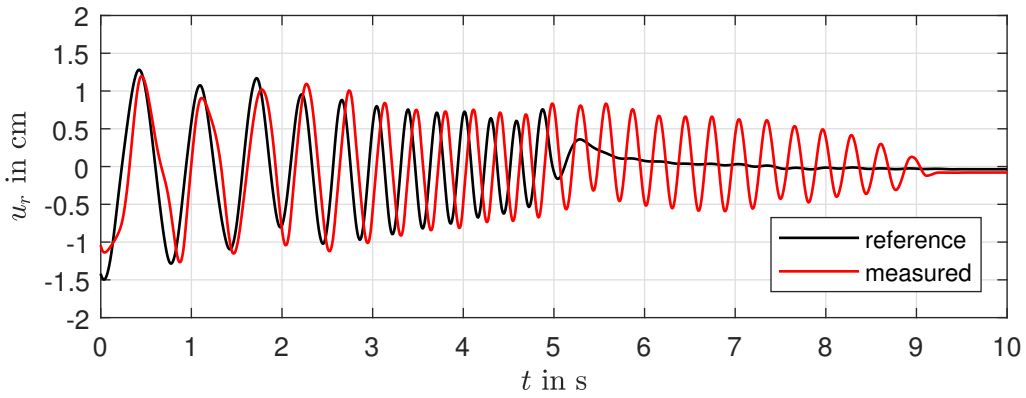

Figure 3.10: Resonance effect on the steering rack. At this measurement, a sweep maneuver caused some characteristic oscillations. The rack compensation mass describes the frequency of this oscillation.

The parameters for the friction model have been taken from internal engineers at TKP. They have the values

$$f_\mathrm{d} = 5000\,\mathrm{Ns\,m^{-1}} \tag{3.66}$$

$$f_\mathrm{r} = 300\,\mathrm{N}. \tag{3.67}$$

In Table 3.3, the parameters from this section are summarized.

Table 3.3: Parameters of the steering rack.

Param.	Value	Description
k_d	$5.75\,\mathrm{rad\,m^{-1}}$	Transmission of rack to steering angle
d_tf	$0.0012\,\mathrm{rad}$	Toe angle front
d_tr	$0.0014\,\mathrm{rad}$	Toe angle rear
k_x	-0.440	Gain of longitudinal force to rack force
k_y	-0.2	Gain of lateral force to rack force
k_z	-0.045	Gain of vertical force to rack force
r_M	$5.775\,\mathrm{m^{-1}}$	Gain from self aligning moments to rack force
m_r	$886\,\mathrm{kg}$	Compensation mass of the steering rack
f_d	$5000\,\mathrm{Ns\,m^{-1}}$	Damping coefficient of rack
f_r	$300\,\mathrm{N}$	Static rack friction

3.2.3 Wheel parameters

The parameters regarding the tire, can be calculated by the TMeasy validation from Esser [11] and by the definitions according to Rill [10]. For the nominal vertical load, a 4th of the overall mass

$$F_\mathrm{zn} = \frac{m\,g}{4} = \frac{2804.3\,\mathrm{kg}\ 9.81\,\mathrm{m/s^2}}{4} = 6877.5\,\mathrm{N} \tag{3.68}$$

has been chosen. Since the tire was parametrized for $F_\mathrm{zn1} = 4500\,\mathrm{N}$ and $F_\mathrm{zn2} = 9000\,\mathrm{N}$, the parameters need to be interpolated by proper relations [10]. The static radius r_s at the nominal wheel load can be calculated by

$$r_\mathrm{s} = r_0 - \Delta z \approx r_0 - \frac{F_\mathrm{zn}}{c_\mathrm{z}} = 0.369\,\mathrm{m} - \frac{6877.5\,\mathrm{N}}{300000\,\mathrm{N/m}} = 0.346\,\mathrm{m} \tag{3.69}$$

where c_z is the vertical tire stiffness at F_zn. The cornering stiffness of the tire can be calculated by

$$c_\mathrm{a} = \frac{F_\mathrm{zn}}{F_\mathrm{zn1}} \left(2\,c_\mathrm{a,n1} - 0.5\,c_\mathrm{a,n2} - (c_\mathrm{a,n1} - 0.5\,c_\mathrm{a,n2})\,\frac{F_\mathrm{zn}}{F_\mathrm{zn1}} \right) = 126160\,\mathrm{N/rad}. \tag{3.70}$$

The length of the lever arm n is difficult to calculate, since it is influenced by a lot of effects such as pneumatic trail, castor offset at ground or some angles of the suspension geometry. Hence, this parameter was tuned with a least squares error analysis in the simulation to match the behavior of the VTC model as close as possible. For a value of

$$n = 0.0835\,\mathrm{m}, \tag{3.71}$$

the error of the steady state steering rack position for various step inputs at different vehicle speeds minimizes. The rolling resistance coefficient was given by the value of

$$f_\mathrm{rw} = 0.0075. \tag{3.72}$$

The parameters validated in this section are summarized in Table 3.4.

Table 3.4: Tire parameters. The lever arm for the self aligning torque was tuned via a least squares error analysis.

Param.	Value	Description
r_0	0.369 m	Unloaded radius of tire
r_s	0.346 m	Static radius of tire @ F_{zn}
c_a	126160 N rad^{-1}	Cornering stiffness of tire @ F_{zn}
F_{zn}	6877.5 N	Nominal vertical wheel load
n	0.0835 m	Lever arm for self aligning torque
f_{rw}	0.0075	Rolling resistance coefficient

3.2.4 Drive train parameters

The drive train with the inverter and motors are not modeled in the VTC model yet. Therefore, the validation has to be done with measurement data. Internal engineers at TKP did sweep tests with the existent SbTV controller, one of these tests is shown in Figure 3.11.

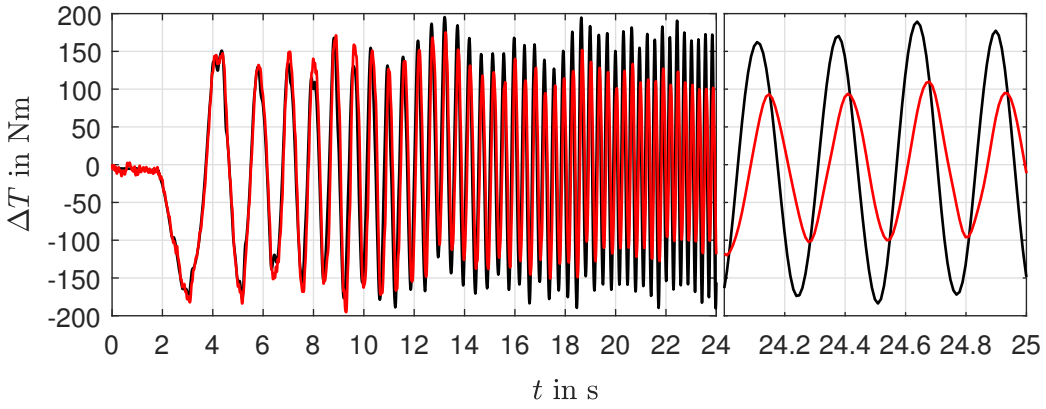

Figure 3.11: Sweep test with SbTV. The black line depicts the requested differential Torque ΔT_{req}, the red line is the estimated actual delta torque ΔT. The estimation is based on the inverter current and is the only available measurement data for the actual torque. For higher frequencies, the actual torque has a lower amplitude than the requested torque. In the zoomed plot on the right side, also a remarkable phase delay is noticeable.

The time constant τ, according to the modeling in Section 3.1.6, has been tuned manually until the behavior of Figure 3.11 was reconstructed properly. For a value of

$$\tau = 0.06\,\text{s}, \tag{3.73}$$

the filtered requested torque matches the actual torque estimate very well. Figure 3.12 shows the results of this validation.

The parameters for the air drag had been taken from [12] and have the values

$$c_d = 0.38 \tag{3.74}$$

$$A_f = 2.9\,\text{m}^2. \tag{3.75}$$

Table 3.5 summarizes the validated parameters in this section.

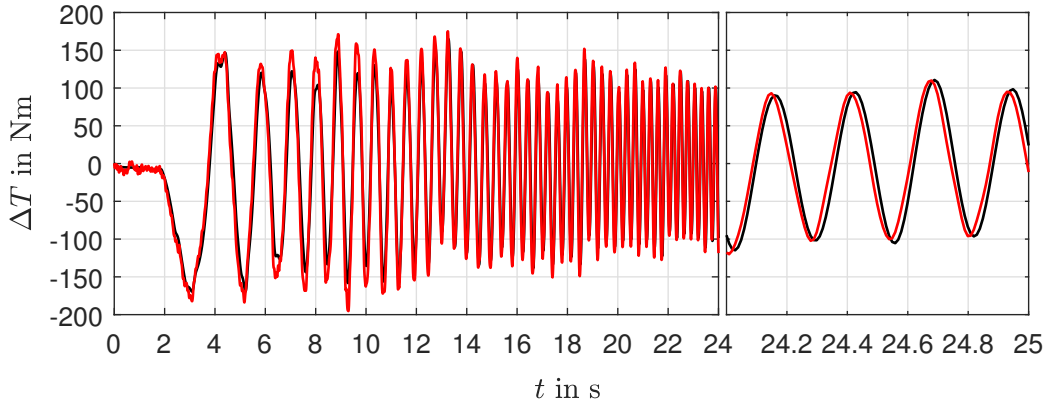

Figure 3.12: Filtered requested torque against the actual torque estimate for the sweep test from Figure 3.11. The black line is the filtered requested torque with a 1st order dynamics and time constant $\tau = 0.06\,\mathrm{s}$. Now, both signals are matching very good. Also the phase delay is considered sufficiently with this approach.

Table 3.5: Parameters for the drive train. The time constant τ has been tuned manually with measurement data from internal TKP engineers.

Param.	Value	Description
τ	$0.06\,\mathrm{s}$	Time constant of inverter-motor-model
c_d	0.38	Drag resistance of air
A_f	$2.9\,\mathrm{m}^2$	Frontal area of the vehicle

3.3 Frequency domain

For the use of conventional controller theory, the derived model relations need to be combined and transformed into the frequency domain. Therefore, a state space realization needs to be derived first.

3.3.1 State space realization

By combining all the model relations of equations (3.1) to (3.57), the behavior can be described in 4 equations of form

$$\dot{\beta} = A_{11}\,\beta + A_{12}\,\dot{\psi} + A_{13}\,u_\mathrm{r} + A_{15}\,\Delta T \tag{3.76}$$

$$\ddot{\psi} = A_{21}\,\beta + A_{22}\,\dot{\psi} + A_{23}\,u_\mathrm{r} + A_{25}\,\Delta T + N_{21}\,\dot{\psi}\,u_\mathrm{r}^2 + N_{22}\,\dot{\psi}^2\,u_\mathrm{r} + N_{23}\,\beta\,\dot{\psi}\,u_\mathrm{r} \tag{3.77}$$

$$\ddot{u}_\mathrm{r} = A_{41}\,\beta + A_{42}\,\dot{\psi} + A_{43}\,u_\mathrm{r} + A_{44}\,\dot{u}_\mathrm{r} + A_{45}\,\Delta T + N_{41}\,\tanh\dot{u}_\mathrm{r}\,N_{42} \tag{3.78}$$

$$\Delta\dot{T} = A_{55}\,\Delta T + B_5\,\Delta T_\mathrm{req} \tag{3.79}$$

with the coefficients A_{ij}, B_i for the linear part of the model and N_{ij} for the non-linear part. These coefficients are constant with dependency of the vehicle speed. The derivation of these coefficients can be found in the Appendix. Because of

$$\beta,\ \dot{\psi},\ u_\mathrm{r} \ll 1, \tag{3.80}$$

the influence of the non-linearities in equation (3.77) is very small. Thus, the non-linearities can be omitted without any compromises. Nevertheless, the static friction of the rack, described by the coefficients N_{41}, N_{42} in equation (3.78), influences the behavior of the

steering rack strongly and is impossible to linearize them in a useful way. Therefore, to get a linear model, the static friction has to be omitted, despite the fact that it represents a major drawback if it is not considered. By introducing a state vector and the input of form

$$\boldsymbol{x} = \begin{bmatrix} x_1 \\ x_2 \\ x_3 \\ x_4 \\ x_5 \end{bmatrix} = \begin{bmatrix} \beta \\ \dot{\psi} \\ u_\mathrm{r} \\ \dot{u}_\mathrm{r} \\ \Delta T \end{bmatrix} \tag{3.81}$$

$$u = \Delta T_\mathrm{req}, \tag{3.82}$$

the model equations can then be stated as

$$\dot{\boldsymbol{x}} = \underbrace{\begin{bmatrix} A_{11} & A_{12} & A_{13} & 0 & A_{15} \\ A_{21} & A_{22} & A_{23} & 0 & A_{25} \\ 0 & 0 & 0 & 1 & 0 \\ A_{41} & A_{42} & A_{43} & A_{44} & A_{45} \\ 0 & 0 & 0 & 0 & A_{55} \end{bmatrix}}_{\boldsymbol{A}(v)} \boldsymbol{x} + \underbrace{\begin{bmatrix} 0 \\ 0 \\ 0 \\ 0 \\ B_5 \end{bmatrix}}_{\boldsymbol{b}} u, \tag{3.83}$$

and the steering rack position as output equation of form

$$y = \underbrace{\begin{bmatrix} 0 & 0 & 1 & 0 & 0 \end{bmatrix}}_{\boldsymbol{c}^\mathrm{T}} \boldsymbol{x}. \tag{3.84}$$

The model is now in the well known state space form

$$\dot{\boldsymbol{x}} = \boldsymbol{A}(v)\,\boldsymbol{x} + \boldsymbol{b}\,u \tag{3.85}$$

$$y = \boldsymbol{c}^\mathrm{T}\,\boldsymbol{x} \tag{3.86}$$

with a vehicle speed dependent dynamic matrix $\boldsymbol{A}(v)$, a input vector $\boldsymbol{b}$ and a output vector $\boldsymbol{c}^\mathrm{T}$. With 1 input and 1 output, the system is a so called *single-input-single-output* system (SISO).

3.3.2 Derivation of the transfer function

With a system in state space notation, the transfer function can be derived easily via

$$P(s) = \boldsymbol{c}^\mathrm{T}\,(s\,\boldsymbol{I} - \boldsymbol{A})^{-1}\,\boldsymbol{b}. \tag{3.87}$$

$\boldsymbol{I}$ is the identity matrix of the same size as $\boldsymbol{A}$. For later use on the embedded hardware of the BMW X5, this calculation is unsuitable due to the lack of special toolboxes. Therefore, an alternative derivation has to be found instead. In general, the transfer function has the form

$$P(s) = \frac{\mu(s)}{\nu(s)} = \frac{s^4\,\mu_4 + s^3\,\mu_3 + s^2\,\mu_2 + s\,\mu_1 + \mu_0}{s^5 + s^4\,\nu_4 + s^3\,\nu_3 + s^2\,\nu_2 + s\,\nu_1 + \nu_0}, \tag{3.88}$$

where μ_i depict the coefficients of the nominator and ν_i the coefficients of the denominator. Since the model has no feed forward action, the degree of the nominator polynomial is less than the one from the denominator. To get those coefficients of the transfer function, also a transformation according to [17] can be applied. For the calculation of the so called

"controllability normal form", the controllability matrix

$$\boldsymbol{S}_{\mathrm{u}} = \begin{bmatrix} \boldsymbol{b} & \boldsymbol{b}\,\boldsymbol{A} & \boldsymbol{b}\,\boldsymbol{A}^2 & \boldsymbol{b}\,\boldsymbol{A}^3 & \boldsymbol{b}\,\boldsymbol{A}^4 \end{bmatrix} \tag{3.89}$$

is necessary. By calculating

$$\boldsymbol{t}_1 = \begin{bmatrix} 0 & 0 & 0 & 0 & 1 \end{bmatrix} \boldsymbol{S}_{\mathrm{u}}^{-1}, \tag{3.90}$$

a transformation matrix

$$\boldsymbol{T} = \begin{bmatrix} \boldsymbol{t}_1 \\ \boldsymbol{t}_1\,\boldsymbol{A} \\ \boldsymbol{t}_1\,\boldsymbol{A}^2 \\ \boldsymbol{t}_1\,\boldsymbol{A}^3 \\ \boldsymbol{t}_1\,\boldsymbol{A}^4 \end{bmatrix} \tag{3.91}$$

can be derived. Using this matrix, a state transformation

$$\boldsymbol{z} = \boldsymbol{T}\,\boldsymbol{x} \tag{3.92}$$

can be applied to the original system. This operation rearranges the state space notation to

$$\dot{\boldsymbol{z}} = \underbrace{\boldsymbol{T}\,\boldsymbol{A}\,\boldsymbol{T}^{-1}}_{\boldsymbol{A}_{\mathrm{tf}}}\,\boldsymbol{z} + \underbrace{\boldsymbol{T}\,\boldsymbol{b}}_{\boldsymbol{b}_{\mathrm{tf}}}\,u \tag{3.93}$$

$$y = \underbrace{\boldsymbol{c}^{\mathrm{T}}\,\boldsymbol{T}^{-1}}_{\boldsymbol{c}_{\mathrm{tf}}^{\mathrm{T}}}\,\boldsymbol{z}. \tag{3.94}$$

Then the matrix $\boldsymbol{A}_{\mathrm{tf}}$ and the vectors $\boldsymbol{b}_{\mathrm{tf}}$, $\boldsymbol{c}_{\mathrm{tf}}^{\mathrm{T}}$ are in the special form of

$$\boldsymbol{A}_{\mathrm{tf}} = \begin{bmatrix} 0 & 1 & 0 & 0 & 0 \\ 0 & 0 & 1 & 0 & 0 \\ 0 & 0 & 0 & 1 & 0 \\ 0 & 0 & 0 & 0 & 1 \\ -\nu_0 & -\nu_1 & -\nu_2 & -\nu_3 & -\nu_4 \end{bmatrix} \tag{3.95}$$

$$\boldsymbol{b}_{\mathrm{tf}} = \begin{bmatrix} 0 & 0 & 0 & 0 & 1 \end{bmatrix}^{\mathrm{T}} \tag{3.96}$$

$$\boldsymbol{c}_{\mathrm{tf}}^{\mathrm{T}} = \begin{bmatrix} \mu_0 & \mu_1 & \mu_2 & \mu_3 & \mu_4 \end{bmatrix}, \tag{3.97}$$

where the coefficients of $P(s)$ are available as single entries.

3.3.3 Stability Analysis

With the transfer function $P(s)$, stability of the system can be determined by analyzing the zeros and poles. Furthermore, the characteristics in frequency domain can be investigated with the help of bode-diagrams. Figure 3.13 shows the poles and zeros, Figure 3.14 shows bode diagrams for different vehicle speeds.

The result is a system, which is stable for vehicle speeds up to $v < 200\,\mathrm{km/h}$. Moreover, the system has a minimum phase behavior up to $v < 100\,\mathrm{km/h}$. However, this stability analysis is true for the simplified linear model, but has no validity for the real car.

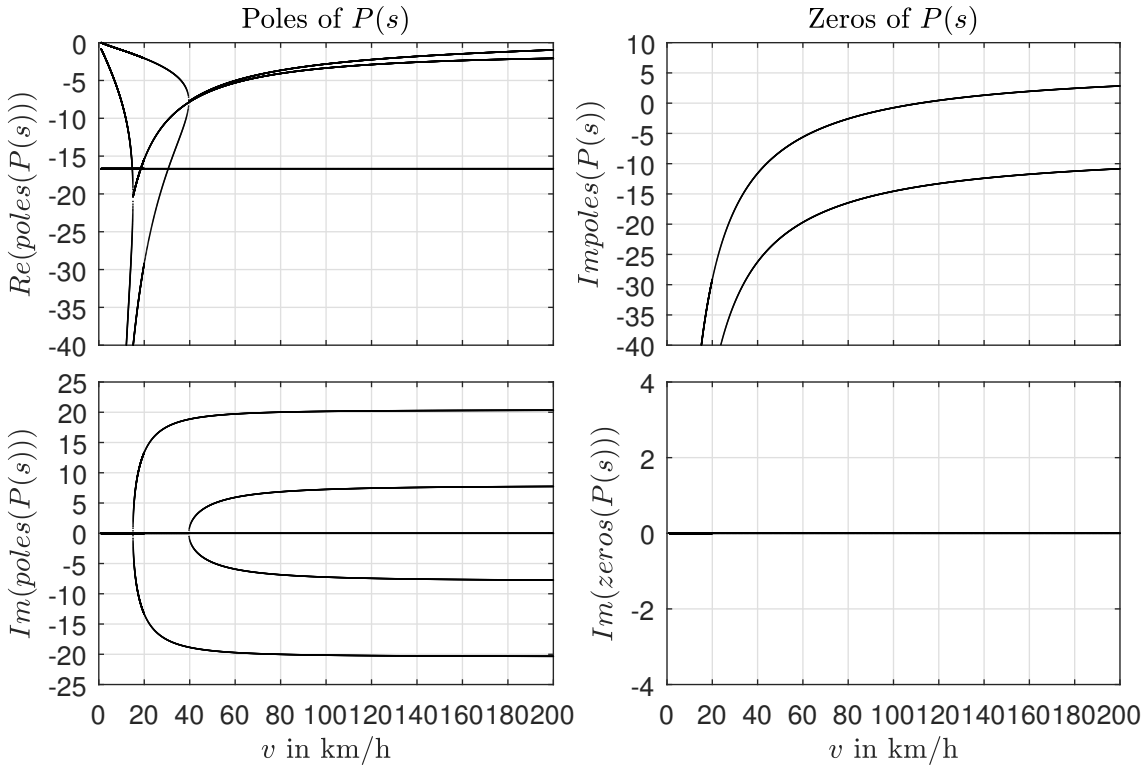

Figure 3.13: Poles and Zeros of $P(s)$ for different vehicle speeds. The diagrams are separated in real and imaginary parts of the poles and zeros. Since the system has 5th order, also 5 poles are existent. One can see that the real part of the poles are negative for the whole range of v which is representing for a stable system. At approx. 100 km/h, one of the two zeros gets positive, which means that system gets a non-minimum phase behavior for higher speeds.

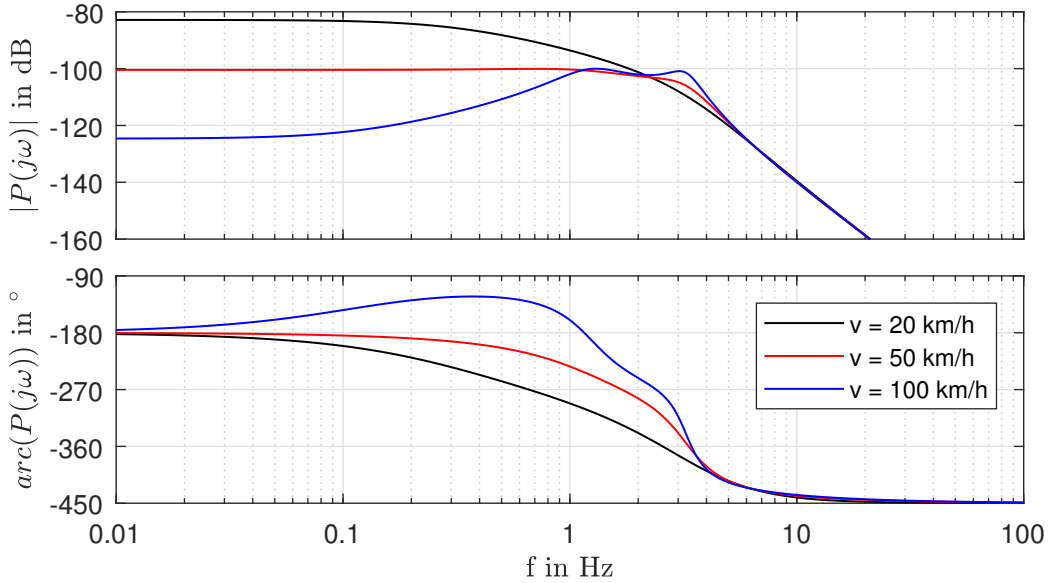

Figure 3.14: Bode diagram of $P(s)$ for different vehicle speeds. For higher velocities, resonance effects are visible. The first resonance at around 1 Hz comes from the chassis, the second resonance at around 3.2 Hz comes from the steering rack. The phase drop is $-270°$, because of the difference in numbers of poles and zeros in $P(s)$.

3.4 Analysis of the linear model

As a completion of the modeling part of this theses, the derived and validated model of the previous sections was compared against the VTC model and real measurement data for different maneuvers.

3.4.1 Comparison against simulation data

To investigate the steady state behavior, a constant differential torque was applied to both the VTC model and the derived linear model. With an ascending vehicle speed in form of a ramp signal, the influence of the velocity was included. Figure 3.15 shows this maneuver for $\Delta T = 500\,\mathrm{Nm}$ with a velocity range of $20\,\mathrm{km/h} < v < 100\,\mathrm{km/h}$. For a better benchmark result, the static friction on the steering rack from equation (3.78) was included.

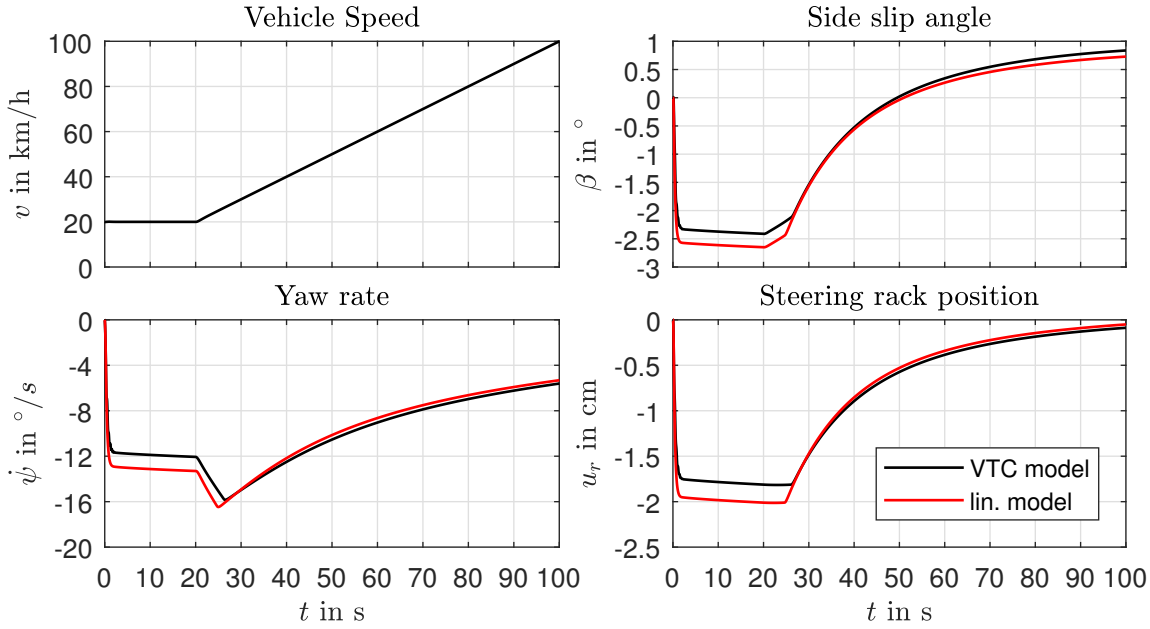

Figure 3.15: A constant differential torque step input of $\Delta T = 500\,\mathrm{Nm}$ for ascending vehicle speed starting at $v = 20\,\mathrm{kmh}$. For low speeds, there are errors in the steering rack position and in further consequences also in the yaw rate and the side slip angle. These errors come from the linearisation of the steering rack model and are unavoidable. As mentioned in section 3.2.2, this linearisation was optimized with a minimization of these errors. At around 30 km/h, the error is significantly low and matches the simulation accurately.

In Figure 3.16, the same experiment was done with a higher differential torque of $\Delta T = 1000\,\mathrm{Nm}$. At this value the linear model matches the results from the VTC model very good, and the errors described in Figure 3.15 are much smaller.

To compare the models in frequency domain, differential torque in form of a sine sweep was injected at a constant vehicle speed. Figure 3.17 shows the results.

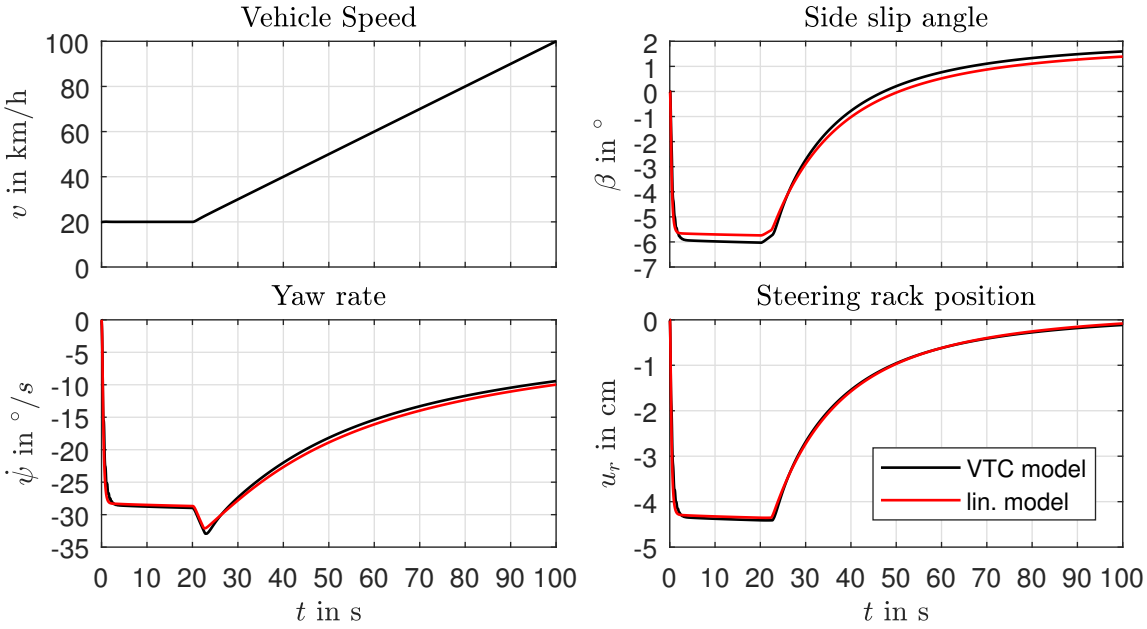

Figure 3.16: A constant differential torque step input of $\Delta T = 1000\,\text{Nm}$ for ascending vehicle speed starting at $v = 20\,\text{kmh}$. The errors of the steering rack position are very low and the behavior matches the VTC model accurately. Errors in the side slip angle come from linearisation errors of the trigonometric functions.

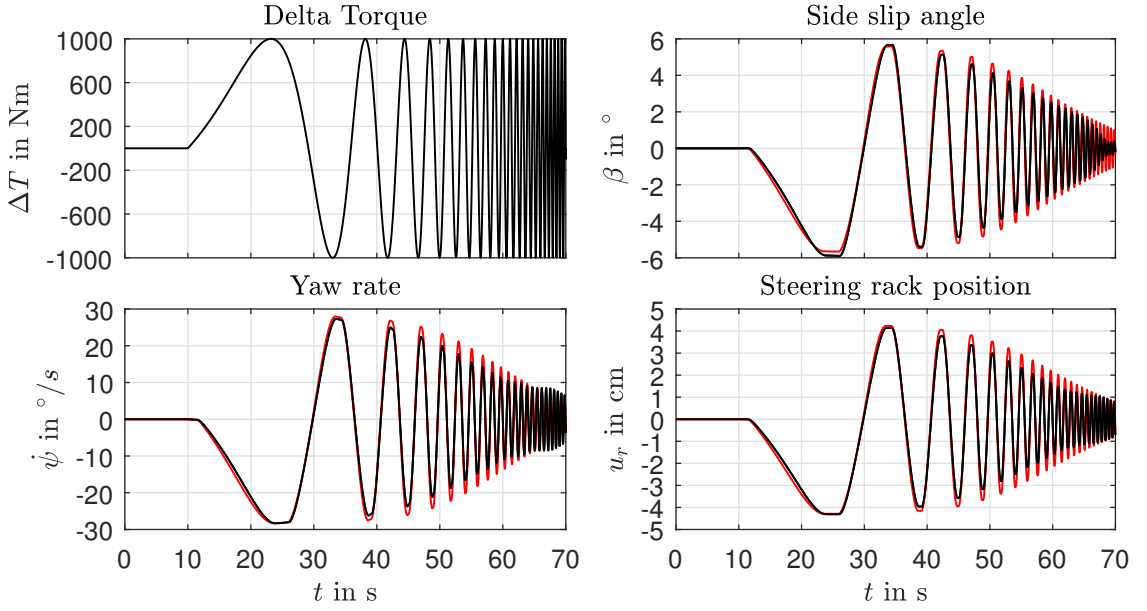

Figure 3.17: Sine sweep with an amplitude of 1000 Nm for a constant vehicle speed of $v = 20\,\text{km/h}$ with a frequency range of $0.01\,\text{Hz} < f < 3\,\text{Hz}$. The black lines depict the results from the VTC model, the red lines the results from the linear model. For small frequencies, the comparison against the VTC model is very good. For higher frequencies, errors occur in the amplitudes but the signals are in phase. At very high frequencies, the resonance characteristic is more dominant in the VTC model.

3.4.2 Comparison against measurement data

In Figure 3.18 and Figure 3.19, two typical experiments (double lane change and slalom) were measured with the real car and compared to the linear model. The static friction of the rack was considered like in the comparisons against the VTC model.

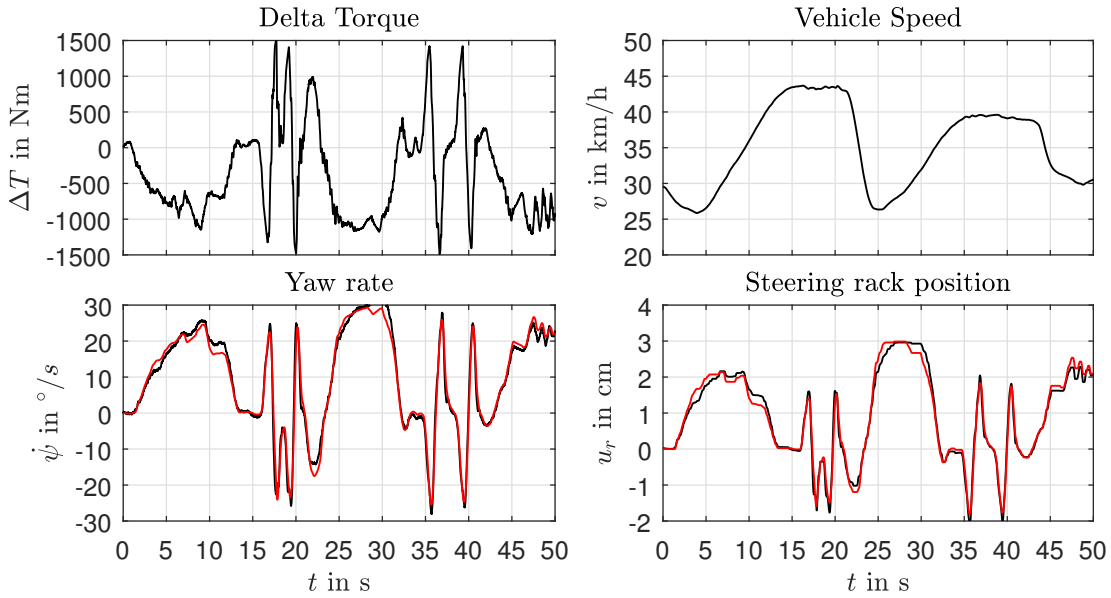

Figure 3.18: Comparison to measurement data of the BMW X5. The black lines depict the measurement data, and the red lines the simulation data. The linear model describes the behavior of the car quite well, especially in the more dynamic maneuvers like the double lane change starting at $t = 15\,\mathrm{s}$, the errors are very small. At less dynamic driving, errors occur due to complex friction in the rack and linearisation problems.

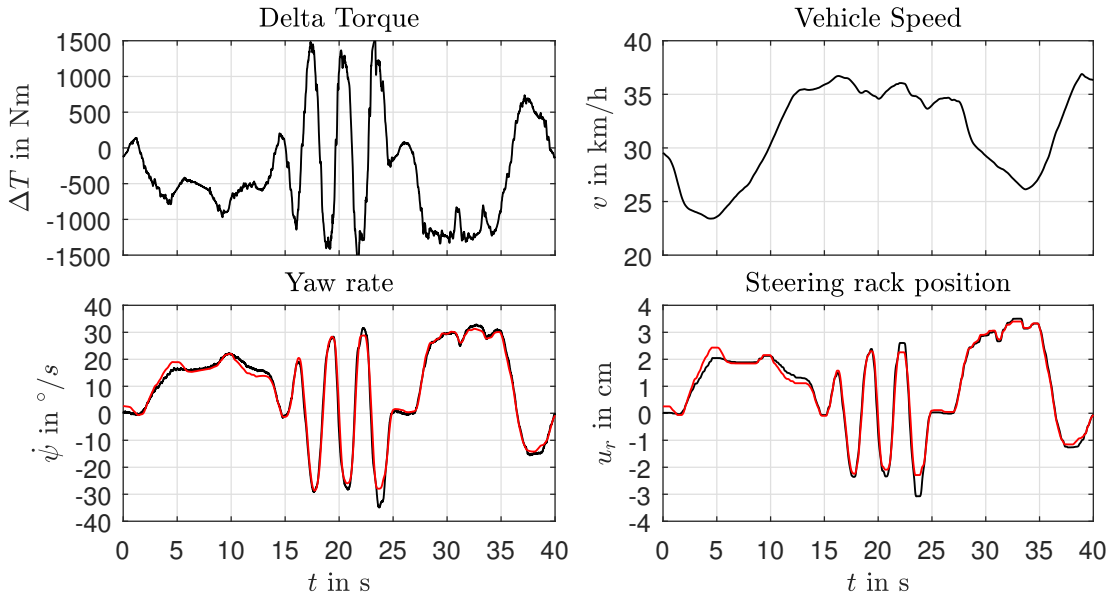

Figure 3.19: Slalom maneuver with $v = 35\,\mathrm{km/h}$. Like in Figure 3.18, some errors at less dynamic driving situations but also at the slalom maneuver. This comes from the gain of the longitudinal tire forces to rack force, which normally increases with increasing rack position, but is linearized here to the value at $u_\mathrm{r} = 0$.

4 Controller Theory

To control SbTV, there are two possible control targets. On the one hand the control of the steering rack position u_r and on the other hand the control of the yaw rate $\dot{\psi}$. Both of the targets have their advantages and drawbacks.

A movement of the steering rack is a direct reaction to a delta torque ΔT on the wheels, which principally enables a good performance. Also, all the sensors of the SbW system are available, which have very high precision and low noise. Furthermore, especially for slow vehicle speeds, the control of the rack position works a lot better than the control of the yaw rate. Whereas a yaw rate target definitely has its advantages in motion control and autonomous driving. It makes trajectory planning much easier than with a target of u_r. Also, the transition between SbW and SbTV needs no additional target recalculation, since the yaw rate represents the actual movement of the car. The sensor for the yaw rate is a gyroscopic acceleration sensor, which bring uncertainties at low values and also consists of a lot of noise, as the signal is the result from the integrated yaw-acceleration.

For this thesis, the target of choice is the rack position u_r. Because of a direct reaction to the drive torques, the rack is easier to control. More on, the target generation is very easy, since it is proportional to the steering wheel angle. Two different controller principles have been implemented and tested.

4.1 State-feedback controller with integral action and anti windup strategy

One possible controller concept to control the rack position, is the use of a state-feedback controller. But since the derived model in Chapter 3 is not accurate in a stationary situation, the controller also needs integral action to guarantee offset-free tracking of the reference. A very problematic side effect of integral action are windup effects. In terms of safety and stability these effects can get dangerous and needs to be avoided by proper anti-windup techniques. Hippe and Wurmthaler introduced a variation for the conventional state-feedback controller, that suits for this kind of problem very well [18].

The base for this controller concept is a plant model in state space notation

$$\begin{aligned} \dot{\boldsymbol{x}} &= \boldsymbol{A}\,\boldsymbol{x} + \boldsymbol{b}\,u \\ y &= \boldsymbol{c}^\mathrm{T}\,\boldsymbol{x} \end{aligned} \tag{4.1}$$

where the state vector $\boldsymbol{x}$ is not (or not fully) measurable. With a standard Luenberger observer [17], this state vector can be estimated by a dynamic model of form

$$\dot{\hat{\boldsymbol{x}}} = \left(\boldsymbol{A} - \hat{\boldsymbol{b}}\,\boldsymbol{c}^\mathrm{T}\right)\hat{\boldsymbol{x}} + \boldsymbol{b}\,u + \hat{\boldsymbol{b}}\,y. \tag{4.2}$$

This state estimate is multiplied with the state-feedback-gain $\boldsymbol{k}^\mathrm{T}$ and fed back to the input of the system. Figure 4.1 shows the principal structure of a so called control-observer structure.

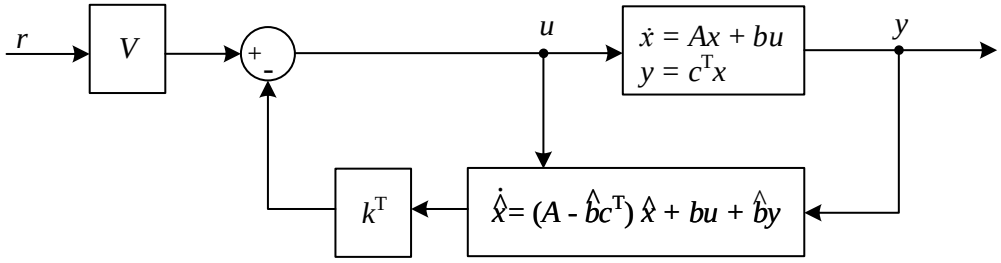

Figure 4.1: Standard control observer according to [17]. The state estimate $\hat{\boldsymbol{x}}$ is fed back to the input via the feedback gain $\boldsymbol{k}^{\mathrm{T}}$. In case of a accurate model, the gain V ensures offset-free tracking of the reference r.

By introducing the estimation error

$$\boldsymbol{e} = \boldsymbol{x} - \hat{\boldsymbol{x}}, \tag{4.3}$$

the whole system can be transformed in a state space model

$$\begin{bmatrix} \dot{\boldsymbol{x}} \\ \dot{\boldsymbol{e}} \end{bmatrix} = \begin{bmatrix} \left(\boldsymbol{A} - \boldsymbol{b}\,\boldsymbol{k}^{\mathrm{T}}\right) & \boldsymbol{b}\,\boldsymbol{k}^{\mathrm{T}} \\ \mathbf{0} & \left(\boldsymbol{A} - \hat{\boldsymbol{b}}\,\boldsymbol{c}^{\mathrm{T}}\right) \end{bmatrix} \begin{bmatrix} \boldsymbol{x} \\ \boldsymbol{e} \end{bmatrix} + \begin{bmatrix} \boldsymbol{b} \\ \mathbf{0} \end{bmatrix} V\, r \tag{4.4}$$

$$y = \begin{bmatrix} \boldsymbol{c}^{\mathrm{T}} & \mathbf{0}^{\mathrm{T}} \end{bmatrix} \begin{bmatrix} \boldsymbol{x} \\ \boldsymbol{e} \end{bmatrix}. \tag{4.5}$$

The dynamics of this system is determined by the characteristic polynomial of the dynamic matrix by

$$\begin{aligned} \tilde{\Delta}(s) &= \det \begin{bmatrix} s\mathbf{I} - \left(\boldsymbol{A} - \boldsymbol{b}\,\boldsymbol{k}^{\mathrm{T}}\right) & -\boldsymbol{b}\,\boldsymbol{k}^{\mathrm{T}} \\ \mathbf{0} & s\mathbf{I} - \left(\boldsymbol{A} - \hat{\boldsymbol{b}}\,\boldsymbol{c}^{\mathrm{T}}\right) \end{bmatrix} \\ &= \underbrace{\det[s\mathbf{I} - (\boldsymbol{A} - \boldsymbol{b}\,\boldsymbol{k}^{\mathrm{T}})]}_{\Delta(s)}\, \underbrace{\det[s\mathbf{I} - (\boldsymbol{A} - \hat{\boldsymbol{b}}\,\boldsymbol{c}^{\mathrm{T}})]}_{\hat{\Delta}(s)} \end{aligned} \tag{4.6}$$

which can be separated into a controller polynomial $\Delta(s)$ and observer polynomial $\hat{\Delta}(s)$. Theses polynomials are dependent on the feedback-gain $\boldsymbol{k}^{\mathrm{T}}$ and observer gain $\hat{\boldsymbol{b}}$ and represent the tuning parameters of the control observer.

With transfer functions, the input-output behavior of this controller structure can also be described in frequency domain via

$$P(s) = \left.\frac{y(s)}{u(s)}\right|_{\boldsymbol{x}_0=0} = \boldsymbol{c}^{\mathrm{T}}\,(s\,\mathbf{I} - \boldsymbol{A})^{-1}\,\boldsymbol{b} = \frac{\mu(s)}{\nu(s)} \tag{4.7}$$

$$G_{\mathrm{u}}(s) = \left.\frac{v_1(s)}{u(s)}\right|_{\hat{\boldsymbol{x}}_0=0} = \boldsymbol{k}^{\mathrm{T}}\left(s\,\mathbf{I} - \left(\boldsymbol{A} - \hat{\boldsymbol{b}}\,\boldsymbol{c}^{\mathrm{T}}\right)\right)^{-1}\boldsymbol{b} = \frac{\mu_{\mathrm{u}}(s)}{\hat{\Delta}(s)} \tag{4.8}$$

$$G_{\mathrm{y}}(s) = \left.\frac{v_2(s)}{y(s)}\right|_{\hat{\boldsymbol{x}}_0=0} = \boldsymbol{k}^{\mathrm{T}}\left(s\,\mathbf{I} - \left(\boldsymbol{A} - \hat{\boldsymbol{b}}\,\boldsymbol{c}^{\mathrm{T}}\right)\right)^{-1}\hat{\boldsymbol{b}} = \frac{\mu_{\mathrm{y}}(s)}{\hat{\Delta}(s)} \tag{4.9}$$

by a structure depicted in Figure 4.2. The denominator of the observer transfer functions $G_{\mathrm{u}}(s)$ and $G_{\mathrm{y}}(s)$ are determined by the observer polynomial $\hat{\Delta}(s)$.

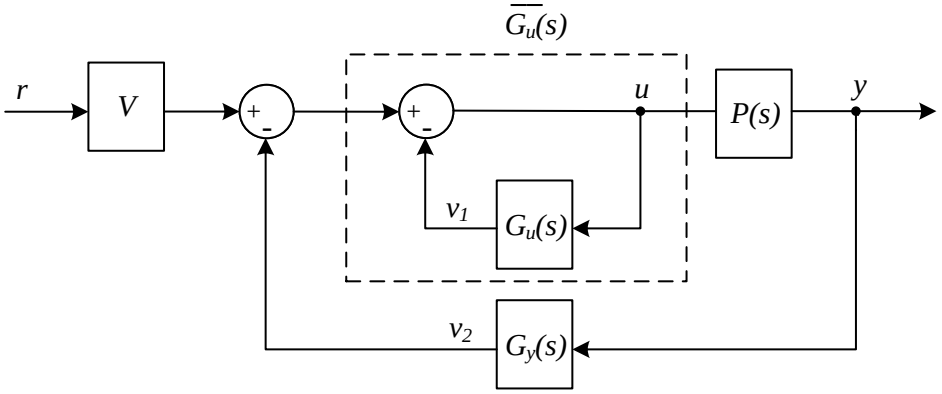

Figure 4.2: Input-output behavior of the control observer in frequency domain. The observer with state-feedback gain can be represented by 2 transfer functions $G_\mathrm{u}(s)$ and $G_\mathrm{y}(s)$.

With

$$\overline{G_\mathrm{u}}(s) = \frac{1}{1 + G_\mathrm{u}(s)} = \frac{\hat{\Delta}(s)}{\hat{\Delta}(s) + \mu_\mathrm{u}(s)} = \frac{\hat{\Delta}(s)}{\nu_\mathrm{u}(s)}, \tag{4.10}$$

the structure of the system can be transformed to a standard 2-degree-of-freedom controller as depicted in Figure 4.3.

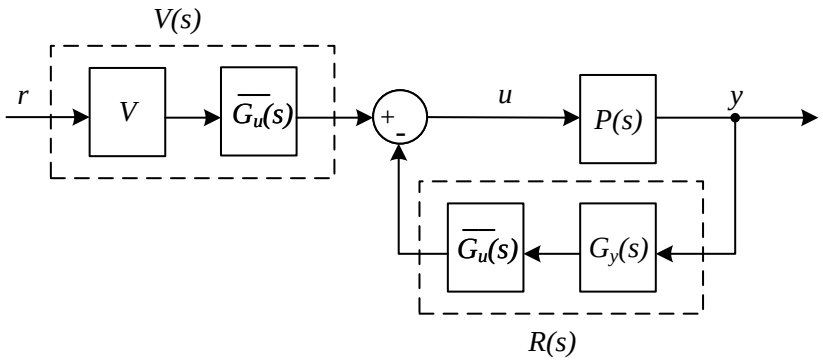

Figure 4.3: The control observer transformed to a standard 2DoF controller structure. By extracting $\overline{G_\mathrm{u}}(s)$ to the outer loop, the closed loop system consists of 2 controller transfer functions, $R(s)$ and $V(s)$.

The resulting controller transfer functions are then given by

$$V(s) = V\,\overline{G_\mathrm{u}}(s) = V\,\frac{\hat{\Delta}(s)}{\nu_\mathrm{u}(s)} \tag{4.11}$$

$$R(s) = \overline{G_\mathrm{u}}(s)\,G_\mathrm{y}(s) = \frac{\hat{\Delta}(s)\,\mu_\mathrm{y}(s)}{\nu_\mathrm{u}(s)\,\hat{\Delta}(s)} = \frac{\mu_\mathrm{y}(s)}{\nu_\mathrm{u}(s)} \tag{4.12}$$

Now, the closed loop transfer function of the whole system can be derived by

$$T(s) = \frac{V(s)\,P(s)}{1 + R(s)\,P(s)} = V\,\frac{\mu(s)\,\hat{\Delta}(s)}{\nu_\mathrm{u}(s)\,\nu(s) + \mu_\mathrm{y}(s)\,\mu(s)}. \tag{4.13}$$

According to [17], the transfer function of the control observer can also be calculated by

$$T(s) = \left.\frac{y(s)}{r(s)}\right|_{\boldsymbol{x}_0,\hat{\boldsymbol{x}}_0=0} = \boldsymbol{c}^{\mathrm{T}}\left(s\,\mathbf{I} - \left(\boldsymbol{A} - \boldsymbol{b}\,\boldsymbol{k}^{\mathrm{T}}\right)\right)^{-1}\boldsymbol{b}\,V = V\frac{\mu(s)}{\Delta(s)}. \tag{4.14}$$

Because of the vanishing initial state values, the observer error is zero, which means that the observer has no influence on the closed loop transfer function. By combining equation (4.13) and (4.14),

$$T(s) = V\,\frac{\mu(s)\,\hat{\Delta}(s)}{\nu_{\mathrm{u}}(s)\,\nu(s) + \mu_{\mathrm{y}}(s)\,\mu(s)} \stackrel{!}{=} V\frac{\mu(s)}{\Delta(s)} = V\frac{\mu(s)\,\hat{\Delta}(s)}{\Delta(s)\,\hat{\Delta}(s)} \tag{4.15}$$

the following fundamental equation results as

$$\nu_{\mathrm{u}}(s)\,\nu(s) + \mu_{\mathrm{y}}(s)\,\mu(s) = \Delta(s)\,\hat{\Delta}(s). \tag{4.16}$$

This relation is called *diophantic equation* and is the foundation for the controller design of this section.

The idea of Hippe and Wurmthaler [18] was to design the controller with the diophantic equation, include integral action and transform the result back to the structure shown in Figure 4.2. In this structure, the consideration of the anti-windup will be very easy. To allow a systematic design, the algebraic controller synthesis described in [17] was used.

4.1.1 Systematic Design

The individual polynomials from equation (4.16) can be specified as

$$\nu_{\mathrm{u}}(s) = a_n\,s^n + a_{n-1}\,s^{n-1} + \cdots + a_2\,s^2 + a_1\,s^1 + a_0 \tag{4.17}$$
$$\nu(s) = \nu_n\,s^n + \nu_{n-1}\,s^{n-1} + \cdots + \nu_2\,s^2 + \nu_1\,s^1 + \nu_0 \tag{4.18}$$
$$\mu_{\mathrm{y}}(s) = b_n\,s^n + b_{n-1}\,s^{n-1} + \cdots + b_2\,s^2 + b_1\,s^1 + b_0 \tag{4.19}$$
$$\mu(s) = \mu_{n-1}\,s^{n-1} + \cdots + \mu_2\,s^2 + \mu_1\,s^1 + \mu_0 \tag{4.20}$$
$$\Delta(s) = c_n\,s^n + c_{n-1}\,s^{n-1} + \cdots + c_2\,s^2 + c_1\,s^1 + c_0 \tag{4.21}$$
$$\hat{\Delta}(s) = d_n\,s^n + d_{n-1}\,s^{n-1} + \cdots + d_2\,s^2 + d_1\,s^1 + d_0 \tag{4.22}$$

with n as the order of the system $P(s)$ (which is the same as the rank of the dynamic matrix A). Now the polynomials can be inserted in the left side of the diophantic equation, which results in

$$\begin{aligned}
\nu_{\mathrm{u}}(s)\,\nu(s) + \mu_{\mathrm{y}}(s)\,\mu(s) = {} & \nu_0\,a_0 + \mu_0\,b_0 \\
& + s\left[(\nu_0\,a_1 + \nu_1\,a_0) + (\mu_0\,b_1 + \mu_1\,b_0)\right] \\
& + s^2\left[(\nu_0\,a_2 + \nu_1\,a_1 + \nu_2\,a_0) + (\mu_0\,b_2 + \mu_1\,b_1 + \mu_2\,b_0)\right] \\
& \vdots \\
& + s^{2n-1}\left[(\nu_{n-1}\,a_n + \nu_n\,a_{n-1}) + (\mu_{n-1}\,b_n)\right] \\
& + s^{2n}\left[\nu_n\,a_n\right].
\end{aligned} \tag{4.23}$$

This can also be done on the right side of the equation as

$$\begin{aligned}\Delta(s)\,\hat{\Delta}(s) = {} & c_0\,d_0 \\ & + s\,[c_0\,d_1 + c_1\,d_0] \\ & + s^2\,[c_0\,d_2 + c_1\,d_1 + c_2\,d_0] \\ & \vdots \\ & + s^{2n-1}\,[c_{n-1}\,d_n + c_n\,d_{n-1}] \\ & + s^{2n}\,[c_n\,d_n]\,.\end{aligned} \tag{4.24}$$

Comparing the coefficients of (4.23) and (4.24), $2n+1$ equations

$$\nu_0\,a_0 + \mu_0\,b_0 = c_0\,d_0 \tag{4.25}$$
$$(\nu_0\,a_1 + \nu_1\,a_0) + (\mu_0\,b_1 + \mu_1\,b_0) = c_0\,d_1 + c_1\,d_0 \tag{4.26}$$
$$(\nu_0\,a_2 + \nu_1\,a_1 + \nu_2\,a_0) + (\mu_0\,b_2 + \mu_1\,b_1 + \mu_2\,b_0) = c_0\,d_2 + c_1\,d_1 + c_2\,d_0 \tag{4.27}$$
$$\vdots \tag{4.28}$$
$$(\nu_{n-1}\,a_n + \nu_n\,a_{n-1}) + (\mu_{n-1}\,b_n) = c_{n-1}\,d_n + c_n\,d_{n-1} \tag{4.29}$$
$$\nu_n\,a_n = c_n\,d_n \tag{4.30}$$

can be stated for $2n+2$ unknown variables of $\nu_{\mathrm{u}}(s)$ and $\mu_{\mathrm{y}}(s)$. This means, that another equation is necessary to allow the set of equations a unique solution. This degree of freedom is used to give the controller integral action.

A controller with integral behavior is characterized by a pole at $s = 0$. This pole can be enforced by

$$a_0 = 0 \tag{4.31}$$

as an additional condition in the above described set of equations. Now the set is fully determined and can be stated in a matrix equation of form

$$\boldsymbol{K}\,\boldsymbol{p} = \boldsymbol{f} \tag{4.32}$$

where the Matrix $\boldsymbol{K}$ is the so called *resultant* and consists of the parameters of $\nu(s)$ and $\mu(s)$. $\boldsymbol{p}$ is a vector with the parameters of $\nu_{\mathrm{u}}(s)$ and $\mu_{\mathrm{y}}(s)$, which depict the unknown quantities in the equation. And $\boldsymbol{f}$ describes the right hand side from equation (4.25) to (4.31). They are given by

$$\boldsymbol{f} = \begin{bmatrix} c_0\,d_0 \\ c_0\,d_1 + c_1\,d_0 \\ c_0\,d_2 + c_1\,d_1 + c_2\,d_0 \\ \vdots \\ c_{n-1}\,d_n + c_n\,d_{n-1} \\ c_n\,d_n \\ 0 \end{bmatrix} \tag{4.33}$$

$$\boldsymbol{p} = \begin{bmatrix} a_0 & a_1 & \dots & a_n & b_0 & b_1 & \dots & b_n \end{bmatrix}^{\mathrm{T}} \tag{4.34}$$

$$\boldsymbol{K} = \begin{bmatrix} \nu_0 & 0 & 0 & \dots & 0 & 0 & \mu_0 & 0 & \dots & 0 & 0 & 0 \\ \nu_1 & \nu_0 & 0 & \dots & 0 & 0 & \mu_1 & \mu_0 & & \vdots & 0 & 0 \\ \nu_2 & \nu_1 & \nu_0 & & \vdots & 0 & \vdots & \mu_1 & \ddots & 0 & \vdots & 0 \\ \vdots & \nu_2 & \nu_1 & \ddots & 0 & \vdots & \mu_{n-1} & \vdots & \ddots & \mu_0 & 0 & \vdots \\ \nu_n & \vdots & \nu_2 & \ddots & \nu_0 & 0 & 0 & \mu_{n-1} & & \mu_1 & \mu_0 & 0 \\ 0 & \nu_n & \vdots & \ddots & \nu_1 & \nu_0 & 0 & 0 & \ddots & \vdots & \mu_1 & \mu_0 \\ 0 & 0 & \nu_n & & \nu_2 & \nu_1 & 0 & 0 & & \mu_{n-1} & \vdots & \mu_1 \\ 0 & 0 & 0 & \ddots & \vdots & \nu_2 & 0 & 0 & \dots & 0 & \mu_{n-1} & \vdots \\ \vdots & \vdots & \vdots & & \nu_n & \vdots & \vdots & \vdots & \dots & 0 & 0 & \mu_{n-1} \\ 0 & 0 & 0 & \dots & 0 & \nu_n & 0 & 0 & \dots & 0 & 0 & 0 \\ 1 & 0 & 0 & \dots & 0 & 0 & 0 & 0 & \dots & 0 & 0 & 0 \end{bmatrix} \tag{4.35}$$

The unknown quantities $\boldsymbol{p}$ can then be calculated by

$$\boldsymbol{p} = \boldsymbol{K}^{-1}\, \boldsymbol{f}. \tag{4.36}$$

To avoid singularities in the Matrix $\boldsymbol{K}$ it is very important that $P(s)$ does not have poles and zeros at the same position. If this happens, they have to be shortened beforehand, otherwise there will be problems calculating the inverse $\boldsymbol{K}^{-1}$. Now, $R(s)$ of structure from Figure 4.3 is fully determined.

To allow offset-free tracking the condition

$$T(s)|_{s=0} = V \frac{\mu(s)}{\Delta(s)}\bigg|_{s=0} \stackrel{!}{=} 1 \tag{4.37}$$

has to hold. Therefore, the gain factor V is defined as

$$V = \frac{\Delta(s)}{\mu(s)}\bigg|_{s=0} = \frac{c_0}{\mu_0}. \tag{4.38}$$

As a next step, the structure of Figure 4.3 is transformed back to the one of Figure 4.2 by

$$G_{\mathrm{u}}(s) = \frac{\nu_{\mathrm{u}}(s) - \hat{\Delta}(s)}{\hat{\Delta}(s)} \tag{4.39}$$

$$G_{\mathrm{y}}(s) = \frac{\mu_{\mathrm{y}}(s)}{\hat{\Delta}(s)}. \tag{4.40}$$

Since $\Delta(s)$ and $\hat{\Delta}(s)$ are monic polynomials (which means that $c_n = 1$ and $d_n = 1$), also $\nu_{\mathrm{u}}(s)$ is monic. Therefore, the structure of these transfer function are given by

$$G_{\mathrm{u}}(s) = \frac{\tilde{a}_{n-1}\, s^{n-1} + \dots + \tilde{a}_2\, s^2 + \tilde{a}_1\, s^1 + \tilde{a}_0}{s^n + d_{n-1}\, s^{n-1} + \dots + d_2\, s^2 + d_1\, s^1 + d_0} \tag{4.41}$$

$$G_{\mathrm{y}}(s) = \frac{b_n\, s^n + b_{n-1}\, s^{n-1} + \dots + b_2\, s^2 + b_1\, s^1 + b_0}{s^n + d_{n-1}\, s^{n-1} + \dots + d_2\, s^2 + d_1\, s^1 + d_0}. \tag{4.42}$$

with a common denominator $\hat{\Delta}(s)$. Since they share the same dynamics, the controller can be realized in one dynamic system in form of a state-space realization. First, $G_{\mathrm{y}}(s)$ has to be split up in a feed trough and a strictly proper part. By partial fraction decomposition, this can be done by

$$G_{\mathrm{y}}(s) = b_n + \frac{\tilde{b}_{n-1}\, s^{n-1} + \cdots + \tilde{b}_2\, s^2 + \tilde{b}_1\, s^1 + \tilde{b}_0}{s^n + d_{n-1}\, s^{n-1} + \cdots + d_2\, s^2 + d_1\, s^1 + d_0} \tag{4.43}$$

and

$$\tilde{\boldsymbol{b}} = \begin{bmatrix} \tilde{b}_{n-1} \\ \vdots \\ \tilde{b}_2 \\ \tilde{b}_1 \\ \tilde{b}_0 \end{bmatrix} = \begin{bmatrix} b_{n-1} - b_n\, d_{n-1} \\ \vdots \\ b_2 - b_n\, d_2 \\ b_1 - b_n\, d_1 \\ b_0 - b_n\, d_0 \end{bmatrix}. \tag{4.44}$$

The final controller can then be stated in observability normal form [17] via

$$\boldsymbol{z} = \begin{bmatrix} 0 & \dots & 0 & -d_0 \\ 1 & \ddots & \vdots & -d_1 \\ \vdots & \ddots & 0 & \vdots \\ 0 & \dots & 1 & -d_{n-1} \end{bmatrix} \boldsymbol{z} + \begin{bmatrix} -\tilde{a}_0 \\ -\tilde{a}_1 \\ \vdots \\ -\tilde{a}_{n-1} \end{bmatrix} u + \begin{bmatrix} -\tilde{b}_0 \\ -\tilde{b}_1 \\ \vdots \\ -\tilde{b}_{n-1} \end{bmatrix} y \tag{4.45}$$

$$w = \begin{bmatrix} 0 & \dots & 0 & 1 \end{bmatrix} \boldsymbol{z} - b_n\, y + V\, r \tag{4.46}$$

with n controller states $\boldsymbol{z}$, r as the reference, y as the measured target, w as the unsaturated controller output and u as the saturated controller output. Figure 4.4 shows the structure of the control system with the input saturation and explains the Anti-Windup technique of this controller design.

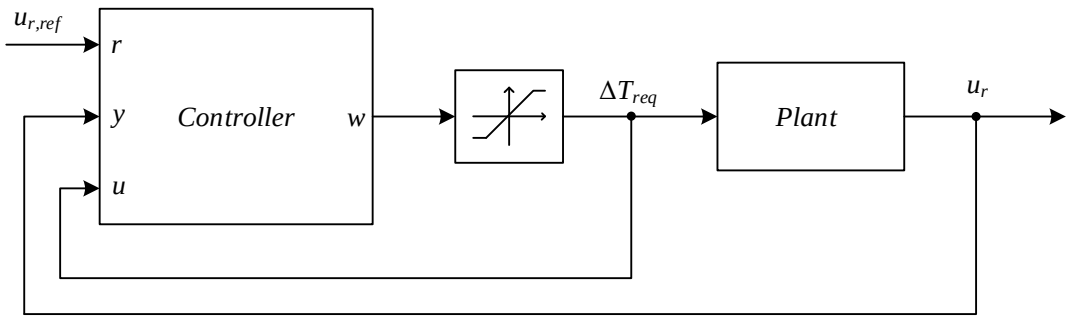

Figure 4.4: Structure of the resulting control system. By saturating the controller output w and feeding back the saturated quantity u to the controller, the special structure of the derived controller limits the output to the boundaries of the saturation automatically. This avoids possible wind-up effects and improves the performance of the controller a lot. The technique works under the principle of input conditioning. In case of a saturated signal, a virtual reference signal is generated to limit the controller output [18].

4.1.2 LQR design for a systematic controller tuning

The tuning parameters for the derived controller concepts are the polynomial coefficients of $\Delta(s)$ and $\hat{\Delta}(s)$, which represent the poles for the closed loop system and observer. For a system of order 5, this means that 10 parameters need to be tuned, which can be a difficult and time consuming process. To simplify this tuning procedure, also the so called LQR (Linear Quadratic Regulator) design method can be used [19].

With LQR, a cost function of form

$$\min \int_0^\infty \left(\boldsymbol{x}^\mathrm{T} \boldsymbol{Q}\, \boldsymbol{x} + 2\, \boldsymbol{x}^\mathrm{T} \boldsymbol{S}\, u + u\, R\, u \right) dt \tag{4.47}$$

with weighting matrices $\boldsymbol{Q}, \boldsymbol{S}$ and weighting factor R is minimized by solving the algebraic Riccatti equation

$$\boldsymbol{0} = \boldsymbol{Q} + \boldsymbol{A}^\mathrm{T} \boldsymbol{P} + \boldsymbol{P}\, \boldsymbol{A} - (\boldsymbol{P}\, \boldsymbol{b} + \boldsymbol{S})\, R^{-1}\, (\boldsymbol{P}\, \boldsymbol{b} + \boldsymbol{S})^\mathrm{T}\,. \tag{4.48}$$

According to the LQR cost function, the optimal control law for state-feedback control then can be calculated by

$$\boldsymbol{k}^\mathrm{T} = R^{-1}\, (\boldsymbol{P}\, \boldsymbol{b} + \boldsymbol{S})^\mathrm{T} \tag{4.49}$$

with $\boldsymbol{P}$ as the solution of the Ricatti equation. The use of LQR theory brings some major advantages compared to the normal strategy by tuning the poles of the system:

- The design provides an analytic solution
- The resulting controller is always stabilizing
- A guaranteed robustness (in the state feedback case).

For this reasons, LQR is widely used in the industry. But the tuning procedure still needs a lot of effort, since the weighting parameters need to be chosen properly. With a special form of LQR, the so called *output weighting LQR*, this effort can be minimized by setting

$$\boldsymbol{Q} = \boldsymbol{c}\, Q_\mathrm{y}\, \boldsymbol{c}^\mathrm{T}. \tag{4.50}$$

Furthermore, it is very common to set

$$\boldsymbol{S} = \boldsymbol{0} \tag{4.51}$$

as it is not intuitive to weigh a combination of the vehicle states and the controller output. Now the tuning process have only two parameters left, Q_y and R. According to Adamy [20], the ratio of Q_y and R is determining the resulting performance of the controller. For a higher Q_y, the speed of the control gets faster to the account of bigger controller outputs. Therefore, the tuning process can be simplified again to only one tuning parameter by choosing

$$Q_\mathrm{y} = k_\mathrm{c} \tag{4.52}$$

$$R = \frac{1}{k_\mathrm{c}}. \tag{4.53}$$

Then, the cost function from equation (4.47) simplifies to

$$\min \int_0^\infty \left(\boldsymbol{x}^\mathrm{T}\, \boldsymbol{c}\, k_\mathrm{c}\, \boldsymbol{c}^\mathrm{T}\, \boldsymbol{x} + \frac{1}{k_\mathrm{c}}\, u^2 \right) dt. \tag{4.54}$$

With the result of the LQR design, the controller polynomial $\Delta(s)$ can then be derived by

$$\Delta(s) = \det[s\mathbf{I} - (\boldsymbol{A} - \boldsymbol{b}\,\boldsymbol{k}^{\mathrm{T}})]. \tag{4.55}$$

The problem of the observer polynomial tuning $\hat{\Delta}(s)$ is very similar to the problem of tuning $\Delta(s)$. The tuning method for the so called *Kalman Filter* uses the same minimization technique by solving an algebraic Riccatti equation [19]. If the problem is reduced again to one tuning parameter, like in equation (4.54), the resulting polynomial

$$\hat{\Delta}(s) = \det[s\mathbf{I} - (\boldsymbol{A} - \hat{\boldsymbol{b}}\,\boldsymbol{c}^{\mathrm{T}})]. \tag{4.56}$$

with $\hat{b}$ as the result from the Kalman filter design is the same as for the LQR design. Therefore, the same approach as for the controller polynomial can be used with a different parameter k_{o} which controls the speed of the error dynamics of the observer. With a higher value of k_{o}, the estimation error converges faster to 0 with the cost of a higher amplification of process- and measurement noise.

To get an idea, how this single parameter influences the tuning parameters, Figure 4.5 shows the trend of $\Delta(s)$ dependent on k_{c}.

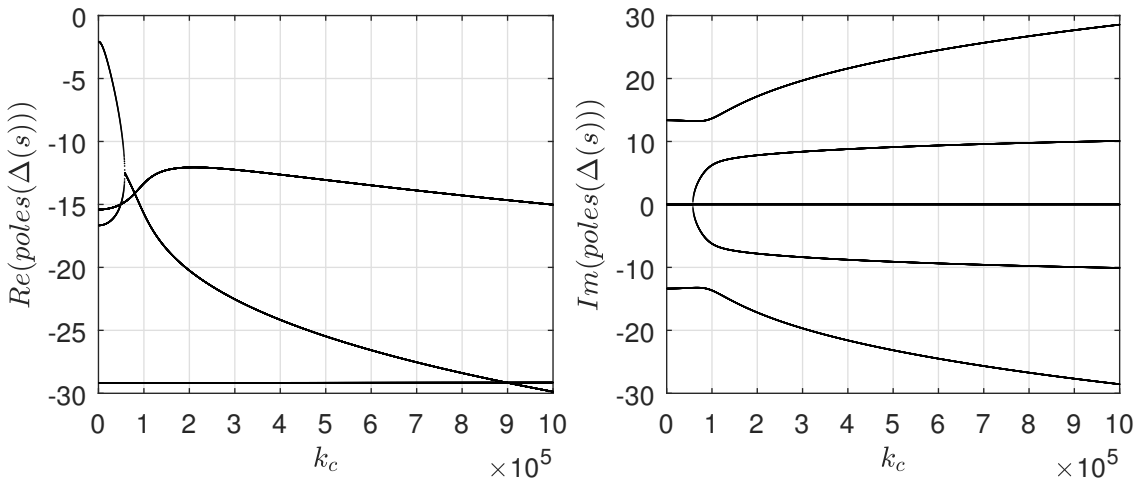

Figure 4.5: Trend of $\Delta(s)$ by investigating the poles for a fixed vehicle speed of $v = 20\,\mathrm{km/h}$. For small values of k_{c}, the resulting polynomial is exactly the same as $\nu(s)$ from the plant $P(s)$. This means that the slowest possible result is the speed of the plant itself. For ascending values of k_{c}, the poles travel more into the negative real plane, which represents increasing speed and aggressiveness of the controller.

4.1.3 Structure-variable extension for different vehicle speeds

As investigated in Chapter 3, the system changes it's behavior with the vehicle speed. In order to consider also this effect, the controller structure was extended with a structure-variable control according to Adamy [20].

The idea of this non-linear method is to increase the performance by using many controllers for different system states. Here, this changing parameter is the vehicle speed. To avoid a huge implementation effort by a high number of controllers, it is also possible to use only two controllers that operate in parallel mode. If the vehicle speed changes, the controllers continuously get new controller parameters and get resetted in a way, that doesn't affect the controller output with any disturbances. In order to allow this kind of structure, a proper switching logic needs to be developed that controls the operation modes of the two controllers (Figure 4.6).

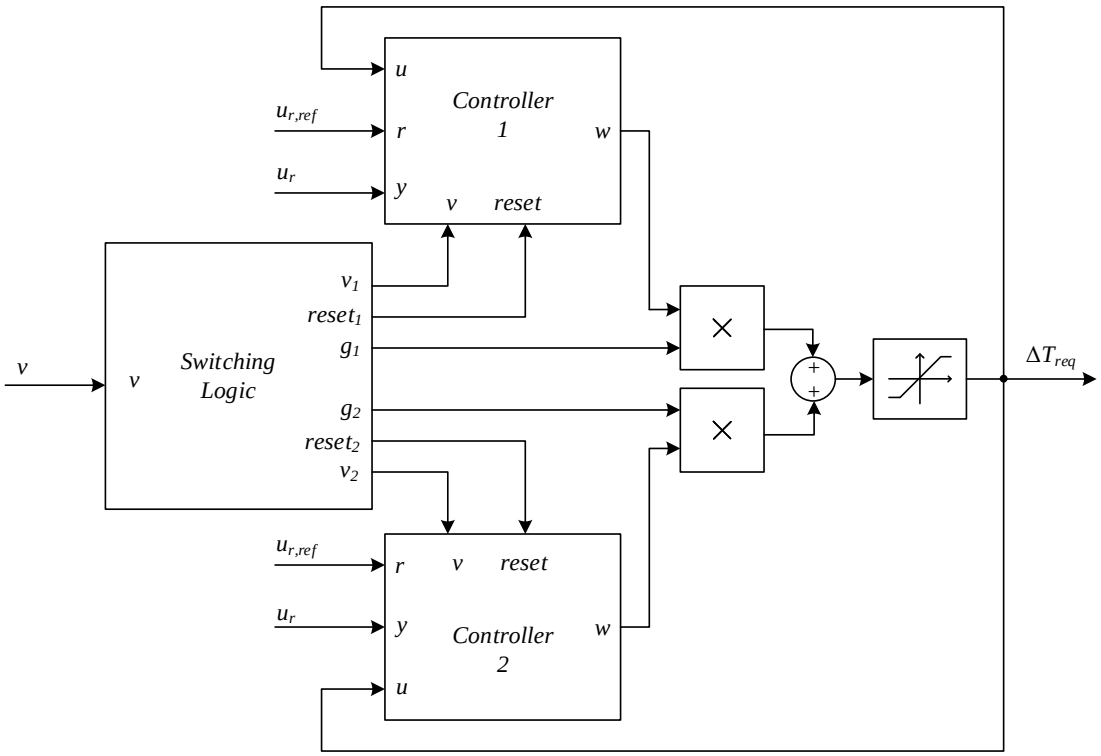

Figure 4.6: Structure-variable extension to the latter designed controller concept. A second controller of same type operates in parallel mode with the other. The switching logic discretizes the actual vehicle speed and is responsible for the switching and mixing process of the two controllers. Dependent on this discretized vehicle speed, the controllers continously get new parameters.

It was decided to design different controllers in a vehicle speed range from $20\,\mathrm{km/h} < v < 100\,\mathrm{km/h}$ with a discretization step of $v_{\mathrm{space}} = 5\,\mathrm{km/h}$. Inside of this range, the controller output will be mixed by two of these designed controllers, depending on the actual and the discretized vehicle speeds. For vehicle speeds $v < 20\,\mathrm{km/h}$ or $v > 100\,\mathrm{km/h}$, just one controller is producing the controller output, the one designed at the boundary of this range.

The logic, how theses controllers are acting together, is defined in the switching logic (see Figure 4.6). With the modulus operator,

$$v_{\mathrm{mod}} = \mathrm{mod}\left(v, v_{\mathrm{space}}\right) \tag{4.57}$$

the distance to discretized speeds, below and above the actual speed, can be determined. With this distance, a sliding function

$$\varphi = \frac{1}{2}\left(1 + \frac{\tanh\left(8\,\frac{v_{\mathrm{mod}}}{v_{\mathrm{space}}} - 4\right)}{\tanh\left(4\right)}\right) \tag{4.58}$$

was defined to calculate the gains g_1 and g_2 of the two controller outputs as in Figure 4.6. With the relations

$$g_1 + g_2 \overset{!}{=} 1 \tag{4.59}$$

$$g_1, g_2 \geq 0, \tag{4.60}$$

either $g_1 = \varphi$ or $g_2 = \varphi$, dependent on the speed slot that is implemented in the 2 controllers. Figure 4.7 shows the strategy that is used in the switching logic.

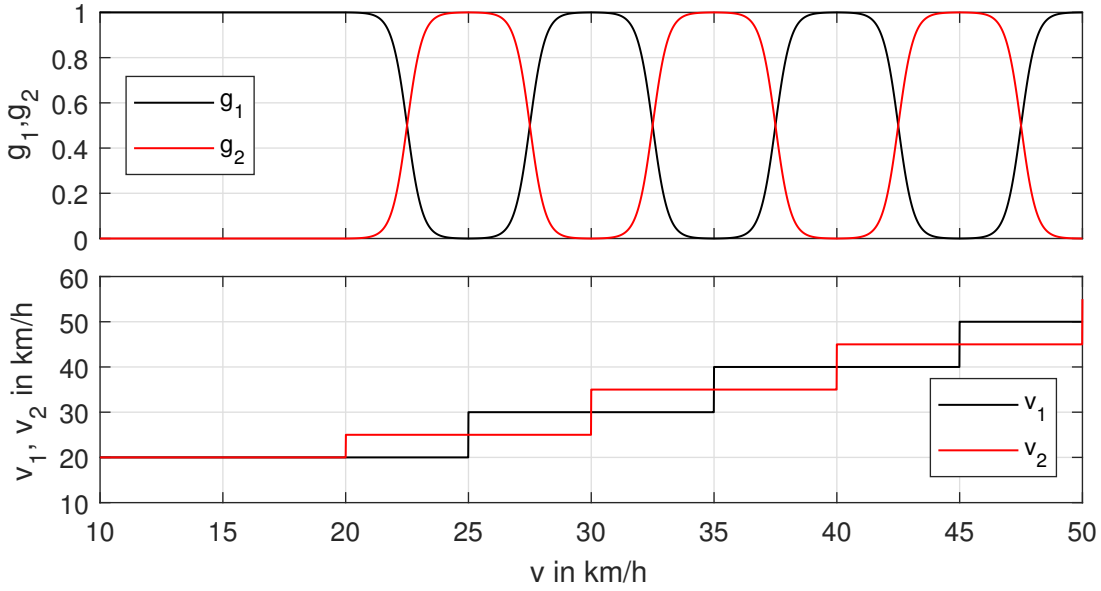

Figure 4.7: Switching logic of the structure-variable extension. v_1 and v_2 depict the discretized vehicle speeds of both controllers. When one of the controllers switches to the next discretized speed, the related gain is 0. This means that possible discontinuities during the switching process do not affect the controller output.

When switching from one discretized speed to the next, the controller gets new paramaters and needs to be redesigned. These parameters are realized with pre-designed lookup tables to minimize computational effort during operative service.

4.2 Cascaded rack position controller

Another possible controller concept, which is very common in robotics and laser positioning, is the use of a cascaded controller structure. The idea is to split up the control problem into a subproblem in an inner loop, and the main problem in the outer loop. Figure 4.8 shows a general structure of a cascaded control system.

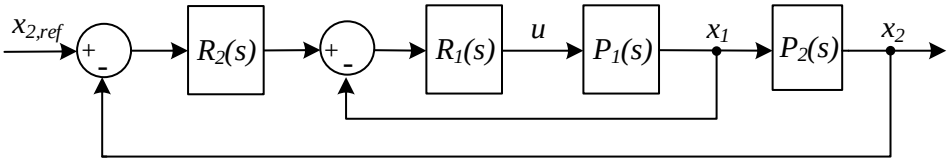

Figure 4.8: General structure of a cascaded control system. $R_1(s)$ in an inner loop controls the quantity x_1 which is described by the system $P_1(s)$. This subproblem is designed without any consideration of the outer problem. The outer loop with $R_2(s)$ then controls the desired control target x_2. $P_2(s)$ describes the behavior from x_1 to x_2.

A big advantage of this design is the use of multiple sensors. Compared to a single-measurement controller, like the one from Section 4.1, the control system gets more information about the system's state which can lead to a significantly better performance of the overall system. But this design has also some drawbacks. According to VanDoren in [21], a cascaded controller design has to fullfill several requirements:

1. The actions of the inner controller must affect the primary control target in a predictable and repeatable way.
2. The inner loop has to be faster than the outer loop in order to allow the inner controller enough time to compensate inner loop disturbances before they can affect the main process.
3. The disturbances of the inner loop have to be less severe than the disturbances from the outer loop.

In order to control the rack position u_r, the logical inner loop is the control of the rack velocity $\dot{u}_\mathrm{r}$. It directly affects the rack position, as there is no rack movement without a rack velocity. Moreover, disturbances of the inner loop are attenuated very well, since $P_2(s)$ has the form of a simple integrator. This reasons makes the system particularly amenable to cascade control.

A further advantage is that there is no need for additional integral action in the outer loop controller $R_2(s)$, since the system already has integral behavior in $P_2(s)$. This means that there is no need for anti windup strategies in the outer loop, which simplifies the controller design of $R_2(s)$ significantly.

To improve the reference tracking behavior, also a feed forward compensation can be added to the structure. This compensation can be described ideally by a dynamic system of the inverse of $P_2(s)$ with the target reference as input. In most cases, this inverse is not implementable, which means that the compensation has to be described by an approximation $N(s) \approx P_2^{-1}(s)$. The updated structure is shown in Figure 4.9.

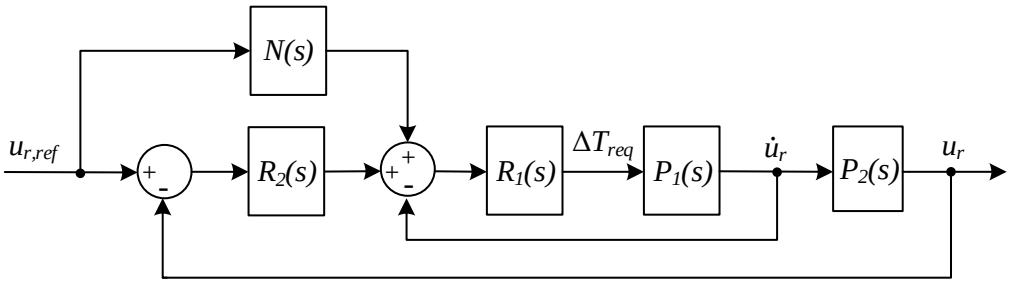

Figure 4.9: Rack position cascade control with feed forward compensation. The compensation is added to the error signal of the inner loop in order to improve the performance of the reference tracking. $N(s)$ represents an approximate of $P_2^{-1}(s)$.

The inner loop controller $R_1(s)$ has to be designed first without consideration of the outer loop. The performance can be described with the closed loop transfer function

$$T_1(s) = \frac{R_1(s)\,P_1(s)}{1 + R_1(s)\,P_1(s)}. \tag{4.61}$$

With a compensatory open loop transfer function

$$P_\mathrm{c}(s) = T_1(s)\,P_2(s) = \frac{R_1(s)\,P_1(s)\,P_2(s)}{1 + R_1(s)\,P_1(s)}, \tag{4.62}$$

the outer controller $R_2(s)$ can be designed. The overall input-output behavior of the closed loop system is then described by

$$T(s) = \frac{P_\mathrm{c}(s)\,[N(s) + R_2(s)]}{1 + R_2(s)\,P_\mathrm{c}(s)}. \tag{4.63}$$

4.2.1 Inner rack velocity controller

For determination of essential properties for the inner controller, the plant $P_1(s)$ has to be investigated first. Since the rack velocity is the derivative of the rack position, it is very easy to derive the transfer function out of the results from Section 3 by a simple multiplication of

$$P_1(s) = P(s)\,s. \tag{4.64}$$

Investigating the poles and zeros from Figure 3.13 and the bode plot from Figure 3.14, it's clear that this transfer function in general has the form

$$P_1(s) = c_\mathrm{P}\,\frac{s\;(s + z_1)\,(s + z_2)}{(s + p_1)\,(s + p_2)\,(s + p_3)\,(s + p_4)\,(s + p_5)} \tag{4.65}$$

whereas the poles p_4 and p_5 get a complex pair of poles at around $v = 15\,\mathrm{km/h}$ which represents the resonance characteristic of the rack. Around $v = 40\,\mathrm{km/h}$, also p_2 and p_3 get a complex pair of poles, which represents the characteristic frequency of the chassis.

With this information of $P_1(s)$, the requirements for the inner-loop controller can be defined:

1. Because of the zero at $s = 0$, the controller will need a double integrator in order to allow offset-free tracking of the reference.

2. To attenuate possible resonance effects on the steering rack, the controller needs a complex pair of zeros, tuned to that characteristic frequency.

To fulfill these requirements, a simple controller approch

$$R_1(s) = k_\mathrm{r} \frac{(s + z_\mathrm{r})\left(s^2 + d_\mathrm{r}\, s + \omega_r^2\right)}{s^2\,(s + p_\mathrm{r})} \tag{4.66}$$

was chosen with a double pole at $s = 0$ that represents the double integrator. With $\omega_r = 2\,\pi\, f_r$, the complex pair of zeros can be tuned to a certain frequency f_r. The damping coefficient d_r then determines the attenuation of this frequency. Additionally, this controller structure is equipped with another pole/zero pair $z_\mathrm{r}, p_\mathrm{r}$ to compensate a pole/zero pair of the plant $P_1(s)$. K is the controller gain, which determines the resulting speed of the control system.

Furthermore, this approach is transformed into a state space realization. By rearranging equation (4.66), $R_1(s)$ has also the form

$$\begin{aligned} R_1(s) &= \frac{s^3\, k_\mathrm{r} + s^2\, k_\mathrm{r}\,(d_\mathrm{r} + z_\mathrm{r}) + s\, k_\mathrm{r}\left(\omega_r^2 + z_\mathrm{r}\, d_\mathrm{r}\right) + k_\mathrm{r}\, z_\mathrm{r}\, \omega_r^2}{s^3 + s^2\, p_\mathrm{r}} \\ &= k_\mathrm{r} + \frac{s^2\, k_\mathrm{r}\,(d_\mathrm{r} + z_\mathrm{r} - p_\mathrm{r}) + s\, k_\mathrm{r}\left(\omega_r^2 + z_\mathrm{r}\, d_\mathrm{r}\right) + k_\mathrm{r}\, z_\mathrm{r}\, \omega_r^2}{s^3 + s^2\, p_\mathrm{r}}. \end{aligned} \tag{4.67}$$

Using the observability normal from [17], the inner controller finally can be stated as

$$\dot{\boldsymbol{z}} = \begin{bmatrix} 0 & 0 & 0 \\ 1 & 0 & 0 \\ 0 & 1 & -p_\mathrm{r} \end{bmatrix} \boldsymbol{z} + \begin{bmatrix} k_\mathrm{r}\, z_\mathrm{r}\, \omega_r^2 \\ k_\mathrm{r}\left(\omega_r^2 + z_\mathrm{r}\, d_\mathrm{r}\right) \\ k_\mathrm{r}\,(d_\mathrm{r} + z_\mathrm{r} - p_\mathrm{r}) \end{bmatrix} (r - y) \tag{4.68}$$

$$w = \begin{bmatrix} 0 & 0 & 1 \end{bmatrix} \boldsymbol{z} + k_\mathrm{r}\,(r - y) \tag{4.69}$$

with three controller states $\boldsymbol{z}$, r as the rack velocity reference, y as the measured rack velocity, and w as the controller output. Similar to the controller of Section 4.1, windup effects due to the integral action of the controller are a problem. To handle these problems, R. Hanus introduced in 1987 a general anti-windup method that fits well for this kind of problem [22]. The base for this method is a controller in state space realization

$$\dot{\boldsymbol{z}} = \boldsymbol{A}_\mathrm{r}\, \boldsymbol{z} + \boldsymbol{b}_{1\mathrm{r}}\, r + \boldsymbol{b}_{2\mathrm{r}}\, y \tag{4.70}$$

$$w = \boldsymbol{c}_\mathrm{r}^\mathrm{T}\, \boldsymbol{z} + d_{1\mathrm{r}}\, r + d_{2\mathrm{r}}\, y \tag{4.71}$$

whereas the controller output w is saturated by

$$u = \begin{cases} u_\mathrm{max}, & \text{when } w > u_\mathrm{max} \\ u_\mathrm{min}, & \text{when } w < u_\mathrm{min} \\ w, & \text{otherwise.} \end{cases} \tag{4.72}$$

Then, the saturated controller output u is used as input for the plant $P_1(s)$. In the saturated case $w \neq u$, the idea of Hanus is to calculate a virtual reference $\tilde{r}$ to ensure $w = u$. For a better distinction between the original controller (equations (4.70) to (4.71)), a copy

$$\dot{\tilde{\boldsymbol{z}}} = \boldsymbol{A}_\mathrm{r}\,\tilde{\boldsymbol{z}} + \boldsymbol{b}_{1\mathrm{r}}\,\tilde{r} + \boldsymbol{b}_{2\mathrm{r}}\,y \tag{4.73}$$

$$u = \boldsymbol{c}_\mathrm{r}^\mathrm{T}\,\tilde{\boldsymbol{z}} + d_{1\mathrm{r}}\,\tilde{r} + d_{2\mathrm{r}}\,y \tag{4.74}$$

$$w = \boldsymbol{c}_\mathrm{r}^\mathrm{T}\,\tilde{\boldsymbol{z}} + d_{1\mathrm{r}}\,r + d_{2\mathrm{r}}\,y \tag{4.75}$$

that produces the saturated controller output u with the virtual reference $\tilde{r}$ and the unsaturated controller output w with the actual reference r is made. By subtracting

$$u - w = d_{1\mathrm{r}}\,(\tilde{r} - r)\,, \tag{4.76}$$

the virtual reference can be calculated by

$$\tilde{r} = r + \frac{1}{d_{1\mathrm{r}}}\,(u - w)\,. \tag{4.77}$$

Inserting this virtual reference into equation (4.73),

$$\begin{aligned}
\dot{\tilde{\boldsymbol{z}}} &= \boldsymbol{A}_\mathrm{r}\,\tilde{\boldsymbol{z}} + \boldsymbol{b}_{1\mathrm{r}}\,\tilde{r} + \boldsymbol{b}_{2\mathrm{r}}\,y \\
&= \boldsymbol{A}_\mathrm{r}\,\tilde{\boldsymbol{z}} + \boldsymbol{b}_{1\mathrm{r}}\,r + \frac{\boldsymbol{b}_{1\mathrm{r}}}{d_{1\mathrm{r}}}\,(u - w) + \boldsymbol{b}_{2\mathrm{r}} \\
&= \boldsymbol{A}_\mathrm{r}\,\tilde{\boldsymbol{z}} + \boldsymbol{b}_{1\mathrm{r}}\,r + \frac{\boldsymbol{b}_{1\mathrm{r}}}{d_{1\mathrm{r}}}\,u - \frac{\boldsymbol{b}_{1\mathrm{r}}}{d_{1\mathrm{r}}}\,\boldsymbol{c}_\mathrm{r}^\mathrm{T}\,\tilde{\boldsymbol{z}} - \frac{\boldsymbol{b}_{1\mathrm{r}}}{d_{1\mathrm{r}}}\,d_{1\mathrm{r}}\,r - \frac{\boldsymbol{b}_{1\mathrm{r}}}{d_{1\mathrm{r}}}\,d_{2\mathrm{r}}\,y + \boldsymbol{b}_{2\mathrm{r}}\,y \\
&= \left(\boldsymbol{A}_\mathrm{r} - \frac{\boldsymbol{b}_{1\mathrm{r}}}{d_{1\mathrm{r}}}\,\boldsymbol{c}_\mathrm{r}^\mathrm{T}\right)\tilde{\boldsymbol{z}} + \frac{\boldsymbol{b}_{1\mathrm{r}}}{d_{1\mathrm{r}}}\,u + \left(\boldsymbol{b}_{2\mathrm{r}} - \boldsymbol{b}_{1\mathrm{r}}\frac{d_{2\mathrm{r}}}{d_{1\mathrm{r}}}\right)y
\end{aligned} \tag{4.78}$$

the so called *conditioned controller according to Hanus* is given by

$$\dot{\tilde{\boldsymbol{z}}} = \left(\boldsymbol{A}_\mathrm{r} - \frac{\boldsymbol{b}_{1\mathrm{r}}}{d_{1\mathrm{r}}}\,\boldsymbol{c}_\mathrm{r}^\mathrm{T}\right)\tilde{\boldsymbol{z}} + \frac{\boldsymbol{b}_{1\mathrm{r}}}{d_{1\mathrm{r}}}\,u + \left(\boldsymbol{b}_{2\mathrm{r}} - \boldsymbol{b}_{1\mathrm{r}}\frac{d_{2\mathrm{r}}}{d_{1\mathrm{r}}}\right)y \tag{4.79}$$

$$w = \boldsymbol{c}_\mathrm{r}^\mathrm{T}\,\tilde{\boldsymbol{z}} + d_{1\mathrm{r}}\,r + d_{2\mathrm{r}}\,y. \tag{4.80}$$

In the unsaturated case, this controller behaves exactly the same as the original controller from equations (4.70) and (4.71), which can be proved by inserting equation (4.80) into (4.79) by setting $w = u$. Whereas in the saturated case, the controller avoids windup effects of the integrator by using a virtual reference as input.

The success of this method depends on the following requirements:

1. The original controller has to provide stability of the closed loop system.
2. The controller parameter $d_{1\mathrm{r}} \overset{!}{\neq} 0$.
3. The eigenvalues $\mathrm{eig}\left(\boldsymbol{A}_\mathrm{r} - \frac{\boldsymbol{b}_{1\mathrm{r}}}{d_{1\mathrm{r}}}\,\boldsymbol{c}_\mathrm{r}^\mathrm{T}\right)$ must have negative real values.
4. In the saturated case, where $w \neq u$, w must approach u in finite time.

The last requirement can be verified by the steady state property

$$-\boldsymbol{c}_\mathrm{r}^\mathrm{T}\left(\boldsymbol{A}_\mathrm{r} - \frac{\boldsymbol{b}_{1\mathrm{r}}}{d_{1\mathrm{r}}}\,\boldsymbol{c}_\mathrm{r}^\mathrm{T}\right)^{-1}\left(\frac{\boldsymbol{b}_{1\mathrm{r}}}{d_{1\mathrm{r}}} + \left(\boldsymbol{b}_{2\mathrm{r}} - \boldsymbol{b}_{1\mathrm{r}}\frac{d_{2\mathrm{r}}}{d_{1\mathrm{r}}}\right)P(0)\right) + (d_{1\mathrm{r}} + d_{2\mathrm{r}})\,P(0) \overset{!}{=} 1 \tag{4.81}$$

Applying this anti windup method to the original controller of equations (4.70) and (4.71), the related conditioned controller has the form

$$\dot{\boldsymbol{z}} = \begin{bmatrix} 0 & 0 & -z_\mathrm{r}\omega_r^2 \\ 1 & 0 & -\omega_r^2 - z_\mathrm{r}\, d_\mathrm{r} \\ 0 & 1 & -d_\mathrm{r} - z_\mathrm{r} \end{bmatrix} \boldsymbol{z} + \begin{bmatrix} z_\mathrm{r}\,\omega_r^2 \\ \omega_r^2 + z_\mathrm{r}\, d_\mathrm{r} \\ d_\mathrm{r} + z_\mathrm{r} - p_\mathrm{r} \end{bmatrix} u \tag{4.82}$$

$$w = \begin{bmatrix} 0 & 0 & 1 \end{bmatrix} \boldsymbol{z} + k_\mathrm{r}\,(r - y) \tag{4.83}$$

with $\boldsymbol{z}$ as the conditioned controller states, u as the saturated controller output, w as the unsaturated controller output, r as the reference and y as the measured control target.

4.2.2 Outer rack position controller

As described earlier in this section, a feed forward compensation is added to the reference signal of the inner controller. This compensation is realized by

$$N(s) = \frac{100\,s}{s + 100}, \tag{4.84}$$

a filtered differentiator that generates the derivate of the reference rack position $u_{\mathrm{r,ref}}$. If the inner controller is able to follow this trajectory well enough, the outer rack position controller only needs to correct control errors from the inner loop controller and possible disturbances from the outer loop. A design of

$$R_2(s) = k_\mathrm{P} \tag{4.85}$$

with the controller gain k_P was chosen. With the integral action in

$$P_2(s) = \frac{P(s)}{P_1(s)} = \frac{1}{s}, \tag{4.86}$$

offset-free reference tracking of $u_{\mathrm{r,ref}}$ is guaranteed.

4.3 Discretization of the controllers

The results of the introduced controller concepts from Sections 4.1 and 4.2 are both in a state-space realization in continuous time of form

$$\dot{\boldsymbol{z}} = \boldsymbol{A}_\mathrm{r}\,\boldsymbol{z} + \boldsymbol{B}_\mathrm{r}\,\boldsymbol{u} \tag{4.87}$$

$$w = \boldsymbol{c}_\mathrm{r}^\mathrm{T}\,\boldsymbol{z} + \boldsymbol{d}_\mathrm{r}^\mathrm{T}\,\boldsymbol{u} \tag{4.88}$$

with a general input vector $\boldsymbol{u} = \begin{bmatrix} r & u & y \end{bmatrix}^\mathrm{T}$ that consists the reference r, the saturated controller output u and the measured control target y. For the use in embedded hardware on the real car, continuous time systems cannot be realized and need to be transformed into discrete time. There are many methods to discretize continuous time systems, one of them is given by investigating the solution of the inhomogeneous matrix equation (4.87)

$$\boldsymbol{z}(t) = \mathrm{e}^{\boldsymbol{A}_\mathrm{r} t}\,\boldsymbol{z}_0 + \int_0^t \mathrm{e}^{\boldsymbol{A}_\mathrm{r}(t-\tau)}\,\boldsymbol{B}_\mathrm{r}\,\boldsymbol{u}(\boldsymbol{\tau})\,\mathrm{d}\tau. \tag{4.89}$$

Introducing a sample time t_s, this solution at time $t = t_\mathrm{s}$ is then given by

$$\boldsymbol{z}(t_\mathrm{s}) = \mathrm{e}^{\boldsymbol{A}_\mathrm{r} t_\mathrm{s}}\,\boldsymbol{z}_0 + \int_0^{t_\mathrm{s}} \mathrm{e}^{\boldsymbol{A}_\mathrm{r}(t_\mathrm{s}-\tau)}\,\boldsymbol{B}_\mathrm{r}\,\boldsymbol{u}(\boldsymbol{\tau})\,\mathrm{d}\tau. \tag{4.90}$$

By holding the input vector

$$\boldsymbol{u}(\boldsymbol{t}) = \boldsymbol{u_0} \qquad \text{for } 0 \le t < t_\mathrm{s}, \tag{4.91}$$

constant, the integral can be solved by

$$\begin{aligned} \boldsymbol{z}(t_\mathrm{s}) &= \mathrm{e}^{\boldsymbol{A}_\mathrm{r} t_\mathrm{s}}\,\boldsymbol{z}_0 + \int_0^{t_\mathrm{s}} \mathrm{e}^{\boldsymbol{A}_\mathrm{r}(t_\mathrm{s}-\tau)}\,\boldsymbol{B}_\mathrm{r}\,\boldsymbol{u_0}\,\mathrm{d}\tau \\ &= \mathrm{e}^{\boldsymbol{A}_\mathrm{r} t_\mathrm{s}}\,\boldsymbol{z}_0 + \boldsymbol{A}_\mathrm{r}^{-1}\left(\mathrm{e}^{\boldsymbol{A}_\mathrm{r} t_\mathrm{s}} - \mathbf{I}\right)\boldsymbol{B}_\mathrm{r}\,\boldsymbol{u_0}. \end{aligned} \tag{4.92}$$

Because of linearity and time invariance, this solution is recursive for any timestep $t = k\,t_\mathrm{s}$. The system can now be described in a discrete time state space notation

$$\boldsymbol{z}_{\mathrm{k}+1} = \boldsymbol{A}_\mathrm{rd}\,\boldsymbol{z}_\mathrm{k} + \boldsymbol{B}_\mathrm{rd}\,\boldsymbol{u}_\mathrm{k} \tag{4.93}$$

$$w_\mathrm{k} = \boldsymbol{c}_\mathrm{rd}^\mathrm{T}\,\boldsymbol{z}_\mathrm{k} + \boldsymbol{d}_\mathrm{rd}^\mathrm{T}\,\boldsymbol{u}_\mathrm{k} \tag{4.94}$$

with

$$\boldsymbol{A}_\mathrm{rd} = \mathrm{e}^{\boldsymbol{A}_\mathrm{r} t_\mathrm{s}} \tag{4.95}$$

$$\boldsymbol{B}_\mathrm{rd} = \boldsymbol{A}_\mathrm{r}^{-1}\left(\mathrm{e}^{\boldsymbol{A}_\mathrm{r} t_\mathrm{s}} - \mathbf{I}\right)\boldsymbol{B}_\mathrm{r} \tag{4.96}$$

$$\boldsymbol{c}_\mathrm{rd}^\mathrm{T} = \boldsymbol{c}_\mathrm{r}^\mathrm{T} \tag{4.97}$$

$$\boldsymbol{d}_\mathrm{rd}^\mathrm{T} = \boldsymbol{d}_\mathrm{r}^\mathrm{T}. \tag{4.98}$$

5 Results

In this chapter, the described controller concepts from Chapter 4 will be implemented, parametrized, validated and verified. As a preparation, these investigations are made first in simulations. With the pre-tuned controllers from these simulations, tests on the demonstrator vehicle are made and the tuning of the controller will be adjusted. Furthermore, upcoming problems will be identified and discussed. Also the transition from SbW to SbTV will be investigated and tested on the demonstrator vehicle.

5.1 Simulation Results

The idea of using a simulation first, is to gain knowledge about the influence of the controller parameters. A found parameter set that works well in the simulations, will provide a good starting point for the tuning process on the real car. This will save a lot of time and costs, since there is less need for making tests on the demonstrator vehicle.

An important aspect of control systems is the stability of the system. Especially for non-linear systems, the prove of stability is not easy to gain. For this thesis, the stability of the closed loop system will be guaranteed for the use with the linear model from Chapter 3. The stability of the non-linear system (the real car) can be investigated with different driving maneuvers.

Also for the simulations, the stability for a set of controller parameters was proved for the linear model first and investigated for the non-linear simulation by various maneuvers afterwards. Then, a set that is well below the boundaries of stability has been chosen as the controller parameters.

5.1.1 State feedback controller

The state feedback controller from Section 4.1 has been designed to provide a easy tuning by only 2 parameters, k_c and k_o, which either represent a design parameter for the controller and observer polynomial. The *higher* these values are, the *more negative* the roots of the polynomials get, which increases the speed of either the controller or the observer.

A big advantage of this tuning is that this systematic approach based on LQR provides always a stable closed loop system regarding the linear model, which is used for the controller design [19]. By trying different pairs of these parameters, the set, which is presented in Table 5.1, ensured stability of the non-linear simulation for every tried experiment.

Table 5.1: Parameters for the state feedback controller used for the simulations.

Param.	Value	Description
k_c	$5 \cdot 10^5$	Design parameter for the controller polynomial
k_o	$1 \cdot 10^5$	Design parameter for the observer polynomial

With this set of parameters, the behavior of the closed loop system was investigated in Figures 5.1 to 5.3. As controlling of SbTV gets more difficult at low speeds, it was decided to make the experiments at a vehicle speed of $v = 20\,\mathrm{km/h}$.

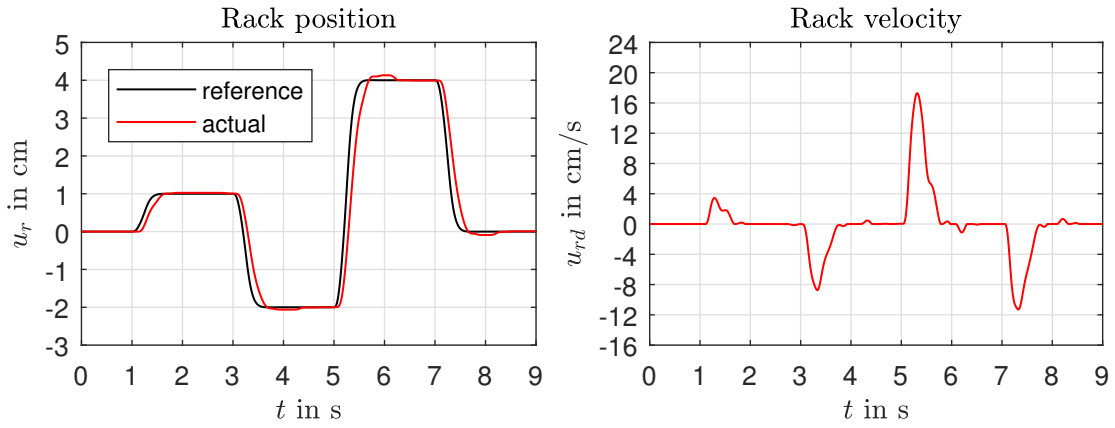

Figure 5.1: Step steer maneuver at different amplitudes and $v = 20\,\mathrm{km/h}$ using the state feedback controller.

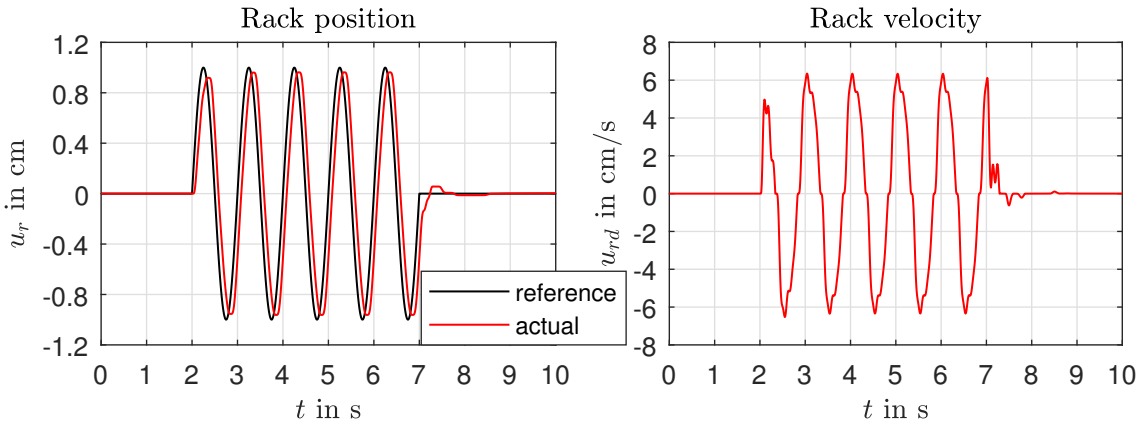

Figure 5.2: Sine maneuver at frequency $f = 1\,\mathrm{Hz}$ and $v = 20\,\mathrm{km/h}$ using the state feedback controller.

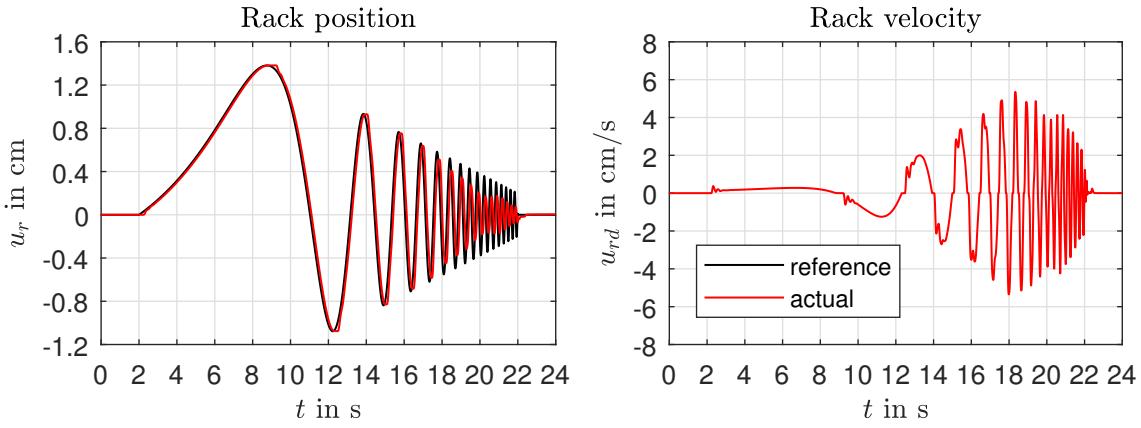

Figure 5.3: Sweep maneuver at frequency range from $0.01\,\mathrm{Hz} < f < 3\,\mathrm{Hz}$ and $v = 20\,\mathrm{km/h}$ using the state feedback controller. With this setup, the controller gain at the rack resonance is well attenuated and does not produce any problems.

One can see clearly that the controller produces a significant phase delay between the reference and the controlled rack position. This problem could not be avoided, as with higher controller speeds, the resonance of the rack would make the closed loop system unstable. This lack of performance (even in the simulation) was the main reason, why a second controller principle, the cascaded rack position controller, was developed.

5.1.2 Cascaded rack position controller

The tuning of the cascaded rack position controller is based on the transfer function of the linear model $P_1(s)$. This transfer function at a vehicle speed of $v = 20\,\mathrm{km/h}$ is given by

$$P_1(s) = -0.02231\,\frac{s\,(s+29.13)\,(s+46.41)}{(s+2.069)\,(s+16.67)\,(s+29.18)\,(s^2+30.81\,s+415.9)}. \tag{5.1}$$

By choosing the controller parameters using the poles and zeros from $P(s)$, the controller is given by

$$R_1(s) = k_\mathrm{r}\frac{(s+2.069)\left(s^2+30.81\,s+415.9\right)}{s^2\,(s+46.41)}. \tag{5.2}$$

Then, the open loop transfer function can be calculated as

$$L_1(s) = R_1(s)\,P_1(s) = -0.02231\,k_\mathrm{r}\frac{(s+29.13)}{s\,(s+16.67)\,(s+29.18)} \approx \frac{-0.02231\,k_\mathrm{r}}{s\,(s+16.67)}. \tag{5.3}$$

According to [17], the stability of the closed loop can be guaranteed by investigating the phase of the open loop transfer function. If the phase at the cutoff frequency (where $abs(L_1(s)) \stackrel{!}{=} 1$) is higher than $-180\,°$, the closed loop is stable. For a negative value of k_r, the phase in this situation will be never smaller than $-180\,°$, which ensures the closed loop stability for

$$k_\mathrm{r} < 0. \tag{5.4}$$

Also in the non-linear simulation model, the closed loop remained stable even for very high values of k_r. A value of $k_\mathrm{r} = -7.5 \cdot 10^4$ had been chosen. With the combination of the feed forward compensation, the quality of the inner loop resulted very good. Therefore, the P-controller of the outer loop was designed with a low value of $k_\mathrm{p} = 1$. The resulting controller parameters are stated in Table 5.2.

Table 5.2: Parameters for the cascaded rack position controller used for the simulations.

Param.	Value	Description
k_r	$-7.5 \cdot 10^4$	Gain of inner loop controller
z_r	2.069	Controller zero
p_r	46.41	Controller pole
d_r	30.81	Damping coefficient of complex pair of zeros
ω_r	20.394	Normalized frequency of complex pair of zeros
k_p	1	Gain of outer loop controller

Different to the state-feedback controller, only one controller for one vehicle speed at $v = 20\,\mathrm{km/h}$ has been designed. This controller worked also for different speeds very well.

Figures 5.4 to 5.6 show the same experiments as in Figures 5.1 to 5.3, for a direct comparison between the state feedback - and the cascaded controller.

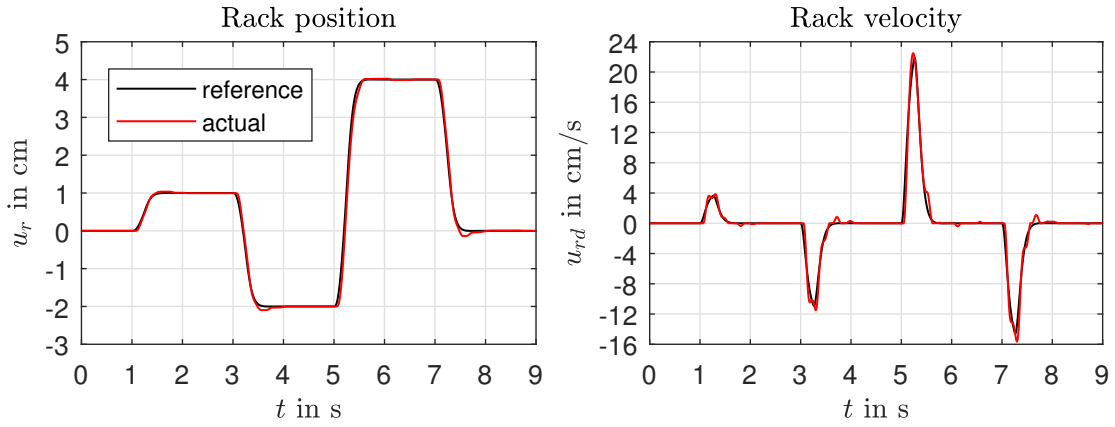

Figure 5.4: Step steer maneuver at different amplitudes and $v = 20\,\mathrm{km/h}$ using the cascaded rack position controller.

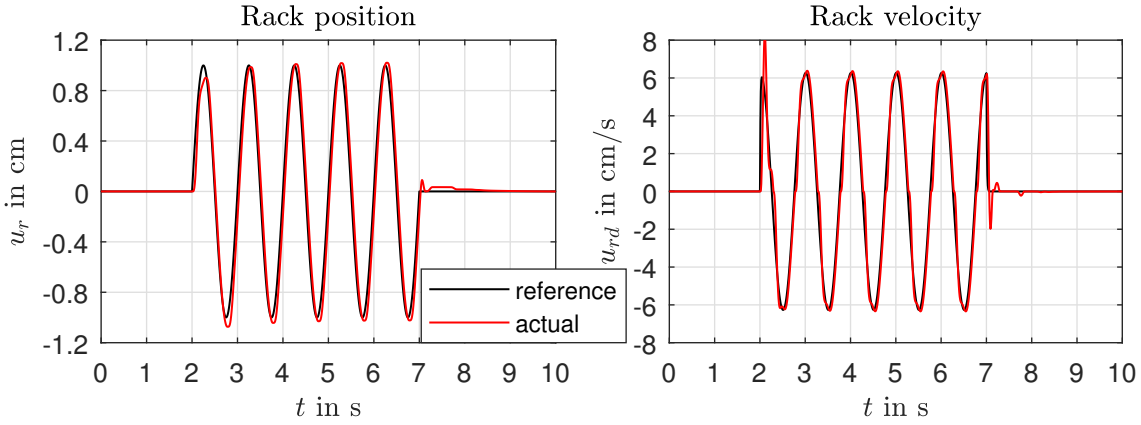

Figure 5.5: Step steer maneuver at different amplitudes and $v = 20\,\mathrm{km/h}$ using the cascaded rack position controller.

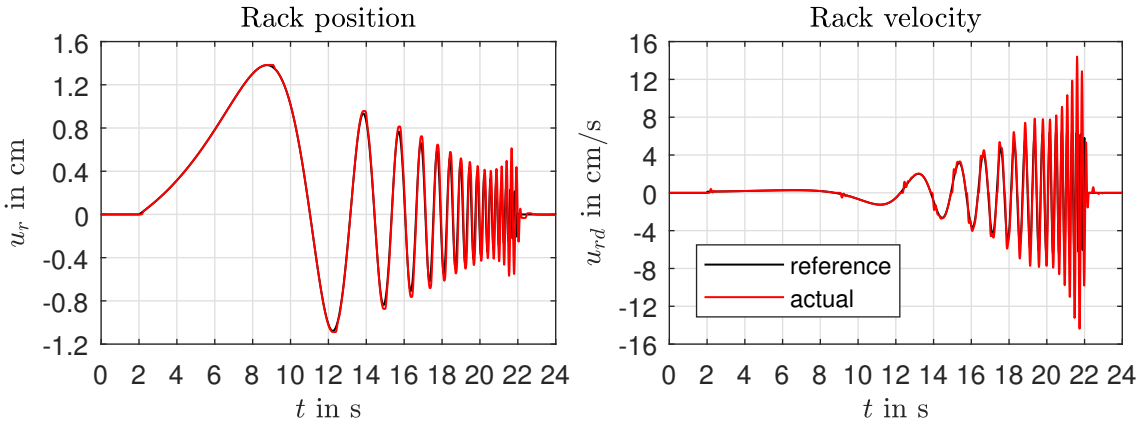

Figure 5.6: Step steer maneuver at different amplitudes and $v = 20\,\mathrm{km/h}$ using the cascaded rack position controller. The gain at high frequencies is higher as with the state feedback controller. Some slight resonance characteristics can be seen.

Compared to the state feedback controller, the performance of the cascaded controller is

much higher. The phase delay got smaller and the rack movement itself got smoother. There are some slight resonance effects in the sweep, since the controller is much more aggressive than the state feedback controller. When looking closer to the rack velocity, one can see discontinuities when passing the origin. This comes from the static friction of the rack, which needs to be overcome when changing the direction of movement.

5.1.3 Influence of the rack friction

The rack friction (especially the static part of it) does not only produce some slight discontinuities when changing direction, there are also some other effects that need to be discussed.

Having a static friction in a system means that a certain force has to be generated first in order to allow any movement of the system. In the SbTV system, this force is generated by the differential torque ΔT. Since the static friction is not considered in linear controller theory, this effect leads to time-delays, which are unavoidable (Figure 5.7).

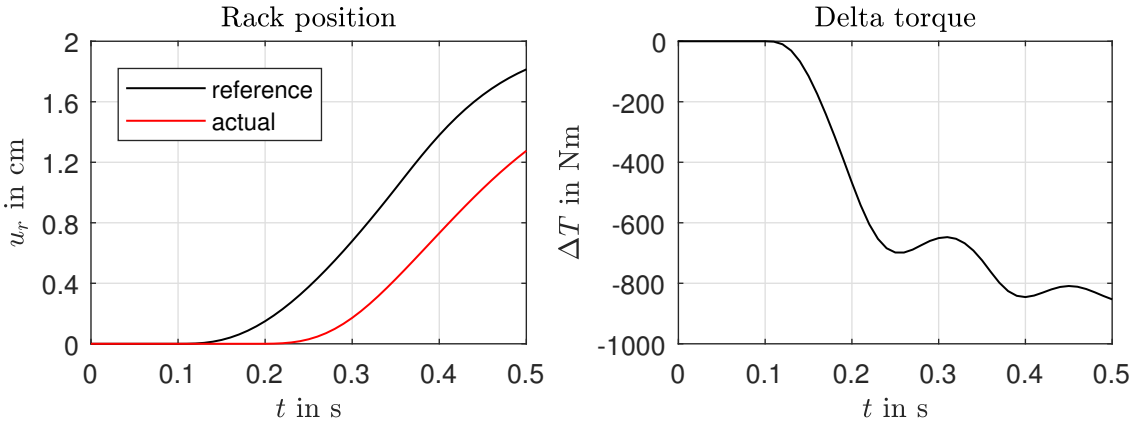

Figure 5.7: A simulated step steer on the closed loop system using the state feedback controller. One can see on the right plot that it takes about 100 ms to build up enough torque to overcome the static friction. The result is a significant time delay.

One possible solution to minimize these time-delays is to increase the controller gains in order to build up the necessary torques faster. But this will be always a compromise between a minimized time-delay and the stability of the closed loop system (since higher controller gains tend to make the closed loop unstable).

High controller gains bring additional problems, the effect of *limit cycles*. They occur when it comes to steady state conditions like going straight or cornering at constant radius. At these situations, the control error in these situation between the reference and actual rack position is very small, the controller just wants to follow the reference exactly. But even for very small movements, the controller needs to overcome the whole static friction. Because of the dynamics in between, it takes some time to „convert“ the driving torques into a rack force. Since the controller gets no immediate reaction, too much torque will be built up and the rack tears off. An overshoot over the reference is unavoidable and the controller has to face the same problem from the opposite side. Figure 5.8 shows this effect for a steady state cornering situation.

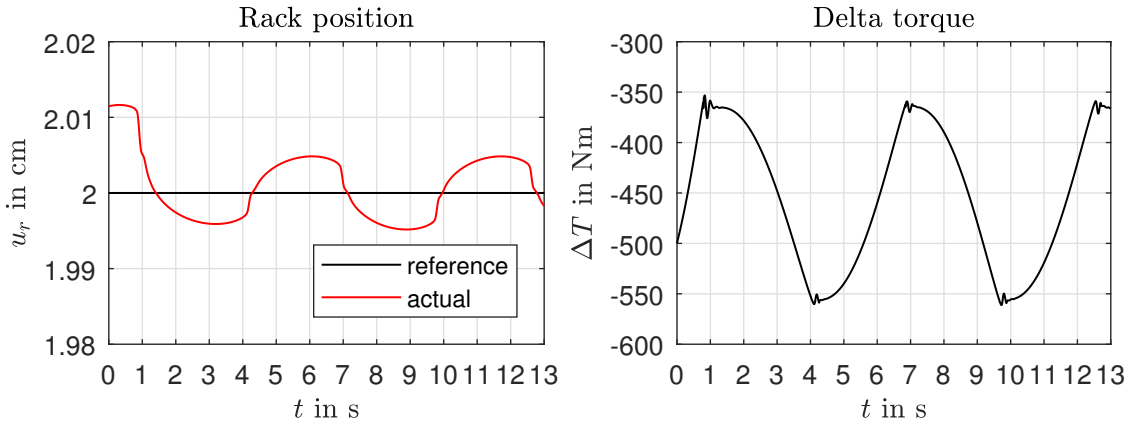

Figure 5.8: Simulated limit cycle during a steady state cornering situation using the cascaded controller. The increased aggressiveness compared to the state feedback controller minimized the time delays significantly, to the cost of occuring limit cycles in steady state situations. One can see in the torque plot that the controller is going up and down the static friction, because the control target slightly starts to oscillate around the reference.

The problem of limit cycles is that they can not be avoided, they can just be minimized in a way, they don't disturb the driver. Using linear controller theory, it will be always a compromise between the time delays and the impact of limit cycles in steady state situations.

5.2 Measurement Results

After parameterizing with the simulation model, the controllers were tested on the real demonstrator vehicle. It could be recognized that the found parameter sets in Section 5.1 were too aggressive for the real vehicle, which resulted in unstable behavior.

For the state feedback controller, the biggest problem was the resonance characteristic of the rack. This effect showed up much stronger than in the simulation. The only way to keep this problem under control was to lower the parameters of the controller, to the cost of a worse performance of the overall system. Table 5.3 shows the updated parameters for the state feedback controller.

Table 5.3: Updated parameters for the state feedback controller used for the experiments on the real car.

Param.	Value old	Value new	Description
k_c	$5 \cdot 10^5$	$1.3 \cdot 10^5$	Design parameter for the controller polynomial
k_o	$1 \cdot 10^5$	$3.1 \cdot 10^4$	Design parameter for the observer polynomial

Since the inner loop of the cascaded controller was tuned to compensate the rack resonance characteristic, the controller had no problems with it, even on the real vehicle. However, with the higher speed of the control system, another (unknown) resonance characteristic at 6.5 Hz occurred. The source for this additional resonance effect is not clearly determined yet, but it is assumed to come somewhere from the drive train. Nevertheless, also the parameters of the cascaded controller needed to be adjusted in order to provide a stable system. Table 5.4 shows the updated controller parameters.

Table 5.4: Updated parameters for the cascaded rack position controller used for the experiments on the real car. The controller gain of the inner loop controller had to be lowered by factor 10 in order to ensure stability of the controlled system. Also the damping coefficient was adjusted a little bit to increase the attenuation of the rack resonance effects.

Param.	Value old	Value new	Description
k_r	$-7.5 \cdot 10^4$	$-7.5 \cdot 10^3$	Gain of inner loop controller
z_r	2.069		Controller zero
p_r	46.41		Controller pole
d_r	30.81	25	Damping coefficient of complex pair of zeros
ω_r	20.394		Normalized frequency of complex pair of zeros
k_p	1		Gain of outer loop controller

5.2.1 Experiments

With these new sets of controller parameters for both the state feedback controller and cascaded controller, the same experiments as shown in Section 5.1 were done. Additionally the experiments were also done with the existing PID controller to provide a benchmark. In Figure 5.9 slalom maneuvers at $v \approx 25\,\mathrm{km/h}$ were done.

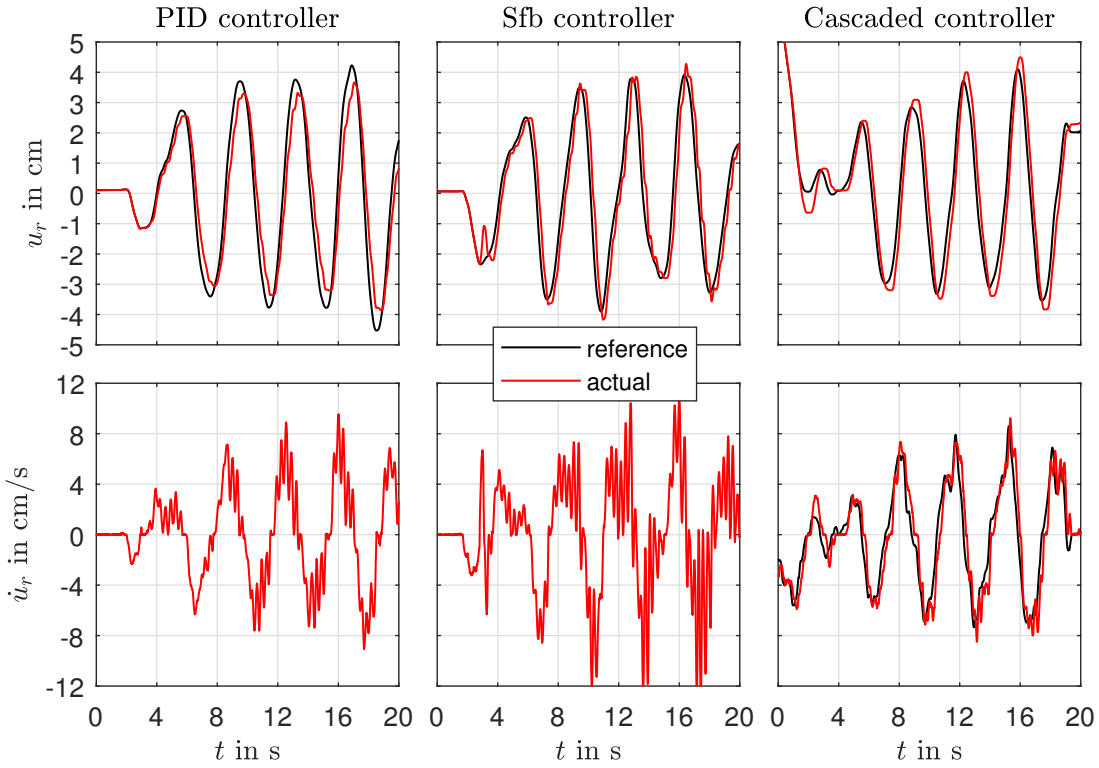

Figure 5.9: Slalom maneuvers at $v \approx 25\,\mathrm{km/h}$ using all 3 controllers. On the left plots, the results of the existent controller are shown to provide a benchmark.

Investigating the result from Figure 5.9, its clear that the PID controller is the slowest of all. It is not able to follow the reference well and also shows some resonance problems when looking to the plot of the rack velocity. The reference tracking gets better with the state feedback controller as it is more aggressive, but the higher controller gains amplify

also the resonance problems, which can be seen clearly. With the cascaded controller, the performance is a lot better. The oscillations of the rack velocity are well under control while providing the same or even a better reference tracking than the other controllers.

In the next experiment, step steer maneuvers were investigated. Figure 5.10 show step inputs at a vehicle speed of $v = 30\,\mathrm{km/h}$ for all 3 controllers.

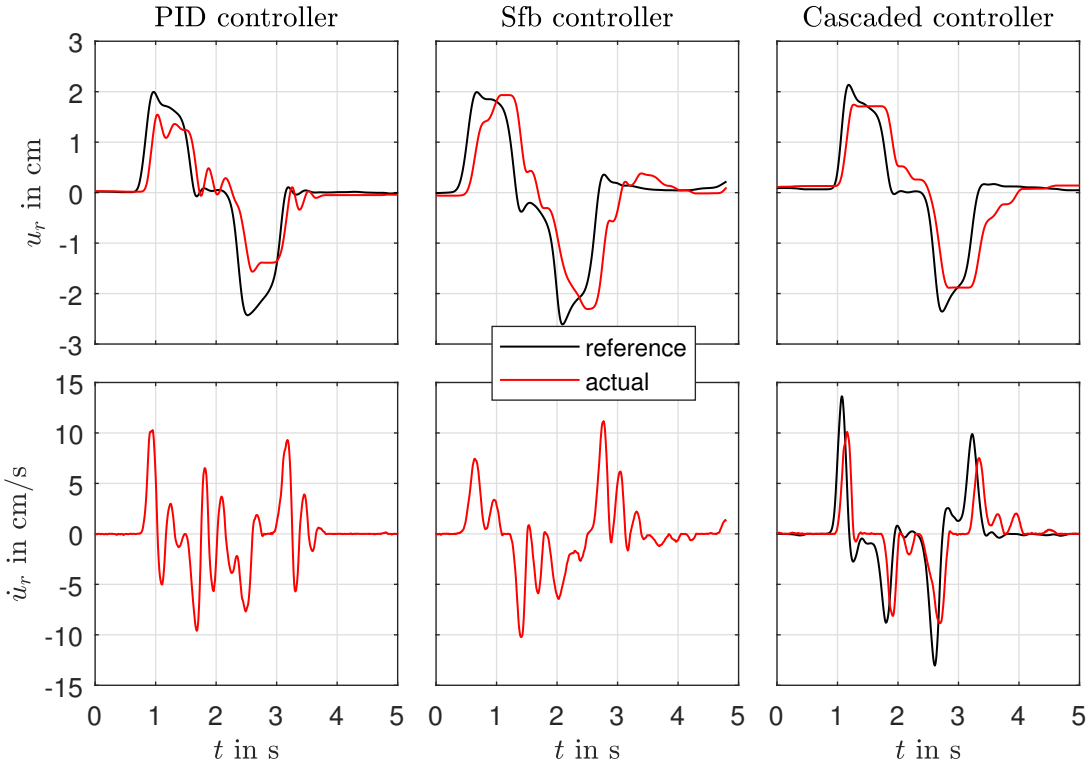

Figure 5.10: Step steer maneuvers at $v = 30\,\mathrm{km/h}$. One can see clearly that the response of the cascaded controller is significantly better than of the other controllers. Especially the PID controller start to oscillate a lot.

Same as for the slalom maneuver, the step maneuver shows the advantage of the cascaded controller that it is faster than the others and is able to keep the resonance effects of the rack under control. At this experiment, the oscillations with the PID controller were that high that it caused an uncomfortable feeling for the driver.

As a last experiment for comparing the three controllers, sweep maneuvers have been made (Figure 5.11). The idea behind this experiment was to stimulate the system at the resonance frequency of the rack in order to ensure the stability at this frequency. It can be seen that the system remained stable with all controllers. The cascaded controller is tuned to attenuate this resonance frequency, hence the performance at this frequency is better with the other controllers. But to keep in mind, such maneuvers will never happen in normal driving situations and were just made for a proof of stability.

It can be said that the cascaded rack position controller is clearly the best controller structure out of these three controllers and will be the reference for all further investigations.

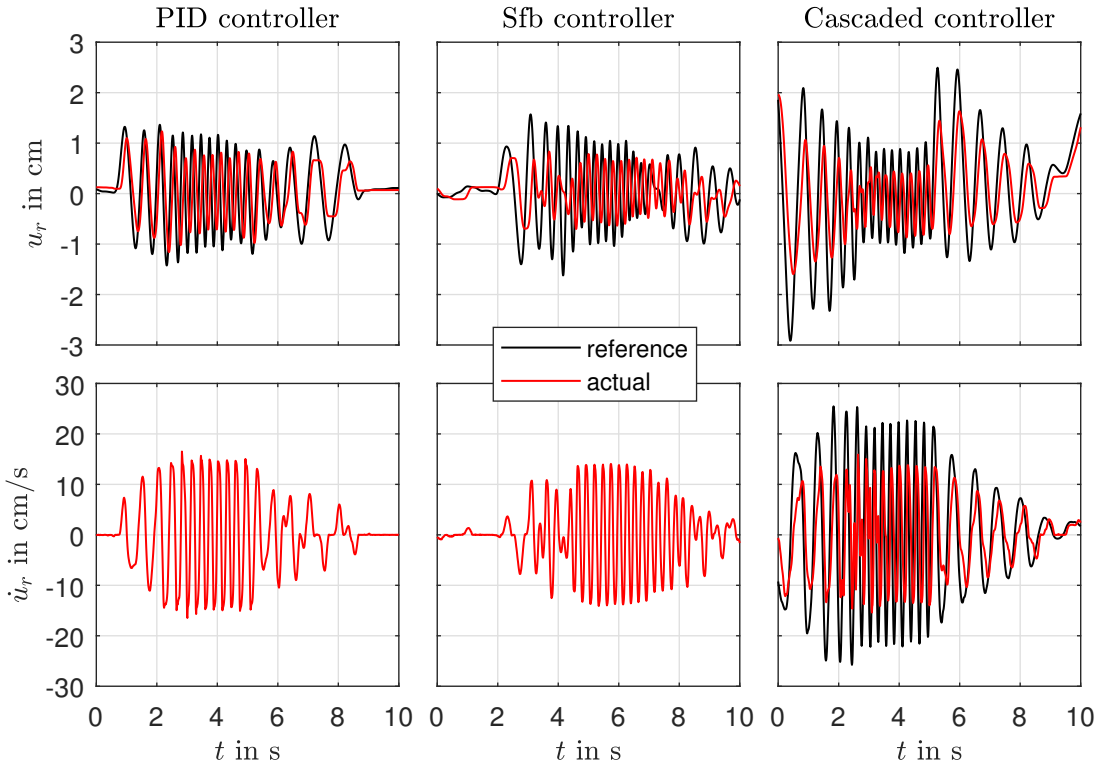

Figure 5.11: Sweep steer maneuvers at $v = 20\,\mathrm{km/h}$. It can be seen that all of the controllers ensured stability of the closed loop system at frequencies around the resonance of the rack.

5.2.2 Influence of the rack resonance

With the cascaded controller structure, the rack resonance is well under control. Nevertheless, this characteristic limits the performance of the overall system a lot, since controller outputs at this frequency need to be attenuated. There are several possibilities to improve the performance regarding this problem.

Two mechanical parameters mainly describe this resonance characteristic physically. The rack compensation mass m_r is one of them and is representing the value of the resonance frequency. With a lower mass (for example by decoupling the steering actuator of the SbW system when driving with SbTV), this resonance frequency would get higher. A higher resonance frequency would allow a more aggressive controller tuning, which would lead to a better performance.

The second mechanical parameter, that influences this behavior a lot, is the damping coefficient k_d of the rack. This damping effect is responsible for the attenuation of this resonance characteristic. With a higher damping, it would be possible to eliminate this problem completely. By installing a mechanical damper on the rack, it would also be very easy to implement this idea. But a big drawback of a higher damping is the energy consumption of the rack, which would significantly increase.

The third option is to increase the speed of the controller. If the closed loop system is significantly faster than the resonance frequency, it is also possible to improve the performance by controlling this resonance effect. This was also the idea behind the cascaded controller, as it was designed in the simulations. But on the real car, a different resonance

characteristic at higher frequencies occurred.

5.2.3 Influence of the additional resonance characteristic

The physical explanation of this resonance characteristic, which lies around $f = 6.5\,\mathrm{Hz}$ is not determined yet. But as the rack has its resonance around $f_\mathrm{r} = 3.2\,\mathrm{Hz}$ and the chassis around $f_\mathrm{c} = 1.2\,\mathrm{Hz}$, this resonance could come from the drive train. In the drive train there are a lot of mechanical components that have slackness, like the tripods from the half axle or the gears from the motor unit. Figure 5.12 shows the impact of this resonance making a step steer using the cascaded controller with a higher controller gain for the inner loop.

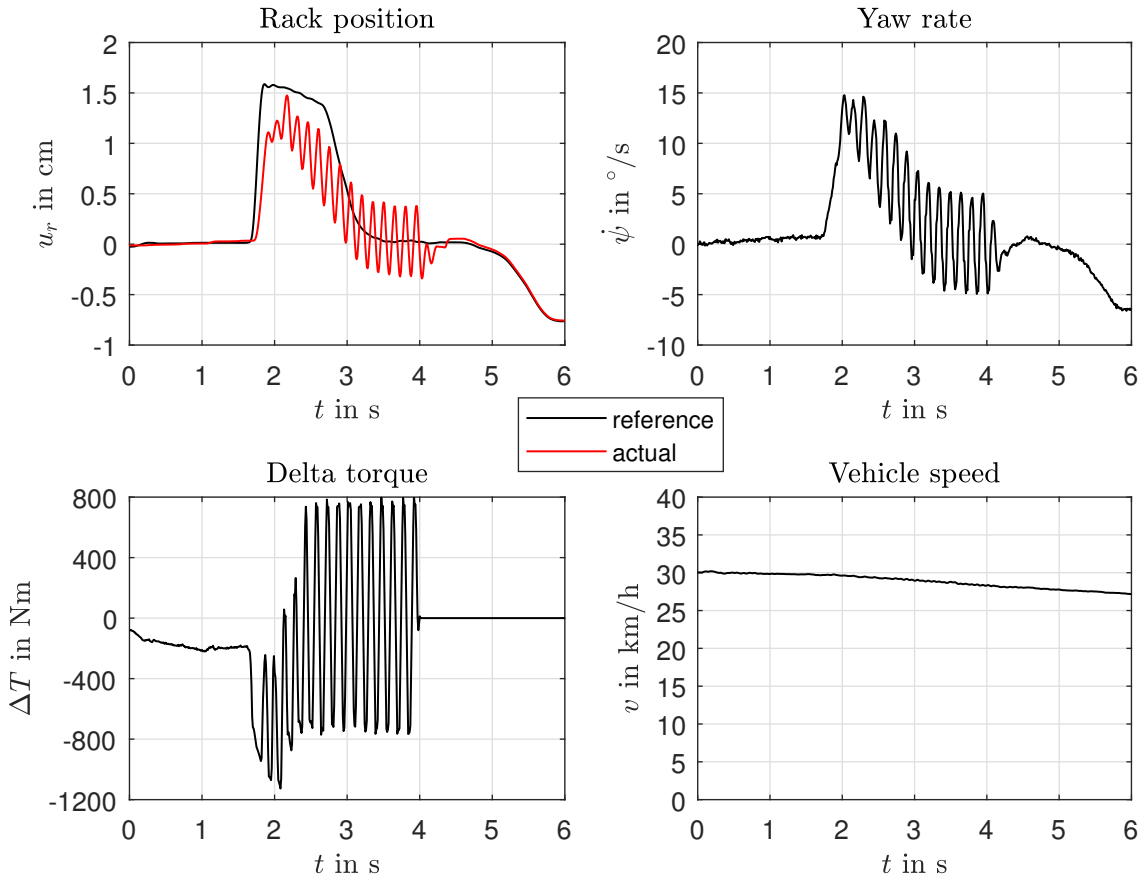

Figure 5.12: Step steer maneuver with the cascaded controller using a higher controller gain $k_\mathrm{r} = 2 \cdot 10^4$ for the inner loop. Immediately after the step steer input, the system starts to oscillate at around $f = 6.5\,\mathrm{Hz}$.

However, to further increase the performance of the inner controller, this oscillation has to be considered in the controller design. This consideration will be stated as an outlook of this thesis.

Therefore, the cascaded controller, as derived in Chapter 4 and tuned in Table 5.4 is the final controller used within this work.

5.3 Transition from SbW to SbTV

A very important requirement of SbTV is the applicability as a redundant steering system for a SbW vehicle. If the SbW system stops working, for whatever reason, SbTV must provide a safe possibility to steer the vehicle. For that purpose, the transition from SbW to SbTV has been investigated for various maneuvers, both in simulations and on the real car. The controller that was used for these investigations, was the cascaded controller.

5.3.1 Simulation Results

The experiment of choice for these investigations in simulations was the error case of SbW in a steady state cornering situation. Therefore, a rack position will be held constantly at a certain vehicle speed by the SbW model of the simulation. At a defined time, the SbW system will be switched off and at the same time, the SbTV controller will be switched on. Figure 5.13 shows this experiment for a vehicle speed of $v = 20\,\mathrm{km/h}$.

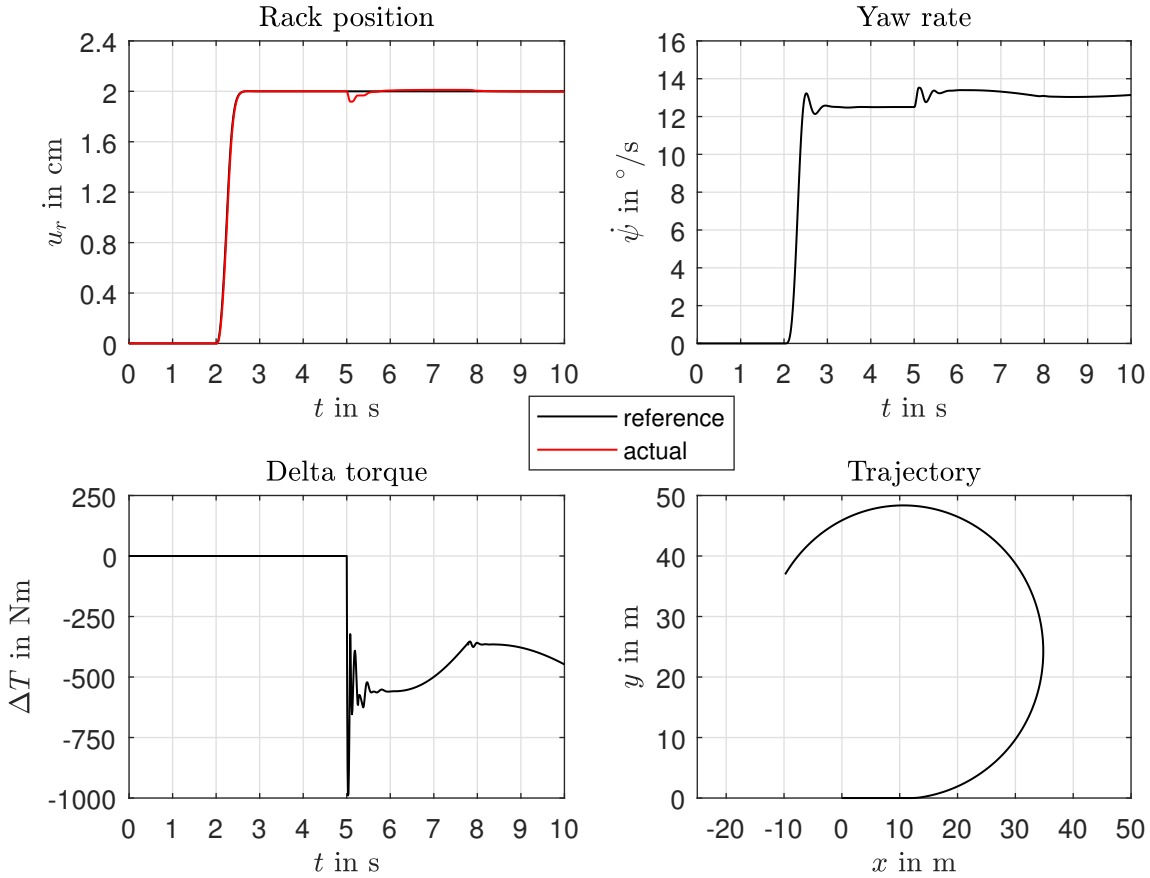

Figure 5.13: Transition of SbW to SbTV at time $t = 5\,\mathrm{s}$ with a vehicle speed of $v = 20\,\mathrm{km/h}$. The required torques to hold the desired rack position are generated very fast. The result is a transition that is hardly noticeable in terms of the rack position. Looking at the yaw rate, one can see that the yaw rate is higher as it is with SbW, whereas the rack positions are the same. This comes from the additional yaw torque, which is generated by SbTV.

This additional yaw torque points out a major drawback of controlling the steering rack position. With this additional amount of yaw rate, SbTV produces a different driving situation as SbW. This means, that the driver has to correct the steering wheel angle, if he wants to follow the same trajectory as with SbW. This effect increases with the speed,

as the rack positions get smaller with higher speeds but the additional torque remains the same. Figure 5.14 shows the same experiment as Figure 5.13 with a higher speed of $v = 42\,\mathrm{km/h}$.

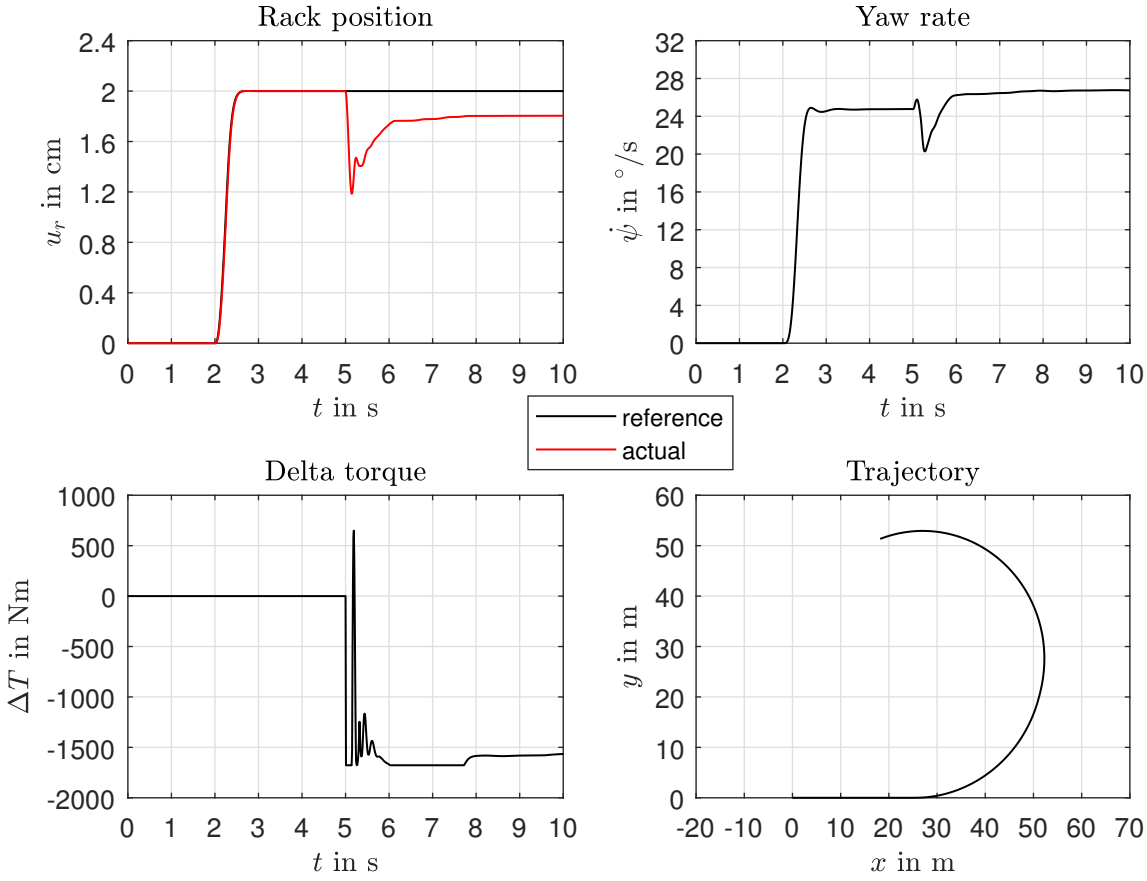

Figure 5.14: Transition of SbW to SbTV at time $t = 5\,\mathrm{s}$ with a vehicle speed of $v = 42\,\mathrm{km/h}$. In this case, the SbTV system is not able to hold the reference rack position of 2 cm, whereas the yaw rate is still higher than the one before the transition. This means that SbTV is still able to follow the trajectory in case of an error. Since the torques are saturated, the reaction of SbTV at the transition is slower than the one in Figure 5.13. This can be seen as a yaw rate drop for approximately 0.5 s.

Because of limitations regarding available driving torque or road traction, situations exist, where SbTV will not be able to follow the trajectory of the SbW system anymore. Then, SbTV has to provide the best possible solution to help the driver handling the situation. Figure 5.15 shows the same experiment as Figure 5.14 with a higher speed of $v = 55\,\mathrm{km/h}$.

It's clear that the reference generation for SbTV has to be different to the one of SbW, especially when it comes to the transition between these 2 systems. An easy solution to this problem would be to analyze the yaw rate for different vehicle speeds and rack positions for both the SbW and SbTV system. With lookup tables, the steering angle ratio of SbTV could be adjusted to allow the same steering behavior as with SbW. However, this strategy was not realized in this thesis and can be seen as an outlook.

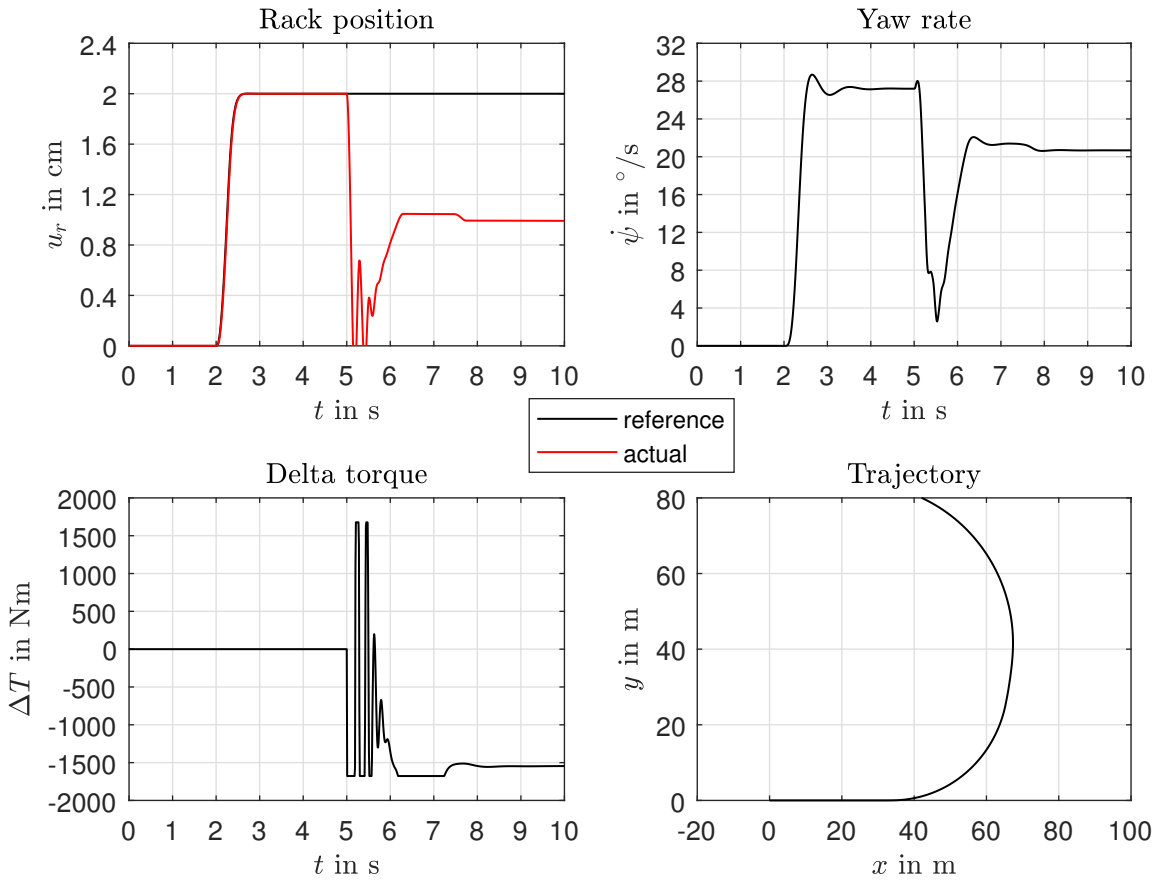

Figure 5.15: Transition of SbW to SbTV at time $t = 5\,\mathrm{s}$ with a vehicle speed of $v = 55\,\mathrm{km/h}$. After the transition, the SbTV system is only capable of holding the rack position at $u_\mathrm{r} = 1\,\mathrm{cm}$. In this situation, also the yaw rate after the transition will be lower than before, which means that the trajectory cannot be hold. This could lead to a dangerous situation for the driver. Furthermore, it takes nearly 1 s to build up the yaw rate, which can be seen in the trajectory plot, where the car goes almost straight in the transition.

5.3.2 Measurement Results

As the last part of this thesis, this transition from SbW to SbTV was also investigated on the demonstrator vehicle for two different maneuvers.

Figure 5.16 shows the error case at a slalom at a vehicle speed of $v \approx 25\,\mathrm{km/h}$. The transition happened around 7 s, which can be seen in the torque plot. The car was able to hold the rack position and enabled the driver to safely steer the car through the rest of the slalom.

In Figure 5.17 this problem was investigated in a steady state cornering situation at a higher speed of $v \approx 40\,\mathrm{km/h}$. One can see clearly that the yaw rate rises after the transition, even with a smaller rack position. As a consequence of this increased yaw rate, the driver had to correct the maneuver. But it has to be said that the driver was still able to steer the vehicle safely in this situation.

For all the experiments tried on the real car, SbTV always provided a safe backup solution of the SbW system.

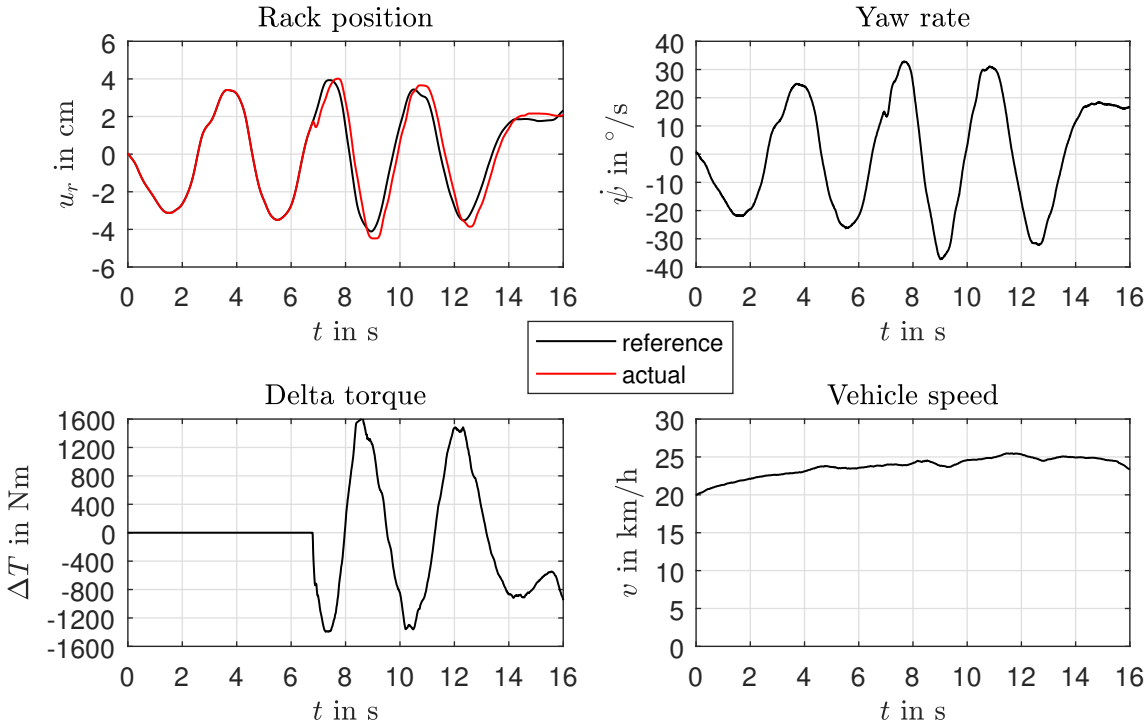

Figure 5.16: Transition of SbW to SbTV on the real car in a slalom maneuver. In this situation, the transition was easy to handle for the controller and the driver could finish the slalom safely.

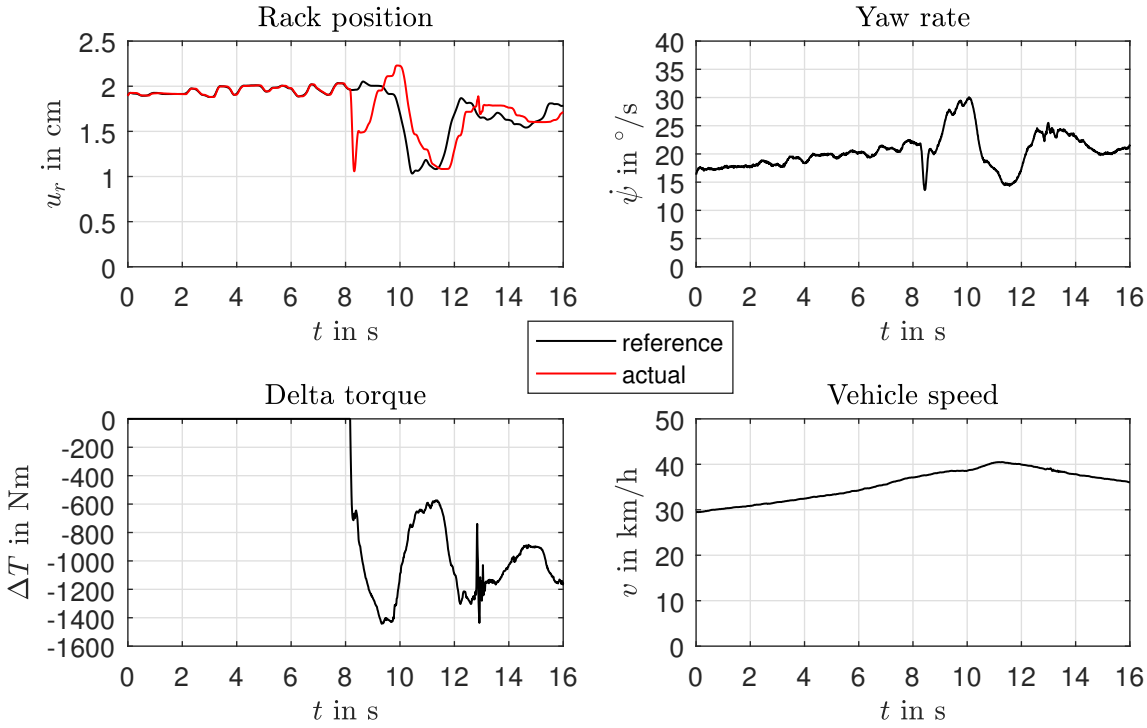

Figure 5.17: Transition of SbW to SbTV on the real car in a steady state cornering situation. One can see, that the driver had to correct the reference rack position to compensate the higher yaw rate of the SbTV system. The transition itself was stable and provided the driver the possibility to pursue the maneuver.

6 Outlook

SbTV is a promising technology that will definitely have it's place on the market when it comes to individually propelled electrical cars. But it has to be further developed first to exploit all the capabilities it can provide. Some possible topics, which could further increase the performance of SbTV, came out and can be seen as an outlook of this thesis:

Consideration of the additional resonance characteristic

The additional resonance characteristic around $f = 6.5\,\mathrm{Hz}$ needs to be understood more clearly where it comes from. Then, this resonance can be modeled both in the linear model and in the VTC simulation model as an extension to the existing parts. More on, this characteristic should also be considered in the controller design. One possible solution for the cascaded controller structure of the inner loop may be

$$R_1(s) = k_\mathrm{r} \frac{(s + z_\mathrm{r})\left(s^2 + d_{\mathrm{r}1}\, s + \omega_{\mathrm{r}1}^2\right)\left(s^2 + d_{\mathrm{r}2}\, s + \omega_{\mathrm{r}2}^2\right)}{s^2\,(s + p_{\mathrm{r}1})\,(s + p_{\mathrm{r}2})\,(s + p_{\mathrm{r}3})}, \tag{6.1}$$

where $\omega_{\mathrm{r}1}$ describes the rack resonance as before and $\omega_{\mathrm{r}2}$ describes the additional resonance characteristic with $d_{\mathrm{r}2}$ as the damping coefficient. The poles $p_{\mathrm{r}2}, p_{\mathrm{r}3}$ should be placed around this additional resonance frequency to allow the overall controller the same behavior as before.

With this consideration, it may be possible to further increase the performance of the inner loop controller a lot, which would increase the performance of the overall system.

Reference calculation for SbTV

Another important part would be the reference calculation based on the yaw rate to allow SbTV the same steering feel as SbW. There are two possible approaches:

- By analyzing the yaw rate of SbW and SbTV for different vehicle speeds and rack positions. Then, a recalculation of the reference target for SbTV based on lookup tables and the steering wheel angle would provide the car with the same steering feel as with SbW. The additional effort of making the experiments can be seen as a disadvantage of this method.
- A model based approach could calculate the yaw rate of the car in SbW mode based on the steering wheel angle and use this yaw rate to calculate an equivalent rack position for the SbTV system.

Especially when it comes to the transition between SbW and SbTV, this reference calculation becomes very important, otherwise the driver needs to correct the higher yaw rate to pursue the maneuver.

Yaw rate control for SbTV

When it comes to higher vehicle speeds, the rack positions in SbTV mode gets very small. At very high speeds, there could be the case, that the system may not be able to move the rack out of the origin because of the high rack friction. But with the yaw moment coming from the torque vectoring, there is still the possibility to steer the car, even without any rack movement. This means that at higher speeds the controller principles that

were derived in this thesis may not be promising anymore or even stop working. For this purpose, a control based on the yaw rate will be essential.

A control based on the yaw rate may also be necessary when it comes to automated or assisted driving, since trajectory planning is based on yaw rate. The state feedback controller can easily be switched to a yaw rate controller by changing the output matrix of the linear state space model to

$$\boldsymbol{c}^{\mathrm{T}} = \begin{bmatrix} 0 & 1 & 0 & 0 & 0 \end{bmatrix}. \tag{6.2}$$

The yaw rate control based on a cascaded controller structure could be realized by using a third loop around the rack position loop.

Advanced friction modelling with non-linear control

The only way to minimize the response time and phase delays of the system with linear theory is to increase the controller gain. But this will always be a drawback between stability of the closed loop system and influence of the friction. A better approach would be a proper modeling of the rack friction. A good foundation for this modeling is the thesis of Rohrmoser [16], who used a LuGre friction model for the SbW system. With this modeling approach, non-linear controller theory in the inner loop of the cascaded structure could be used to minimize the influence of the friction. Two methods are possible:

- The information of a friction observer could be used to compensate the non-linearities.
- A non-linear controller principle, which uses the information of the friction can be used. Sliding mode based strategies could be possible candidates for this kind of problem.

Changing the mechanical parameters of the rack

Since the resonance characteristic of the rack is mainly determined by the compensation mass m_{r} and the damping coefficient k_{d}, this characteristic could be also influenced by changing these parameters mechanically. On the one hand, a higher damping coefficient in form of a mechanical damper on the rack would minimize this resonance effect a lot to the costs of a higher energy consumption. On the other hand, by decoupling the steering actuator when using SbTV would decrease the compensation mass. As a direct consequence, this would increase the resonance frequency significantly. Then, the controller gains could be also higher, which would result in a better performance.

Modular Research Platform (MRP)

As explained in Chapter 1, the performance of SbTV is mainly determined by the suspension design of a car. The demonstrator vehicle that was used in this thesis has some disadvantages regarding the suspension, since very high torques are necessary for the use of SbTV. To experience more with the suspension design, TKP developed a further demonstrator vehicle, the modular research platform (MRP), Figure 6.1.

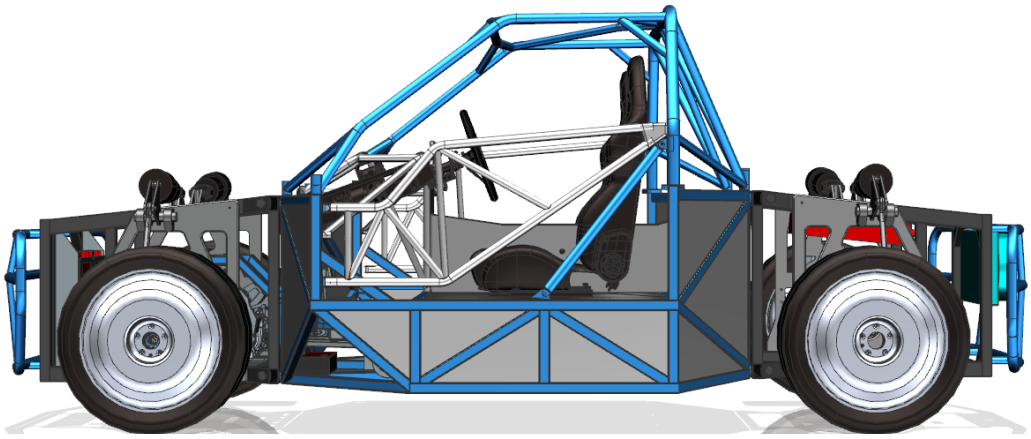

Figure 6.1: Modular Research Platform (MRP) [4]. Nearly all suspension parameters can be chosen individually by modular wheel carriers. Active suspensions, brake-by-wire and 3 electrical with a total power of 420 kW allow a lot of possibilities to investigate and develop various things in vehicle dynamics.

With this vehicle, the suspension can be adjusted to support SbTV in the best possible way. This means that the motors need less torques, which would be a huge advantage regarding bad road conditions (where traction could be a problem) and tire wear.

Besides the described topics, also the combination of SbTV and SbW could bring some advantages regarding safety, comfort, lateral driving performance and a lot more. There are still further topics that can be investigated and developed in the future.

7 Conclusion

The goal of this thesis was to develop model-based controller concepts for SbTV. In Chapter 1, the company TKP and it's newest field of research, Steer by Wire, was introduced. Then, the principle of Steer by Torque Vectoring and its desired application in the SbW system as a fallback solution was explained. More on, the motivation for the goal of this thesis was described. In Chapter 2, the demonstrator vehicle and the VTC simulation model [12] was explained. Furthermore, also the existing controller concept, which was seen as a benchmark for this thesis, was presented.

The first part in Chapter 3 covered the modeling part of this thesis. Since the simulation model described in [12] is too complex for the use in model based controller designs, a much simpler modeling approach in form of a basic two track model was derived. With a simple tire model, separated lateral dynamics, linearized slip quantities, a steady state load transfer model and a linear steering rack model, it was possible to derive a linear state space model of the car. This linear representation of the demonstrator vehicle was validated both with the VTC simulation model and measurement data and was then analyzed in frequency domain. By investigating the poles of the system, stability was ensured for all vehicle speeds. It resulted that the gain of the systems dropped strongly with increasing vehicle speeds, which means that controlling SbTV with the rack position works better for low vehicle speeds. Comparisons against the VTC simulation model and real measurement data showed that the result of the linear modeling represented the behavior of the car very well regarding resonance characteristics and dynamics.

In Chapter 4, the controller theory was discussed and derived. Instead of the yaw rate, it was decided to use the rack position as a control target. Better sensors for the rack position and a better applicability at low vehicle speeds confirmed this decision. With the linear state space model of Chapter 3, two different controller concepts were derived. First, a special structure of a state-feedback controller was chosen. This version supports integral action, which is needed to guarantee offset-free tracking of the reference (since the model didn't reproduce the real car's steady state behavior exactly). To avoid wind-up effects of the integrator, this state feedback controller also supports a anti windup strategy by feeding the saturated controller output back. A systematic design based on the algebraic controller synthesis [17] and the use of LQR tuning scheme provided an easy tuning procedure. A structure-variable extension based on Adamy [20] was added to provide a solution for different vehicle speeds. As the second controller concept, a cascaded structure had been chosen. The idea was to split up the control problem into a inner loop and a outer loop. The controller of the inner loop, with the rack velocity as it's control target, was enhanced by an anti windup strategy based on Hanus [22]. With a feed forward compensation of the rack velocity reference, the outer controller was designed as a P-controller. Both controller concepts were designed in continous time and were discretized afterwards for the use in the prototype hardware.

In Chapter 5, these controller concepts were validated and tested both in simulations with the VTC model and on the demonstrator vehicle. Because of the LQR tuning scheme, the state feedback controller could be tuned very fast. It was recognized that the controller had some problems regarding the rack resonance characteristic and tended to oscillate. In order to control this effect, the controller gains had to be lowered. This resulted in a slow response time and remarkable phase delays. The cascaded controller structure was tuned with the poles and zeros from the linear model. Therefore, it was possible to tune the controller to attenuate the rack resonance characteristic. Hence, this structure had no problems with oscillations and could be tuned much more aggressive than the state feedback controller. The quality of the closed loop system with the simulations resulted much better with the cascaded structure than with the state feedback controller. Investigations showed, that the rack friction is the main reason that causes phase delays and slow responses, since a certain force has to be generated first in order to allow any movement of the system. In steady state situations, it could be realized, that the rack friction also caused limit cycles, slight oscillations around the reference trajectory.

On the real car, the gain of the state feedback controller had to be lowered significantly, as the real car tended to be more unstable than the VTC simulation model. Especially the rack resonance characteristic showed up much more on the real car. Similar to the simulation results, the cascaded controller was able to deal with the rack resonance better than the state feedback controller, which resulted in a higher performance. With the higher controller gain of the cascaded controller, another (unmodeled) resonance characteristic at a frequency around $f \approx 6.5\,\mathrm{Hz}$ showed up. This additional effect could come from the drive train and tended the system to oscillate as well. To avoid these oscillations, also the gain of the cascaded controller had to be lowered.

With the cascaded controller, also the transition from SbW to SbTV was investigated. In simulations, the transition was performed during a steady state cornering situation for different vehicle speeds. Because of the additional yaw torque that is generated by SbTV, the yaw rate of SbTV is higher than the one from the SbW system (for the same rack position). This resulted in an unnatural steering feel. The reference generation for SbTV need to be based on the equivalent yaw rate, which is generated by SbW in order to produce the same steering feel as SbW. In the tests on the real car, the driver was always able to safley pursue the maneuvers when it came to the transition to SbTV. The investigations proved that SbTV is a possible canditate for the redundancy of a fail tolerant SbW system.

Finally, it can be said that the goals of this thesis were achieved. The linear model depicts a appropriate foundation for model based controller theory, even for more complex concepts than the ones introduced in this thesis. The state feedback approach provides a very easy-to-tune solution that results in a same, or even better performance than the existing PID controller concept. With the cascaded controller, the performance reaches a new level regarding response time, phase delay and steering feel. Furthermore, the influences of the rack friction and the rack resonance were investigated and provide an insight to the limitations of the system.

List of Symbols

Variables, parameters and constants

$\boldsymbol{a}$	vehicle acceleration vector at CoG
a_i	$i = 0 \dots n$, parameters of $\nu_\mathrm{u}(s)$
$\tilde{a}_i$	$i = 0 \dots n$, parameters of $\mu_\mathrm{u}(s)$
a_x	vehicle acceleration in x-direction at CoG
a_y	vehicle acceleration in y-direction at CoG
$\boldsymbol{A}$	dynamic matrix
A_f	frontal area of vehicle
A_{ij}	$i, j = 1 \dots 5$, parameters of dynamic matrix
$\boldsymbol{A}_\mathrm{r}$	dynamic matrix of controller in continuous time
$\boldsymbol{A}_\mathrm{rd}$	dynamic matrix of controller in discrete time
$\boldsymbol{A}_\mathrm{tf}$	dynamic matrix in controllability normal form
$\boldsymbol{b}$	input vector
$\hat{\boldsymbol{b}}$	gain vector of state observer
$\boldsymbol{b}_\mathrm{1r}$	reference input vector of controller in continuous time
$\boldsymbol{b}_\mathrm{2r}$	feedback input vector of controller in continuous time
b_f	track width of front axle
b_i	$i = 0 \dots n$, parameters of $\mu_\mathrm{y}(s)$
$\tilde{b}_i$	$i = 0 \dots n$, parameters of $\mu_\mathrm{y}(s)$ after partial fraction decomposition
b_r	track width of rear axle
$\boldsymbol{b}_\mathrm{tf}$	input vector in controllability normal form
B_5	parameter of input vector
$\boldsymbol{B}_\mathrm{rd}$	input matrix of controller in discrete time
$\boldsymbol{c}^\mathrm{T}$	output vector
c_a	cornering stiffness at nominal wheel load
c_d	drag resistance of air
c_i	$i = 0 \dots n$, parameters of $\Delta(s)$
c_p	gain of the transfer function $P_2(s)$
$\boldsymbol{c}_\mathrm{tf}^\mathrm{T}$	output vector in controllability normal form
$\boldsymbol{c}_\mathrm{r}^\mathrm{T}$	output vector of controller in continuous time
$\boldsymbol{c}_\mathrm{rd}^\mathrm{T}$	output vector of controller in discrete time
C	position of wheel center coordinate system

d_{1r}	direct reference feed trough of controller in continuous time
d_{2r}	direct output feed trough of controller in continuous time
d_i	$i = 0 \dots n$, parameters of $\hat{\Delta}(s)$
d_r	damping factor of inner loop controller $R_1(s)$
$\boldsymbol{d}_{rd}^T$	direct feed trough vector of controller in discrete time
d_{tf}	toe angle front
d_{tr}	toe angle rear
$\boldsymbol{e}$	estimation error of state observer
f	frequency quantity
$\boldsymbol{f}$	right hand side vector of the resultant equation
f_d	damping coefficient of the steering rack
f_r	static friction of the steering rack
f_{rw}	coefficient of roll friction
F_l	sum of forces on the steering rack coming from the tires
F_r	friction force of steering rack
F_R	steering rack force
F_x	sum of forces in x-direction at CoG
F_{xw}	$w = 1, 2, 3, 4$, longitudinal tire forces of the single wheels
F_{yw}	$w = 1, 2, 3, 4$, lateral tire forces of the single wheels
F_{zn}	nominal wheel load
F_{zw}	$w = 1, 2, 3, 4$, vertical tire forces of the single wheels
g	gravity constant
g_1	gain for upper state feedback controller
g_2	gain for lower state feedback controller
$G_u(s)$	observer transfer function 1
$\bar{G}_u(s)$	modified observer transfer function 1
$G_y(s)$	observer transfer function 2
h_{CoG}	height Center of Gravity
i_{belt}	transmission between steering actuator and BLD
i_{BLD}	transmission between BLD and steering rack
$\boldsymbol{I}$	identity matrix
$\boldsymbol{k}^T$	gain of state feedback controller
k_c	tuning parameter for the controller polynomial of the state feedback controller
k_d	steering transmission between rack position and steering angles
k_{fr}	slope of the friction describing function
k_o	tuning parameter for the observer polynomial of the state feedback controller

k_p	gain of P-controller
k_r	gain of inner loop controller $R_1(s)$
k_x	transmission of longitudinal tire force to rack force
k_y	transmission of lateral tire force to rack force
k_z	transmission of vertical tire force to rack force
$\boldsymbol{K}$	resultant
l_f	distance between front axle and CoG
l_r	distance between rear axle and CoG
l_sh	lever length for the steering arm
$L_1(s)$	open loop transfer function of the inner loop controller for stability analysis
m	overall vehicle mass
m_r	compensation mass of steering rack and actuator
m_z	mass of steering rack
M_sw	$w = 1, 2$, self aligning torques of front wheels
n	constant pneumatic trail of a tire
$N(s)$	approximate of the inverse of $P_2(s)$
N_ij	$i, j = 1 \dots 5$ parameters for non linearities in the derived model
$\boldsymbol{p}$	parameter vector for the unknown quantities of the state feedback controller
p_i	$i = 1, 2, 3, 4, 5$, poles of the transfer function $P_1(s)$
p_r	pole of inner loop controller $R_1(s)$
$\boldsymbol{P}$	solution of the algebraic ricatti equation
$P(s)$	transfer function of linear model with rack position as output
$P_1(s)$	transfer function of linear model with rack velocity as output
$P_2(s)$	transfer function between rack velocity and rack position
$P_c(s)$	compensatory open loop transfer function for the design of the outer loop controller $R_2(s)$
$\boldsymbol{Q}$	weighting matrix for LQR tuning method
Q_y	weighting factor for output weighting LQR
r	reference quantity for the controllers
$\tilde{r}$	conditioned reference quantity according to Hanus [22]
r_0	unloaded tire radius
r_s	static tire radius
r_D	dynamic tire radius
r_M	transmission of self aligning torques to rack force
$\boldsymbol{r}_\mathrm{vc1,v}$	distance from CoG to front left wheel center, depicted in the vehicle fixed coordinate system

R	weighting factor for LQR tuning method
$R(s)$	feed back transfer function of state feedback controller
$R_1(s)$	transfer function of inner loop controller of cascaded controller structure
$R_2(s)$	transfer function of outer loop controller of cascaded controller structure
R_B	roll balance of car
s_x	longitudinal slip of a not assigned wheel
$\boldsymbol{S}$	weighting matrix for LQR tuning method
$\boldsymbol{S}_\mathrm{u}$	controllability matrix of state space model
$\boldsymbol{t_1}$	bottom line of controllability matrix
t_s	sample time for discretized systems
$\boldsymbol{T}$	transformation matrix for controllability normal form
T	longitudinal torque
$T(s)$	closed loop transfer function
$T_1(s)$	closed loop transfer function of inner loop of cascaded controller
T_dw	$w = 1, 2$, drive torques of front wheels
$T_\mathrm{z,TV}$	yaw torque component from Torque Vectoring
ΔT	delta torque of front wheels
ΔT_req	requested delta torque
u	input quantity of state space realization
$u_\mathrm{min}, u_\mathrm{max}$	saturation limits of delta torque ΔT
u_r	position of the steering rack
$u_\mathrm{r,ref}$	reference position of the steering rack
$\dot{u}_\mathrm{r}$	velocity of the steering rack
$\dot{u}_\mathrm{r,ref}$	reference velocity of the steering rack
$\ddot{u}_\mathrm{r}$	acceleration of the steering rack
v	absolute vehicle velocity
$\boldsymbol{v}$	vehicle velocity vector at CoG
$\dot{\boldsymbol{v}}$	derivative of vehicle velocity vector at CoG
v_mod	modulus of absolute speed for discretization of vehicle velocity
v_space	discretization step of vehicle velocity
$\boldsymbol{v}_\mathrm{w}$	$w = 1, 2, 3, 4$, tire velocities of the single wheels
v_x	vehicle velocity in x-direction at CoG
$\dot{v}_\mathrm{x}$	derivative of vehicle velocity in x-direction at CoG
v_xw	$w = 1, 2, 3, 4$, tire velocities in x-direction of the single wheels
v_y	vehicle velocity in y-direction at CoG
$\dot{v}_\mathrm{y}$	derivative of vehicle velocity in y-direction at CoG
v_yw	$w = 1, 2, 3, 4$, tire velocities in x-direction of the single wheels
V	gain of state feedback controller
$V(s)$	feed forward transfer function of state feedback controller

w	controller output of state feedback controller
W	position of wheel contact patch coordinate system
W_B	weight balance of vehicle
$\boldsymbol{x}$	state vector of state space realization
$\hat{\boldsymbol{x}}$	state vector of observer
x_c	x axis of coordinate system at wheel center C
x_w	x axis of coordinate system at wheel contact patch W
y_c	y axis of coordinate system at wheel center C
y_w	y axis of coordinate system at wheel contact patch C
$\boldsymbol{z}$	state vector in controllability normal form, controller state vector
$\tilde{\boldsymbol{z}}$	state vector of conditioned controller according to Hanus [22]
z_c	z axis of coordinate system at wheel center C
z_i	$i = 1, 2$, zeros of transfer function $P_1(s)$
z_r	zero of inner loop controller $R_1(s)$
z_w	z axis of coordinate system at wheel contact patch C
α_w	$w = 1, 2, 3, 4$, slip angles of the single wheels
β	side slip angle of vehicle
$\dot{\beta}$	derivative of side slip angle
δ_w	$w = 1, 2$, steering wheel angles
θ_EM	Inertia of steering actuator
θ_BLD	Inertia of ball type linear drive
θ_wheel	Inertia of a single wheel
$\mu(s), \mu_\mathrm{i}$	$i = 0 \ldots 4$, nominator polynomial and its coefficients
$\mu_\mathrm{u}(s)$	nominator polynomial of $G_\mathrm{u}(s)$
$\mu_\mathrm{y}(s)$	nominator polynomial of $G_\mathrm{y}(s)$
$\nu(s), \nu_\mathrm{i}$	$i = 0 \ldots 4$, denominator polynomial and its coefficients
$\nu_\mathrm{u}(s)$	nominator polynomial of $\bar{G}_\mathrm{u}(s)$
τ	time constant of motor inverter model
ω_w	$w = 3, 4$, angular velocities of the single wheels
ω_r	resonance frequency of inner loop controller $R_1(s)$
$\boldsymbol{\omega}$	vehicle rotation vector at CoG
$\Delta(s)$	controller polynomial of state feedback controller
$\hat{\Delta}(s)$	observer polynomial of state observer
Θ	overall inertia of chassis around z-axis at CoG
$\dot{\psi}$	yaw rate of vehicle around center of gravity

Abbreviations

AFS	Active Front Steering
BLD	Ball type linear drive
CoG	Center of Gravity
DOF	Degrees of Freedom
PAS	Power Assisted Steering
SbTV	Steering by Torque Vectoring
SbW	Steer by Wire
TKP	ThyssenKrupp Presta AG
TV	Torque Vectoring
VTC	Name of simulation model from Georg Rill [10].

List of Figures

List of Tables

Bibliography

[1] "ThyssenKrupp Presta AG Homepage," http://www.thyssenkrupp-presta.com/de/index.php, accessed: 2017-09-23.

[2] P. Pfeffer and M. Harrer, *Steering Handbook*. Springer International, 2017.

[3] K. Polmans, "Modelling and Implementation of Steering System Feedback for Steer by Wire Systems," Master's thesis, Loughborough University, 2004.

[4] *Intern Documentation, Steer-by-Wire*, ThyssenKrupp Presta AG, 2016.

[5] M. Klein, A. Mihailescu, L. Hesse, and L. Eckstein, "Single Wheel Steering for the Research Vehicle Speed E," in *ATZ Worldwide*, October 2013, pp. 28–32.

[6] S. Stracke, "Torque Vectoring as Redundant Steering for Automated Driving or Steer-by-Wire," Master's thesis, RWTH Aachen, 2014.

[7] M. Zurbuchen, "Vehicle model and controller concept for steering using torque vectoring," Master's thesis, ETH Zrich, 2013.

[8] *SUNCAR Steer by Wire 2014/15 Endbericht Mechanik und Thermomanagement*, ETH Zurich, 2014/15.

[9] C. Pfister and J. Reis, "Entwicklung eines Regelalgorithmus zum Lenken eines Fahrzeugs mit Einzelradantrieb durch Torque-Vectoring," Master's thesis, NTB Buchs, 2016.

[10] G. Rill, *Road Vehicle Dynamics*. CRC Press, 2012.

[11] K. Esser, *Documentation IABG tyre measurement*, ThyssenKrupp Presta AG, 2016/17.

[12] G. Reiter, "Basic Investigations and Parameter Identification of a Steer-by-Wire Torque Vectoring Vehicle," Master's thesis, TU Graz, 2017.

[13] "dSpace Homepage," https://www.dspace.com/de/gmb/home.cfm, accessed: 2017-09-25.

[14] W. Hirschberg and H. Waser, *Fahrzeugdynamik Skript*, TU Graz, 2014.

[15] A. Mitterrutzner, "Development and Validation of a Vehicle Model for real time application on a Steer-by-Wire prototype," Master's thesis, TU Graz, 2015.

[16] M. Rohrmoser, "Rack Force Estimation for a Steer-by-Wire System," Master's thesis, Fachhochschule Vorarlberg, 2016.

[17] M. Horn and N. Dourdoumas, *Regelungstechnik*. Pearson Studium, 2004.

[18] P. Hippe and C. Wurmthaler, "Systematic closed-loop design in the presence of input saturations," in *Automatica Volume 35, Issue 4*, 1999, pp. 689–695.

[19] A. Cervin, *Multivariable Control, Lecture Notes*, LTH Lund, 2016.

[20] J. Adamy, *Nichtlineare Systeme und Regelungen*. Springer Professional, 2014.

[21] V. VanDoren, "Fundamentals of cascade control," http://www.controleng.com, visited in June 2017, Tech. Rep., 1999.

[22] R. Hanus, M. Kinnaert, and J. L. Henrotte, "Conditioning technique, a general anti-windup and bumpless transfer method," in *Automatica Volume 23, Issue 6*, 1987, pp. 729–739.

Appendix

Coefficients for the derived model

$$A_{11} = -\frac{g\,c_\mathrm{a}}{v\,F_\mathrm{zn}} \tag{8.1}$$

$$\begin{aligned} A_{12} = &-1 - \frac{g\,c_\mathrm{a}}{v^2\,F_\mathrm{zn}}\left(l_\mathrm{f}\,W_\mathrm{B} - l_\mathrm{r}\,(1-W_\mathrm{B})\right) \\ &+ 2\,\frac{h_\mathrm{CoG}\,d_\mathrm{tf}\,R_\mathrm{B}}{b_\mathrm{f}\,F_\mathrm{zn}}\left(c_\mathrm{a} - \frac{r_0}{r_\mathrm{s}} f_\mathrm{rw}\,F_\mathrm{zn}\right) \\ &+ 2\,\frac{h_\mathrm{Cog}\,d_\mathrm{tr}\,(1-R_\mathrm{B})\,c_\mathrm{a}}{b_\mathrm{r}\,F_\mathrm{zn}} \end{aligned} \tag{8.2}$$

$$A_{13} = \frac{g\,W_\mathrm{B}\,k_\mathrm{d}}{v\,F_\mathrm{zn}}\left(c_\mathrm{a} - \frac{r_0}{r_\mathrm{s}} f_\mathrm{rw}\,F_\mathrm{zn}\right) + \frac{2\,T\,k_\mathrm{d}}{v\,m\,r_\mathrm{s}} \tag{8.3}$$

$$A_{15} = -\frac{2\,d_\mathrm{tf}}{v\,m\,r_\mathrm{s}} \tag{8.4}$$

$$A_{21} = \frac{m\,g\,c_\mathrm{a}}{\Theta\,F_\mathrm{zn}}\left(l_\mathrm{f}\,W_\mathrm{B} + \frac{b_\mathrm{f}}{2}\,d_\mathrm{tf}\,W_\mathrm{B} + l_\mathrm{r}\,(1-W_\mathrm{B})\right) \tag{8.5}$$

$$\begin{aligned} A_{22} = &\frac{m\,g\,c_\mathrm{a}}{v\,\Theta\,F_\mathrm{zn}}\left(-l_\mathrm{f}^2\,W_\mathrm{B} + \frac{b_\mathrm{f}}{2}\,l_\mathrm{f}\,d_\mathrm{tf}\,W_\mathrm{B} - l_\mathrm{r}^2\,(1-W_\mathrm{B})\right) \\ &+ \frac{v\,m}{\Theta\,F_\mathrm{zn}} 2\,\frac{l_\mathrm{f}}{b_\mathrm{f}}\,h_\mathrm{CoG}\,d_\mathrm{tf}\,R_\mathrm{B}\left(c_\mathrm{a} - \frac{r_0}{r_\mathrm{s}}\,f_\mathrm{rw}\,F_\mathrm{zn}\right) \\ &+ \frac{v\,m}{\Theta\,F_\mathrm{zn}} h_\mathrm{CoG}\,R_\mathrm{B}\left(-c_\mathrm{a}\,d_\mathrm{tf}^2 - \frac{r_0}{r_\mathrm{s}}\,f_\mathrm{rw}\,F_\mathrm{zn}\right) \\ &- \frac{v\,m}{\Theta\,F_\mathrm{zn}}\left(2\,\frac{l_\mathrm{r}}{b_\mathrm{r}}\,h_\mathrm{Cog}\,d_\mathrm{tr}\;(1-R_\mathrm{B})\;c_\mathrm{a}\right) \end{aligned} \tag{8.6}$$

$$A_{23} = \frac{m\,g\,W_\mathrm{B}\,k_\mathrm{d}}{\Theta\,F_\mathrm{zn}}\left(l_\mathrm{f}\left(c_\mathrm{a} - \frac{r_0}{r_\mathrm{s}}\,f_\mathrm{rw}\,F_\mathrm{zn}\right) - b_\mathrm{f}\,d_\mathrm{tf}\,c_\mathrm{a}\right) + \frac{2\,T\,l_\mathrm{f}\,k_\mathrm{d}}{\Theta\,r_\mathrm{s}} \tag{8.7}$$

$$A_{25} = -\frac{2}{\Theta\,r_\mathrm{s}}\left(l_\mathrm{f}\,d_\mathrm{tf} + \frac{b_\mathrm{f}}{2}\right) \tag{8.8}$$

$$A_{41} = -\frac{m\,g\,W_\mathrm{B}\,c_\mathrm{a}\,(k_\mathrm{y} - r_\mathrm{M}\,n)}{m_\mathrm{r}\,F_\mathrm{zn}} \tag{8.9}$$

$$\begin{aligned} A_{42} = &-\frac{m\,g\,c_\mathrm{a}\,l_\mathrm{f}\,W_\mathrm{B}}{v\,m_\mathrm{r}\,F_\mathrm{zn}}\,(k_\mathrm{y} - r_\mathrm{M}\,n) \\ &+ \frac{v\,m\,2\,h_\mathrm{CoG}\,R_\mathrm{B}}{m_\mathrm{r}\,F_\mathrm{zn}\,b_\mathrm{f}}\left(\frac{r_0}{r_\mathrm{s}}\,f_\mathrm{rw}\,F_\mathrm{zn}\,k_\mathrm{x} + c_\mathrm{a}\,d_\mathrm{tf}\,(k_\mathrm{y} - r_\mathrm{M}\,n) - F_\mathrm{zn}\,k_\mathrm{z}\right) \end{aligned} \tag{8.10}$$

$$A_{43} = \frac{m\,g\,k_\mathrm{d}\,W_\mathrm{B}\,c_\mathrm{a}}{m_\mathrm{r}\,F_\mathrm{zn}}\,(k_\mathrm{y} - r_\mathrm{M}\,n) \tag{8.11}$$

$$A_{44} = -\frac{f_\mathrm{d}}{m_\mathrm{r}} \tag{8.12}$$

$$A_{45} = \frac{2\,k_\mathrm{x}}{m_\mathrm{r}\,r_\mathrm{s}} \tag{8.13}$$

$$A_{55} = -\frac{1}{\tau} \tag{8.14}$$

$$B_5 = \frac{1}{\tau} \tag{8.15}$$

$$N_{21} = -\frac{v\, m\, k_{\mathrm{d}}^2\, h_{\mathrm{CoG}}\, R_{\mathrm{B}}\, c_{\mathrm{a}}}{\Theta\, F_{\mathrm{zn}}} \tag{8.16}$$

$$N_{22} = \frac{m\, k_{\mathrm{d}}\, l_{\mathrm{f}}\, h_{\mathrm{CoG}}\, R_{\mathrm{B}}\, c_{\mathrm{a}}}{\Theta\, F_{\mathrm{zn}}} \tag{8.17}$$

$$N_{23} = \frac{v\, m\, k_{\mathrm{d}}\, h_{\mathrm{Cog}}\, R_{\mathrm{B}}\, c_{\mathrm{a}}}{\Theta\, F_{\mathrm{zn}}} \tag{8.18}$$

$$N_{41} = -\frac{f_{\mathrm{r}}}{m_{\mathrm{r}}} \tag{8.19}$$

$$N_{42} = \frac{1}{k_{\mathrm{fr}}} \tag{8.20}$$